

DETECTION OF CITRUS CANKER USING HYPERSPECTRAL IMAGING
TECHNIQUE

By

NIKHIL PRAMOD NIPHADKAR

A THESIS PRESENTED TO THE GRADUATE SCHOOL
OF THE UNIVERSITY OF FLORIDA IN PARTIAL FULFILLMENT
OF THE REQUIREMENTS FOR THE DEGREE OF
MASTER OF SCIENCE

UNIVERSITY OF FLORIDA

2010

© 2010 Nikhil Pramod Niphadkar

To my Aai and Baba

And

To all my Gurus

// Gururbramha gururvishnu gururdevo maheshwara //

// Guru sakshyat parabramha tasmaishri guruve namaha //

ACKNOWLEDGMENTS

I would like to thank my advisor Dr. Thomas F. Burks for providing me a priceless guidance and encouragement during the course of this research. I am also grateful to Dr. Wonsuk Lee and Dr. Clint Slatton for the invaluable technical assistance they provided by being on my thesis committee. I would also like to thank Dr. Warren Dixon for being my advisor in Mechanical and Aerospace Engineering department.

In addition, I would like to appreciate the valued support provided by my colleagues Dr. Jianwei Qin and Dr. Duke Bulanon, without whose help this research could not have completed. Also, I would like to express my gratitude to Mr. Mike Zingaro and Mr. Greg Pugh for their precious help in building the hyperspectral imaging system and all the technical aid they provided. At last but not the least, I would like to thank all my friends for being there during the hard times and encouraging me to keep going.

TABLE OF CONTENTS

	<u>Page</u>
ACKNOWLEDGMENTS.....	4
LIST OF TABLES.....	9
LIST OF FIGURES.....	10
ABSTRACT	12
1 INTRODUCTION	15
Overview of United States Citrus Industry	15
Necessity of the Automated Detection System	16
2 OBJECTIVES OF RESEARCH.....	19
Estimation of Detection Limit for Size of Citrus Canker Lesions Based on Hyperspectral Imaging.....	19
Detection of Citrus Canker Using RGB Color Image Along with Near Infrared (NIR) Monochrome Images	19
Compensation of Edge Effect on Spherical Objects due to Light Source – Hyperspectral Imaging Application	20
3 LITERATURE REVIEW	21
Citrus Canker.....	22
Image Processing Techniques Used in Agriculture	23
Hyperspectral and Multispectral Imaging Based Approaches Used in Agriculture..	29
Hyperspectral and Multispectral Imaging Coupled with Computer Vision and Pattern Classification Approaches.....	32
4 OVERVIEW OF MATERIALS AND METHODS.....	35
Citrus Samples	35
Hyperspectral Imaging System	37
Image Pre-Processing	38
Flat field correction	39
Image Masking and Binning.....	41
Hyperspectral Band Selection Using Correlation Analysis (CA)	41
Image Classification.....	43
Principle Component Analysis (PCA)	44
Estimation of Detection Limit for Size of Citrus Canker Lesions Based on Hyperspectral Imaging.....	45

	Detection of Citrus Canker Using RGB Color Image Along with NIR Monochrome Images	46
	Compensation of Edge Effect on Spherical Objects due to Light Source – Hyperspectral Imaging Application	47
5	ESTIMATION OF DETECTION LIMIT FOR SIZE OF CITRUS CANKER LESIONS BASED ON HYPERSPECTRAL REFLECTANCE IMAGING	51
	Introduction	51
	Materials and Methods.....	54
	Citrus Samples	54
	Hyperspectral Imaging System.....	55
	Image Pre-Processing.....	57
	Hyperspectral Band Selection	58
	Image Classification	59
	Binary Lesion Size Detection Algorithm	60
	Mapping Binary Lesion Size to Original Hyperspectral Image	61
	Results, Observations and Discussion.....	62
	Image Classification Results	62
	Binary Lesion Size Estimation Results	63
	Results of Mapping Binary Lesion Size to Original Hyperspectral Image	64
	Summary and Conclusion.....	66
6	DETECTION OF CITRUS CANKER USING RGB COLOR IMAGE ALONG WITH NEAR-INFRARED MONOCHROME IMAGES	76
	Introduction	76
	Materials and Methods.....	79
	Citrus Samples	79
	Hyperspectral Imaging System.....	80
	Image Pre-Processing.....	82
	Simulation of RGB Color Image	82
	Combining RGB Color Image and Remaining Monochrome Images	83
	Hyperspectral Band Selection	84
	Image Classification	86
	Results, Observations and Discussion.....	87
	Key Wavelengths for Canker Detection.....	87
	Ratio Images	89
	Image Classification Results	89
	Why RGB Image Can't Be Used for Canker Identification?.....	92
	Summary and Conclusion.....	97

7	COMPENSATION OF EDGE EFFECT ON IMAGES OF SPHERICAL OBJECTS DUE TO LIGHT SOURCE – HYPERSPECTRAL IMAGING APPLICATION	107
	Introduction	107
	Materials and Methods.....	110
	Hyperspectral Imaging System.....	110
	Flat Field Correction	112
	Image Masking and Binning	114
	Derivation of Geometric Correction Factor	114
	Generating the Digital Elevation Model	118
	Estimation of Geometric Correction Factors.....	122
	Algorithm Validation Tests.....	123
	Results, Observations and Discussion.....	125
	Digital Elevation Model Observations.....	125
	Geometric Correction Factor Observations and Results	126
	Validation Test Results.....	127
	Summary and Conclusion.....	130
8	OVERALL SUMMARY, CONCLUSIONS AND FUTURE SCOPE	141
	Summary and Conclusions	141
	Future Scope	143
 APPENDIX		
A	MATLAB CODE FILES - ESTIMATION OF DETECTION LIMIT FOR SIZE OF CITRUS CANKER LESIONS BASED ON HYPERSPECTRAL REFLECTANCE IMAGING	145
B	MATLAB CODE FILES - DETECTION OF CITRUS CANKER USING RGB COLOR IMAGE ALONG WITH NIR MONOCHROME IMAGES.....	147
	Main Program File	147
	Simulation of the RGB + NIR images	147
	Generation of Spectra of Different Disease Conditions	149
	Function Files	150
	Function to Perform the Correlation Analysis on the Image Data.....	150
	Function to Read the Image File in ENVI Format in MATLAB	152
	Function to Write the MATLAB Array into an Image File in ENVI Format.....	154
C	MATLAB CODE FILES - COMPENSATION OF EDGE EFFECT ON IMAGES OF SPHERICAL OBJECTS DUE TO LIGHT SOURCE.....	156
	Main Program File	156
	Function Files	160

LIST OF REFERENCES 162
BIOGRAPHICAL SKETCH..... 166

LIST OF TABLES

<u>Table</u>		<u>Page</u>
4-1	Numbers of fruit samples for each peel condition.....	50
5-1	Numbers of fruit samples for each peel condition.....	74
5-2	Summary of classification results	74
5-3	Effect of number of erosion cycles on canker lesion size estimation	75
6-1	Summary of classification results	106

LIST OF FIGURES

<u>Figure</u>	<u>Page</u>
4-1 Representative normal and diseased peel conditions of grapefruit samples	48
4-2 Hyperspectral imaging system for reflectance image acquisition from grapefruits.....	49
4-3 Image classification procedure	50
5-1 Representative normal and diseased peel conditions of grapefruit samples	68
5-2 Hyperspectral imaging system for reflectance image acquisition from grapefruits.....	69
5-3 Image Classification Procedure	70
5-4 Classification Method-Discrimination of canker from other peel conditions	71
5-5 Effect of variation of threshold values on classification accuracies.....	72
5-6 Final Binary Image of a sample before and after applying the 'bwareaopen' function.....	72
5-7 Mapping binary lesion size to original hyperspectral image.....	73
5-8 Probability distribution of lesion size of all samples	73
5-9 Probability distribution of lesion size of subset of all samples	74
6-1 Representative normal and diseased peel conditions of grapefruit samples	99
6-2 Hyperspectral imaging system for reflectance image acquisition from grapefruits.....	100
6-3 Red, Green and Blue filter transmittance characteristics.....	101
6-4 Contour of correlation coefficients between two band ratios and fruit peel conditions	102
6-5 Mean reflectance spectra of grapefruits with different peel conditions	103
6-6 Two band Ratio images for different disease conditions. (From L to R Canker, Greasy Spot, Insect Damage, Normal, Melanose, Scab, Wind Scar) .	103
6-7 Image classification procedure	104

6-8	Values of two band ratio between 771 and 739 nm (R_{771}/R_{739}) for different peel conditions.....	105
6-9	Effect of variation of threshold values on classification accuracies.....	105
7-1	Hyperspectral imaging system for reflectance image acquisition from grapefruits.....	132
7-2	Pilot points and center of mass.....	133
7-3	Pilot points (red in color) and nodes of interpolation (green in color) of one of the meridians	133
7-4	Transversal plane formed by maximum fruit height (h_c) and center of mass of the fruit (C_g). The computed elevations of the interpolation nodes is also shown by 'center line'	134
7-5	Side view of the modeled ellipse and the elevations of interpolation nodes	135
7-6	3-D view of the modeled ellipse and the elevations of interpolation nodes.....	135
7-7	Digital elevation model	136
7-8	Contour of geometric correction factor (ϵ_g)	137
7-9	Effect of application of geometric correction – Single band image at 724 nm ..	137
7-10	Citrus sample marked with the angular graduations and the regions of interest.....	138
7-11	Reflectance spectra of ROI 3.....	139
7-12	Reflectance spectra of all three ROIs at the rotation of 40 degrees	140

Abstract of Thesis Presented to the Graduate School
of the University of Florida in Partial Fulfillment of the
Requirements for the Degree of Master of Science

DETECTION OF CITRUS CANKER USING HYPERSPECTRAL IMAGING
TECHNIQUE

By

Nikhil Pramod Niphadkar

May 2010

Chair: Thomas F Burks

Major: Agricultural and Biological Engineering

The citrus industry of Florida has led the economy of the State of Florida to prosperity. The statistics shows that Florida produces maximum citrus supply throughout United States. However, one of the biggest challenges the industry has been facing for quite a while is citrus canker. The reason citrus canker being such an important issue is its fast spread and very high damage potential which is affecting the export of citrus fruits to several international markets including European countries. Presently the stress is on preventing the cankerous citrus fruits from entering the unaffected regions. The studies have proven that the automated detection systems can help in prevention of citrus canker and thus reduce the serious loss Florida citrus industry has been facing. The basic underlying objective of this thesis was to develop an approach for canker detection for a real time application on a packaging line using hyperspectral imaging. The thesis consisted of three different studies, the outcomes of which are abstracted here.

The first study was aimed at estimating the capability of the previously developed multispectral algorithm using correlation analysis to detect smallest possible canker lesion on the citrus fruit. More specifically the goal of this work was to determine the

size of the smallest canker lesion that can be detected. The optimal wavelengths selected using correlation analysis were 834 nm and 729 nm. The best overall classification accuracy achieved was 95.7% when the binary threshold value of 1.275 was used. This threshold value was found to give best tradeoff between canker classification and overall classification. The smallest lesion detected by the lesion size estimation algorithm had the surface area of 2.16 sq. mm. and equivalent diameter was 1.66 mm.

The second part of the thesis consisted of an attempt to develop a novel approach to discriminate citrus canker from other surface conditions. The idea was to explore if a two camera system with one CCD color camera (to capture RGB color image) and one monochrome camera (to capture NIR single band image) could be built for canker detection in online real time packaging application. As this was an experimental study, the hybrid hyperspectral image including RGB color image and NIR single band images was simulated using previously captured hyperspectral image data (450 - 930 nm). This image was then subjected to the correlation analysis (CA) to identify the key channels. The CA did not select any of the red, green or blue channels as significant channels for canker identification. The reason being higher bandwidths of the R, G and B channels which not only might have included the information to detect canker but also other peel conditions. It was concluded that RGB color image (along with some single band monochrome image) cannot be utilized to discriminate canker from other peel conditions based on simple thresholding technique.

The third and final piece of the thesis was to re-implement the compensation algorithm to eliminate the adverse effects of light source while capturing the image of

spherical objects like citrus fruits. The motivation behind this study was to reduce the misclassification of citrus fruits due to the edge blackening effect which our research team had been facing. The algorithm was developed by Gomez et al. 2007. The image was corrected for the spatial variations (flat field correction) caused by intensity of light source as well as geometrical variation caused by the spherical geometry of the citrus fruit. The geometric correction was accomplished by constructing a 3-D digital elevation model (DEM) of the fruit from its 2-D image. This DEM provided us with the geometric properties of the fruit like X, Y, and Z coordinates which were exploited in the course of estimating the geometric correction factor for each pixel. The corrected image portrayed improved and uniform brightness of the citrus fruit surface throughout. Few tests were also conducted to validate the results of the algorithm which essentially proved that the geometric correction results in uniform intensity of radiation throughout the fruit surface.

CHAPTER 1 INTRODUCTION

Citrus production is the second largest industry in the State of Florida. More than 70% of the citrus supply of United States is produced in Florida. Citrus industry has proved to be an important source of employment to many. The agricultural economy and the economy in general of the State of Florida is influenced significantly by the citrus industry. And hence one can safely say that to improve the economy of the state we should target the citrus and various related industries.

However, the Florida citrus industry has been facing a serious challenge of disease control. Among different diseases, citrus canker has proven to be one of the most devastating diseases that endanger the marketability of the citrus crops. Citrus canker can infect most commercial citrus varieties. Caused by bacterial pathogen *Xanthomonas axonopodis*, the disease is characterized by conspicuous, erumpent lesions on leaves, stems, and fruit. Citrus canker could cause defoliation, blemished fruit, premature fruit drop, twig dieback, and tree decline. Due to its fast spread, high damage potential, and massive impact on export and domestic trade, canker is considered as one of the most disturbing diseases that threaten all citrus-growing areas. The emphasis of this particular exploration is on developing the measures that could differentiate between diseased and marketable citrus fruits, preventing them from entering the canker free areas and thereby restricting the further spread of the disease.

Overview of United States Citrus Industry

Florida leads U.S. citrus production and accounts for a major part of the U.S. citrus industry. According to the citrus production report (USDA, 2005-06), Florida accounts for more than 70% of U.S. citrus production. Florida produces a number of different

citrus products. Orange, grapefruit, and lemons are major citrus crops, with lesser production in tangerines, limes, and an increasing variety of specialties. Oranges account for more than 80 percent (Hodge et al., 2001). Orange and grapefruit account for about 90 percent of U.S. production (Jacobs et al., 1994). Florida, California/Arizona, and Texas are the major states for U.S. citrus productions. Florida accounted for more than three quarters of all U.S. citrus, while California/Arizona and Texas had the remainder. Citrus is consumed not only as fresh fruit but also in products that use citrus fruits. Florida has 52 citrus processing plants (Hodges et al., 2001). They produce various orange juice items such as chilled, canned juice, and concentrated juice. These plants also produce many byproducts like citrus pulp, molasses, and the essential oil-limonene (Hodges et al., 2001) along with a number of byproducts like food additives, cattle feed, and cosmetics.

Necessity of the Automated Detection System

Twenty first century is characterized by technological advances. Automated systems are used everywhere. Various scientists, organizations etc. have been working hard to bring automation into the agricultural industry. Since the citrus production volume in Florida is very large, it is really difficult to inspect all the fruits using human inspectors. Also, after a while, human inspectors are prone to make mistakes because of the fatigue caused by repetition. Moreover in the packaging industries, the conveyors are designed to carry the fruits at considerably high speeds (say 5 to 10 fruits per second). At such high speeds, it becomes almost impossible for the human inspectors to catch the diseased fruits. In such cases, automated disease detection systems prove to be the ultimate solution, the performance of which does not get affected by long working hours. The automated systems hence not only improve the performance of the

detection but they also reduce the labor expenses needed otherwise. The hyperspectral imaging has provided a new facet to the automated disease detection systems. This particular thesis consists of three basic components:

1. Estimation of detection limit for size of citrus canker lesions based on hyperspectral imaging
2. Detection of citrus canker using RGB color image along with NIR monochrome images
3. Compensation of edge effect on spherical objects due to light source – Hyperspectral imaging application

The first part aims at estimating smallest possible canker lesion that can be detected using the hyperspectral imaging technique. The misclassification of cankerous citrus fruits with very small canker lesions was the motivating factor behind this exploration. The previously developed multispectral algorithm using hyperspectral wavelengths by our research group was used for segregation of cankerous citrus fruits from fruits with other peel conditions (normal, greasy spot, insect damage, melanose, scab and wind scar). We then used the image processing techniques such as morphological opening to estimate the size of smallest lesion detected.

The second part of this thesis is dedicated to development of an innovative algorithm for classification of citrus fruits into diseased and marketable class. There are totally seven classes, six diseases (canker, greasy spot, insect damage, melanose, scab, windscar) and a marketable class. The algorithm makes use of visible and Near Infrared (NIR) wavelengths of hyperspectral image as separate channels lumped together to create a single image. The resulting image is then processed further using some multivariate statistical algorithms like principle component analysis (PCA) or correlation analysis (CA) to identify the key wavelengths in the NIR region which will

help separate the cankerous citrus fruit from fruits of other peel conditions. The basic objective behind this was to simulate the output of the two camera system installed on the packaging line, including one CCD camera (outputting the RGB image) and one monochrome camera (outputting the single NIR wavelength image) to provide four channels of red, green, blue and NIR wavelength which in turn would be used to detect canker. The motivation behind this research was, RGB images have proven to be a good source to detect the physical defects like bruises on biological products while NIR wavelengths have shown a good potential to detect canker on citrus fruits (Qin et al., 2008 and 2009). In addition sooty mold which typically gets confused with other disease symptom can be detected at 510 nm which is already covered in the RGB region. So combining these two regions (RGB and NIR) can provide a means to identify all types of defects that can be found on citrus fruits in a very cost effective manner.

When a computer vision system is used to capture the image of a spherical object, the curvature of the object results in some adverse effects like darkening of the edges. This darkening of edges may misguide the algorithm to detect a normal peel as damaged or diseased. This was the underlying inspiration for re-implementing the edge effect compensation algorithm developed by Gomez-Sanchis et al., (2007) which constitutes the third and final part of the thesis. A correction factor was calculated for every fruit pixel by generating the 3-D model of the fruit called digital elevation model (DEM) and obtaining geometric properties like Cartesian coordinates for each pixel. Application of this correction to the fruit image resulted in uniform intensity over the fruit surface reducing the edge darkening.

CHAPTER 2 OBJECTIVES OF RESEARCH

This thesis constitutes of three major components. The objectives of each of them are mentioned below:

Estimation of Detection Limit for Size of Citrus Canker Lesions Based on Hyperspectral Imaging

The main objective of this exploration was to estimate the detection limit for the size of citrus canker lesions. Following were the sub-objectives to achieve the final goal:

- To use the previously developed multispectral algorithm for detecting the smallest possible cankerous lesion on the citrus fruit.
- To determine the controlling factors and their optimal values in canker lesion size estimation.

Detection of Citrus Canker Using RGB Color Image Along with Near Infrared (NIR) Monochrome Images

The main aim was to develop an algorithm to classify citrus fruits in diseased and marketable classes. The intermediary objectives were:

- To simulate the grayscale images of “Red”, “Green” and “Blue” channels of the citrus fruit from the already available 3-D hyperspectral image dataset.
- To combine the “Red”, “Green” and “Blue” channels along with the rest of monochrome images (wavelengths not considered in creating the RGB image i.e., 700 to 930 nm) from the hyperspectral data.
- Select the appropriate channels/wavelengths using PCA or CA for canker classification.
- To simulate the output of a two camera system providing a single image containing the RGB image along with the selected NIR monochrome image.

Compensation of Edge Effect on Spherical Objects due to Light Source – Hyperspectral Imaging Application

To implement the algorithm to determine the compensation factor for the images of citrus fruits to reduce the blackening effect at the edges of the fruit, was the lead goal of this study which was achieved with the help of the following intermediate goals:

- To correct the images for the spatial variations of light source using a flat white panel of known reflectance
- To produce a 3-D model (digital elevation model-DEM) of the citrus fruit by assuming it to be Lambertian ellipsoidal surface from its 2-D image
- To derive the geometric correction to correct the images for edge effect using the geometric properties (Cartesian coordinates) of the fruit obtained from the DEM
- To validate that the images of citrus fruits corrected using the estimated compensation factor have similar reflectance throughout the fruit surface, minimizing the edge blackening effect.

CHAPTER 3 LITERATURE REVIEW

The citrus industry plays a very crucial role in improving the economy of the State of Florida. Being the growers of world class citrus fruits, Florida farmers are very concerned about not only the quality but also the cost effectiveness of the citrus production. The citrus groves are usually spread over large acreages and hence it demands significant labor to manage the groves and to control the pests. Also this is a very time consuming and expensive job which needs to be done periodically. Apart from all this, as the citrus fruits are produced in large quantity and they need to be inspected for diseases which is also labor intensive and costly. Hence the citrus growers are intending to use some automation application to assist managing their citrus groves and the crops more economically.

There are two types of such automation applications usually found in agricultural industry; one type is used for infield applications and other for indoor, packaging applications. As most of these applications make use of some kind of machine vision, image acquisition and processing technique, most of the infield applications are influenced more by the intensity of light and ambient conditions than that of the indoor applications. In recent studies, researchers have exploited computer vision techniques coupled with pattern classification algorithms for agricultural applications such as disease and defect detection, segregation of fruits and vegetables, identifying fruits in the tree canopy, etc. This chapter is dedicated to introduction of the previous research in the field of agriculture based machine vision applications. We will start with the background information of one of the most serious diseases which Florida citrus industry is facing.

Citrus Canker

The geographical origin of citrus canker is a matter of controversy. However researchers have suggested that canker might have initiated in the tropical regions of Asia i.e., South China, Indonasia, India, etc., where the citrus species are presumed to be originated (Schubert et al., 2001; Das 2003). Citrus canker has spread all over the world and is now in more than thirty countries in Asia, the Pacific and Indian Ocean Islands, South America and Southern-Eastern USA. Some areas of the world (e.g., South Africa, Australia, the Fiji Islands, Mozambique, and New Zealand) have eradicated citrus canker completely. However active ongoing eradication programs still continue in other infected areas such as Argentina, Uruguay, Brazil, and Florida (Schubert et al., 2001). It should be noted that in recent years, Florida has abandoned the eradication program since the disease has become endemic.

Citrus canker usually occurs in regions with warm, humid and cloudy climate. This disease is primarily caused by the bacterium named *Xanthomonas axonopodis* pv. *citri*. Citrus canker was first found Florida around 1912 and then it spread all over the state in the last few decades. The Citrus Canker Eradication Program (CCEP), initiated by the Florida Department of Agriculture and Consumer Services - Division of Plant Industry (FDACS-DPI) and the United States Department of Agriculture - Animal and Plant Health Inspection Service (USDA-APHIS) in mid 1990's, was an attempt to alleviate the consequences that canker would have on the Florida citrus industry, as well as to keep other U.S. citrus-producing areas (e.g., Texas and California) from being infected and harmed by this disease. Because canker exhibits endemic features in most infected regions, there is no universal treatment or prevention that could completely eradicate the disease in all the infected areas. The current emphasis is put on minimizing the level

of the disease and preventing its further spread to the areas that are unaffected or were already eradicated. The presence of cankerous fruit in a shipment could result in the whole shipment being deemed unmarketable to some 'canker-free' areas, such as the European countries.

Citrus canker is characterized by several symptoms on tree leaves, stems and fruits. The symptoms on leaves at initial stage include slightly raised tiny blister-like lesions which at later stage turn tan to brown. The center of the lesion becomes raised and corky. The lesions are usually visible on both sides of the leaf. Symptoms on twigs and fruit are similar and consisted of dark brown or black raised corky lesions surrounded by an oily or water-soaked margin. As the lesions mature, they appear scabby or corky. Lesions cause blemishes and early fruit drop, and hence results in reduced fruit yield. Defoliation, premature fruit drop, twig dieback, general tree decline, and very bad blemishes on fruit are the results of severe infestation. The canker infected trees become weak, unproductive, and unprofitable. The cankerous citrus fruits are unacceptable to the market but as canker is not harmful to human beings the juice market does not get affected because of canker. Citrus canker is extremely infectious and can be spread rapidly by wind-driven rain, storm events such as tornadoes and tropical storms, flooding, equipment, and human movement within groves (Zekri et al., 2005).

Image Processing Techniques Used in Agriculture

Burks et al. (2000) used the color co-occurrence method (CCM) and neural network for classifying weed species. They extracted a total of 33 features using CCM which were analyzed using SAS discriminant procedure STEPDISC. They reported poor classification performance for feature models consisting only hue features or only

saturation features. The neural network with back-propagation demonstrated the capability for identification of weed species with classification rates as high as 96.7%. The individual species were also classified with classification accuracies of 90.0%.

Pydipati et al. (2006) also used the color co-occurrence method (CCM) to analyze if it is possible to identify diseased and normal citrus leaves using texture based hue, saturation and intensity (HSI) color features along with statistical classification algorithms like SAS STEPDISC, under laboratory conditions. They created three CCM matrices, one each for H, S and I, using spatial grey level dependence matrices (SGDM's) which then were used to generate the texture features. A total of 39 features (13 each for H, S and I) were generated. The SAS statistical analysis using procedure called STEPDISC was conducted to reduce redundancy in texture feature set and to create different data models. The leaf sample discriminant analysis using CCM textural features achieved classification accuracies of over 95% for all diseases when using hue and saturation texture features. Classification models based on intensity features alone, resulted in a reduction in classification accuracy when analyzing leaf fronts, due to the darker pigmentation of the leaf fronts unlike the leaf backs where the lighter pigmentation clearly revealed the disease discoloration. The overall best performance was determined with a reduced data model that relied on hue and saturation features only even if high accuracies were achieved when using an unreduced dataset consisting of all HSI texture features. This model was selected due to reduced computational load and the elimination of intensity features, which were not robust in the presence of ambient light variation. From the study of Burks et al. (2000) and

Pydipati et al. (2006), it can be concluded that if only hue, only saturation or only intensity features are used alone for classification, the classifier perform poorly.

Pydipiti et al. (2005) also tried to apply pattern recognition algorithms like statistical and neural network classifiers for detection of diseases on citrus leaves. The 39 texture features were generated (using SGDM's) from the citrus leaf samples and redundancy in the texture features was reduced (using SAS STEPDISC) in a similar way to form different data models. In this study they analyzed only backs of the leaves. They applied the following real time classifiers to all the data models and computed the classification accuracies for each of them: 1) statistical classifier using Mahalanobis minimum distance method 2) neural network with back propagation, and 3) neural network with radial basis functions. They used the preliminary classification results of “generalized square distance classifier” (which is a non real time classification approach) as the bench mark for comparing the above real time classification approaches. The Mahalanobis minimum distance classifier gave the overall classification accuracy of 98%, where those for neural network with back propagation and neural network with radial basis functions were 98% and 95%, respectively. All the three classifier agreed that the reduced feature set including hue and saturation features gave the best results due to absence of intensity features, as intensity features may vary a lot in the outdoor lighting conditions.

Park and Chen (2000) studied the texture features of co-occurrence matrix related to distance and direction of neighborhood matrix and wavelength of multispectral images of chicken carcasses to identify the important texture features along with the important wavelengths to classify the carcasses into wholesome and unwholesome

classes. They concluded that variance, sum average, sum variance and sum entropy were the most significant features to identify the unwholesome carcasses while angular second moment was important to differentiate wholesome carcasses at both visible and NIR wavelengths. They could discriminate the unwholesome chicken carcasses with the accuracy of 95.6% using the linear discriminant model with covariance matrix analysis while the accuracy of detection of wholesome carcasses was 97.0% using the quadratic discriminant model with covariance matrix analysis. Both the linear and quadratic models utilized the co-occurrence texture features of spectral images at visible and NIR wavelengths, however the above mentioned optimum accuracies were obtained when spectral image at 570 nm wavelength was used as input to the model.

Recently, Kim et al. (2009) also demonstrated that color imaging and texture feature analysis could be used for differentiating citrus peel diseases under laboratory conditions. Essentially they also followed a similar procedure that was followed by other researchers in this type of study. They developed a color imaging system to acquire the RGB color images from grapefruits. All the captured images were then analyzed using the color co-occurrence method (CCM). To reduce the amount of data for processing a small region of interest (ROI) was selected from each image. These ROIs were then subjected to RGB to HSI (hue, saturation and intensity) domain conversion. To facilitate the use of color co-occurrence method the spatial gray-level dependence matrices (SGDMs) were generated. Total three SGDMs per ROI image were generated. These SGDMs were then used to compute different texture features. 13 texture features per SGDM per image were computed totaling 39 texture features for every image. The appropriate texture features were selected out of those 39 using the stepwise

discrimination procedure by SAS called STEPDISC in order to reduce the redundancy in the texture feature set. They developed four classification models using the SAS procedure called DISCRIM. Out of those four models, HSI_13 which had total 13 texture features from hue, saturation and intensity color space, acquired the best classification results with overall classification accuracy of 96.7%. They also checked the stability of this model which showed that the average classification accuracy for 10 different runs of the model was 96.0% with a standard deviation of 2.3%, which proved that the model HSI_13 is quite stable and could be successfully used for differentiating cankerous citrus peel from other disease conditions under laboratory environment.

Whenever a computer vision system is used to capture images of spherical objects, due to curvature of the object the edges of the objects appear darker than the center. In such cases there is a possibility of these darker areas at the edge being misclassified as diseased by the segregation algorithm (which is used for separation diseased and healthy products). Gomez et al. (2007) presented an algorithm to correct these adverse effects due to curvature of the spherical objects. They modeled the fruit as Lambertian ellipsoidal surface (whose characteristic property is that it reflects light in exactly the same way in all directions regardless of the direction from which it is observed) and created a 3-D model (digital elevation model-DEM) of the fruit from the 2-D image mask of the fruit. This 3-D model – DEM was used to determine the geometric correction factor for each of the pixel of the image. The value of this correction factor was dependant on the location of the pixel. The corrected image had a similar reflectance throughout its surface. This was validated by conducting numerous

experiments which essentially proved that after geometric correction the intensity of radiation becomes uniform over the fruit surface.

Unay and Gosselin (2006) applied the various pattern recognition techniques to identify stem and calyx of apples. They used high resolution digital monochrome camera with four filters centered at 450, 500, 750 and 800 nm with bandwidths 80, 40, 80 and 50 nm, respectively. The method included the following steps: background removal, object segmentation, feature extraction, feature selection, and pattern classification. The image at 750 nm was used for segmentation which segmented the objects by adaptive thresholding. A total of 35 features were extracted for each segmented object. To eliminate the redundant features, sequential floating forward selection (SFFS) method was used. The method selected 9 useful features out of 35 discarding the rest. They tried five different pattern recognition algorithms (linear discriminant classifier, nearest neighbor, fuzzy nearest neighbor, support vector machine and adaboost) and compared their performances. They found the support vector machine to achieve best classification accuracies of 99% for stems and 100% for calyxes using selected feature set. Also 13% of defects on the apple skin were misclassified as stem or calyx. They concluded that along with low contrast and partial segmentation due to erosion if the stem or calyx is located far from the center closer to the edge in the image then it had a higher probability of getting misclassified the reason being the captured images of the spherical object appear darker at edges than center. This observation was found in line with that found by Gomez et al. (2007) during his invention of edge effect compensation algorithm.

Hyperspectral and Multispectral Imaging Based Approaches Used in Agriculture

In the recent years, hyperspectral and multispectral imaging techniques have been developed as useful tools for quality and safety evaluation of food and agricultural products. The hyperspectral imaging technique acquires spatial information across a sequence of individual band in a broad wavelength range, which generates a 3-D image cube with a high spectral resolution. Kim et al. (2001) of the United States Department of Agriculture (USDA) demonstrated such potential with the sample fluorescence and reflectance images of normal apple and an apple with fungal contamination and bruised spots captured using a laboratory based hyperspectral imaging system. He also suggested that such a unique system can also be used for numerous scientific applications.

Qin et al. (2008) analyzed the reflectance images of Ruby Red Grape fruits in the wavelength range of 400-900 nm captured with the help of the portable hyperspectral imaging system for classifying them into marketable and six diseased peel conditions (canker, greasy spot, insect damage, melanose, scab, and windscar). These images were then processed using principle component analysis (PCA) to compress the 3-D hyperspectral image data into useful image features which could then be used to separate cankerous samples from other diseased and marketable peel conditions. The maximum overall canker detection accuracy was of the order of 93.0%. They identified four wavelengths (553, 677, 718, and 858 nm) which could be adopted by the future online real time solution for detecting canker on the sorting machine in packaging industry.

Piron et al. (2007) worked towards determining the optimal combination of wavelength filters for detecting various weed species located within the carrot rows in

the field. An infield multispectral imaging device consisting of a black and white camera coupled with a rotating wheel holding 22 interference filters in VIS-NIR region was used for the study. The quadratic discriminant analysis was used to determine the finest filter combination. The best filter combination selected was 450, 550 and 700 nm which accomplished the overall classification accuracy of 72.0%. They reported better classification rates with an advanced stage of growth.

Although plenty spectral information is fairly useful for laboratory research, the 3-D hyperspectral image cube contains lot of redundant information across wavelength range being captured. Consequently, real-time hyperspectral image acquisition and processing is challenging due to the large amount of data. Hence Lee et al. (2008) made use of correlation analysis (CA) to select multispectral wavelengths from the 3-D hyperspectral image data for defect detection on apples. The VIS-NIR reflectance spectra extracted from the hyperspectral images of apples were used to identify the wavelength pair for detecting the defect regions on apple surface. Such an optimal pair of wavelengths was selected with the help of correlation analysis between band ratio (λ_1/λ_2) or band difference ($\lambda_1-\lambda_2$) and the assigned value for the surface condition (0 = normal or 1 = defect). The best wavelengths obtained with band ratio were 670 and 684 nm while those obtained with band difference were 828 and 734 nm which gave the correlation coefficients of 0.91 and 0.79, respectively. The maximum overall classification accuracy obtained was 92.42% (195 out of 211 defects).

A similar study was conducted by Qin et al. (2009) for detecting canker on citrus fruits. He developed a multispectral method to inspect citrus canker based on band selection from the hyperspectral images. He used both the correlation analysis (CA) and

principle component analysis (PCA) for the band selection and then compared the results of both. He selected two bands using CA (band ratio), and three & four bands using sequential forward CA (band ratio) and two bands using PCA. The overall classification accuracy of two band ratio classifier using correlation analysis (95.7%) was found to be better than that (92.8%) of the two band ratio classifier using principle component analysis. The three and four band ratio classifiers using CA did not perform (94.2% and 93.3%, respectively) as well as two band ratio classifier using CA which suggests that adding more bands in image ratio calculations does not necessarily improve the canker detection accuracy.

Kim et al. (2007) presented a single hyperspectral line scan imaging inspection system with multi-tasking capabilities to detect not only the defects and diseases on the apples but also the fecal contamination on the apples for online real time application. To detect the fecal contamination the fluorescence imaging was used while the defects were identified using reflectance imaging. The fluorescence imaging using band ratio of F660/F530 (fluorescence at particular wavelengths) achieved 100.0% segregation of feces contaminated apples from the non-contaminated ones (irrespective of diseased or healthy). The reflectance imaging using band ratio of R800/R750 (reflectance at particular wavelengths) coupled with SAS discriminant analysis could reach the classification accuracies of 98.0% for healthy apples and 99.4% for defective apples. He is in the process of evaluating the online system to simultaneously acquire the above multispectral reflectance and fluorescence images. He claimed that it is possible to configure the vision system to capture only a few selected spectral channels to speed up the classification rate. Preset rate of detection is three apples / sec; however he is

modifying the hardware and software to improve the detection rate to more than 10 apples / sec. The basic aim of the exploration was to invent an inspection system with multi-tasking capabilities with presently available infrastructure which he seemed to achieve.

Lu (2002) investigated the use of near infrared (NIR) hyperspectral imaging for detection of bruises on apples. His aim was to find out the spectral range and spectral resolution along with development of an algorithm for effective detection of bruises of different stages on different variety of apples (red delicious and golden delicious). He made use of principle component analysis (PCA) coupled with minimum noise fraction transform (MNF) to identify the bruises. He concluded that the spectral range of 1000 nm to 1340 nm with resolution 17.3 nm and 8.6 nm is best suitable for bruise detection on all the variety of apples considered for the study. The best possible correct classification rate for red delicious apples was 88.0% while the worst possible incorrect classification rate was 12.0%. These numbers for golden delicious apples were 94.0% (correct classification) and 7.0% (incorrect classification). He also proposed that with the improved speed of image acquisition and improved detector technology, NIR hyperspectral imaging can be a solution for offline inspection and online sorting of fruit defects.

Hyperspectral and Multispectral Imaging Coupled with Computer Vision and Pattern Classification Approaches

Cheng et al. (2004) presented a new approach which combined the principle component analysis (PCA) along with Fisher's linear discriminant (FLD) to generate the hybrid PCA-FLD method for maximizing the representation and classification effects on the extracted new feature bands (wavelengths). PCA uses orthogonal axes for

dimensionality reduction by performing the eigen decomposition of the data co-variance matrix. However, it is not necessarily good at drawing distinction between patterns, being an unsupervised method. On the other hand FLD makes the data more reliable for classification by projecting the scatter of the data but it is noise sensitive and may not convey enough energy from original data. The hybrid PCA-FLD method maximizes the advantages of the two methods and compensates for the disadvantages by introducing a weighting factor in the computation. He used the hybrid method along with individual methods PCA and FLD to discriminate the damaged (because of excessive chilling) cucumbers from the good ones and finally compared the results to prove that the hybrid PCA-FLD method outperforms the individual PCA and FLD methods.

Aleixos et al. (2001) developed a multispectral system to identify the size, color (ripe or unripe) and skin defects on the citrus fruits using digital signal processors and machine vision techniques. The system was developed for commercial fruit sorting and packaging house for real time classification of fruits based on size, shape, color and defects. The vision system consisted of two cameras, one CCD camera to capture the RGB image while other monochrome camera with an infrared filter centered at 750 nm to capture the infrared band. The infrared band (I) image alone was used to detect the size and shape of the fruit (by applying a simple threshold to segment the fruit from background) while all the R, G, B and I bands were used to detect the color and the surface defects. Two separate DSP's workings in parallel were used to detect the size & shape and color & defects at the same time to minimize the processing time. The color detection was performed with an accuracy of more than 94% in all the categories. The

surface defects were detected with the accuracy of more than 99% in every category along with separation of stem ends from the defects with 100% accuracy.

Park et al. (1997) implemented a multispectral imaging technique to differentiate between wholesome and unwholesome poultry carcasses using neural network algorithm. The multispectral imaging system was designed to capture the images at 540 and 700 nm wavelengths to provide the image information of the carcasses in spectral and frequency domain. Different neural network classifiers were designed to classify between the wholesome and unwholesome carcasses, one of which took the spectral image pixel intensities as input while other took intensities of Fourier power spectra as input. The neural network classifier based on combined spectral image intensities at 540 and 700 nm achieved the best results (among all other models based on spectral image pixel intensities) of 100.0% accuracy for calibration and 93.3% accuracy for validation. On the other hand, the classification accuracies for neural network classifier based on Fourier spectrum pixel intensities were 93.4% for calibration and 90.0% for validation when fast Fourier transform of image intensity data of 700 nm wavelength only were used as inputs for the network. They concluded that the neural network classifier based on spectral image pixel intensities achieved the best results in classifying the carcasses. The architecture of the neural network which gave best results was 512 input nodes, one hidden layer with 32 hidden nodes and the output layer with two output nodes.

CHAPTER 4 OVERVIEW OF MATERIALS AND METHODS

This chapter serves the purpose of describing the methodology used in collecting and preparing the citrus fruit samples (cankerous and non-cankerous), along with hyperspectral imaging system used during this research. It also describes the methods used for the classification of citrus fruits in the diseased and marketable classes. The description of the primary algorithms like correlation analysis (CA) and principle component analysis (PCA) is also discussed. An attempt was made to discover an innovative algorithm to segregate cankerous citrus fruits from non-cankerous citrus fruits, by combining their RGB images with the near infrared (NIR) monochrome images. The chapter also includes the overview of this algorithm. Finally the edge effect compensation algorithm developed by Gomez et al. (2007) which is re-implemented as a part of this study is also described here. In general the methods employed in all the three subsequent chapters are explained in short in this chapter just to provide an overview to the reader. The readers are advised to refer the “Materials and Methods” sub-sections of respective chapters for more in-depth information.

Citrus Samples

Ruby Red grapefruits with normal surface, canker, and five common diseased peel conditions (i.e., greasy spot, insect damage, melanose, scab, and wind scar) were tested in this study. The spread of canker is observed to be more problematic in grape fruits than other citrus fruits especially oranges which is the most ‘in demand’ citrus variety. Because of this fact canker is readily available on grape fruit samples they had been chosen for this study. Color images for each typical peel condition are shown in Figure 4-1. The diseases on the fruit surface show different symptoms. Greasy spot,

melanose, and scab are all caused by fungi, which generate surface blemishes that are formed by infection of immature fruit during the growing season. Greasy spot produces small necrotic specks, and the affected areas are colored in brown to black and exhibit greasy in appearance. Melanose is characterized by scattered raised pustules with dark brown to black in color. Scab appears as corky raised lesions usually with the color of light brown. Different from the fungal diseases, citrus canker is caused by bacteria, and it is featured with conspicuous dark lesions. Most circular in shape, canker lesions vary in size and they are superficial (up to 1 mm deep) on the fruit peel (Timmer et al., 2000). Diameter of the canker lesions tested in this study was approximately in the range of 1-9 mm. Insect damage is characterized by irregular grayish tracks on the fruit surface, which are generated by larvae of leafminers that burrow under the epidermis of the fruit rind. Wind scar, which is caused by leaves, twigs, or thorns rubbing against the fruit, is a common physical injury on the fruit peel, and the scar tissue is generally gray.

Fruit samples were handpicked monthly from a grapefruit grove in Fort Pierce, Florida during a seven-month harvest period from October 2007 to April 2008. Thirty samples for each peel condition were collected for each month if the condition was available. Cankerosus samples were collected all seven months, and the samples with other peel conditions were not obtained every month due to their availabilities. The grapefruit samples with different sizes of canker lesions were used to evaluate the size detection limits for hyperspectral image processing and classification methods.

A total of 960 grapefruits were collected and tested in this study. Numbers of samples for each peel condition are summarized in Table 4-1. All the grapefruits were washed and treated with chlorine and sodium o-phenylphenate (SOPP) at the Indian

River Research and Education Center of University of Florida (UF) in Fort Pierce, Florida. The samples were transported to UF campus in Gainesville, Florida, and stored in an environmental control chamber maintained at 4 °C. The samples were removed from cold storage about 2 hours before imaging to allow them to reach room temperature. During image acquisition, the fruit samples were placed on the rubber cups, which were fixed on the positioning table of the imaging system, to make sure the diseased areas were on the top of each fruit.

Hyperspectral Imaging System

A hyperspectral imaging system was used to acquire reflectance images from citrus samples. Schematic diagram of the system is illustrated in Figure 4-2. It is a push broom; line-scan based imaging system that utilizes an electron-multiplying charge-coupled-device (EMCCD) camera (iXon, Andor Technology Inc., South Windsor, CT, USA). The EMCCD has 1004×1002 pixels and is thermoelectrically cooled to -80°C through a double-stage Peltier device. An imaging spectrograph (ImSpector V10E, Spectral Imaging Ltd., Oulu, Finland) and a C-mount zoom lens (Rainbow CCTV H6X8, International Space Optics, S.A., Irvine, CA, USA) are mounted to the camera. The instantaneous field of view (IFOV) is limited to a thin line by the spectrograph aperture slit (30 μm), and the spectral resolution of the imaging spectrograph is 2.8 nm. Through the slit, light from the scanned IFOV line is dispersed by a prism-grating-prism device and projected onto the EMCCD. Therefore, for each line-scan, a two-dimensional (spatial and spectral) image is created with the spatial dimension along the horizontal axis and the spectral dimension along the vertical axis of the EMCCD. The lighting unit consists of two 21 V, 150 W halogen lamps powered with a DC voltage regulated power supply (TechniQuip, Danville, CA, USA). The light is transmitted through optical fiber

bundles toward line light distributors. Two line lights are arranged to illuminate the IFOV. A programmable, motorized positioning table (BiSlide-MN10, Velmex Inc., Bloomfield, NY, USA) moves citrus samples (five for each run) transversely through the line of the IFOV. One thousand seven hundred and forty line scans were performed for five fruit samples, and 400 pixels covering the scene of the fruit at each scan were saved, generating a 3-D hyperspectral image cube with the spatial dimension of 1740×400 for each band. Spectral calibration of the system was performed using an Hg-Ne spectral calibration lamp (Oriel Instruments, Stratford, CT, USA). Because of inefficiencies of the system at certain wavelength regions (e.g., low light output in the visible region less than 450 nm, and low quantum efficiency of the EMCCD in the NIR region beyond 930 nm), only the wavelength range between 450 and 930 nm (totaling 92 bands with a spectral resolution of 5.2 nm) was used in this investigation. The parameterization and data-transfer interface software for the hyperspectral imaging system were developed using a SDK (Software Development Kit) provided by the camera manufacturer on a Microsoft Visual Basic (Version 6.0) platform in the Windows operating system.

Image Pre-Processing

As mentioned in the earlier section (Hyperspectral Imaging System), each hyperspectral image taken with our system consists of 3-D hyperspectral image cube with spatial dimension of 1740×400 and spectral dimension of 92 (92 wavelengths). To reduce the amount of data for computation, the binning technique was used in which the hyperspectral image data was averaged by two neighboring pixels in both vertical and horizontal spatial dimensions at each wavelength. This reduced the size of the original 3-D image data from 1740×400×92 (92 bands) to 870×200×92, and resulted in a spatial resolution of 0.6 mm/pixel for both vertical and horizontal dimensions. The image

preprocessing procedures described above were executed using programs developed in MATLAB R2007a (Math Works, Natick, MA, USA). Along with this the image preprocessing was performed for the original hyperspectral reflectance images to fulfill flat- field correction and image masking which resulted in normalized and masked hyperspectral cubes with a dimension of 870×200×92 (92 bands). Detailed procedures for hyperspectral image preprocessing are given in the following sections.

Flat field correction

As mentioned in the earlier paragraph, halogen lamps (21 V, 150 W) were used for the illumination in the hyperspectral imaging system. The problem associated with the lighting provided by the halogen lamps is that it suffers with high order of directionality. The above mentioned fact results in varied intensity of the light source in the plane of the scene which is called the spatial variation of light source. In order to take care of this issue, the flat field correction was carried out. During the procedure of the flat field correction the image was pre-processed using a flat white panel of known reflectance. This white panel is usually called a white reference. In this study the white Spectralon panel was used as a reference. The first step was to perform the correction of the hyperspectral image based on the ratio of reflectance of the fruit ($\rho(\lambda)$) and the radiance of the light source ($I(\lambda)$) as denoted by equation (4-1).

$$R(\lambda) = \frac{\rho(\lambda)}{I(\lambda)} \quad (4-1)$$

Where, $R(\lambda)$ is the spatially corrected reflectance image of the fruit. However, the reflectance of the fruit ($\rho(\lambda)$) and the radiance of the light source ($I(\lambda)$) cannot be measured as absolute values using the hyperspectral imaging system. Hence in order

to achieve this correction the white and dark references were used. Therefore the spatial variation of the light source was rectified using the following equation:

$$R(\lambda) = \frac{R_s(\lambda) - R_d(\lambda)}{R_w(\lambda) - R_d(\lambda)} * \Psi_{Ref} \quad (4-2)$$

Where,

λ = Wavelengths

$R_s(\lambda)$ = Original (uncorrected) reflectance image of the fruit

$R_d(\lambda)$ = Reflectance image of dark current

$R_w(\lambda)$ = Reflectance of white reference

Ψ_{Ref} = Reflectance factor of the white reference panel

The dark current image $R_d(\lambda)$ was acquired with the light source off and the camera lens covered with the cap and the white reference image $R_w(\lambda)$ was acquired using the white Spectralon panel. The actual reflectance factor (Ψ_{Ref}) of the white panel was around 98.5% in the wavelength range covered for the study (450 – 930 nm) however in this exploration for simplicity it was assumed to be 100%. The correction mentioned in the equation (4-2) was applied to all the monochrome images in the wavelength range mentioned above. The relative reflectance images processed using above mentioned procedure were then multiplied by a factor of 10,000 so as to achieve the pixel values for resultant images in the range 0 to 10,000. This multiplication factor was applied in order to attain the pixel value range comparable to that of the original data from the hyperspectral imaging camera and also to reduce the round off errors for further data analysis. Further details about the flat field correction can be found in Qin et al. (2008).

Image Masking and Binning

After correcting the images for spatial variation, the mask for the fruit image was created with an intention of removing the noisy background. The mask template was formed by determining the threshold value by visual inspection of one of the monochrome images (765 nm) that had good contrast between fruit surface and the background. The mask was then applied to extract the fruit pixels and remove the background from all the monochrome images in the hyperspectral image cube. The subsequent analysis used these masked images for further processing.

Since hyperspectral image involves a large amount of data, spatial binning technique is used for data reduction. In this process the image data is averaged by few neighboring pixels in horizontal or vertical direction or in both directions (as per requirement) at each wavelength. Image binning was used during first two studies but it was not performed during the third part i.e., edge effect compensation as it was just an experimental study. The algorithms for flat field correction as well as image masking and binning were developed by our research team (Qin et al., 2008) during prior explorations. For further details one can refer to Qin et al. (2008).

Hyperspectral Band Selection Using Correlation Analysis (CA)

Correlation analysis was used as basis for selecting fewer numbers of wavelengths from the high dimensional 3-D hyperspectral image cube in order to reduce the amount of data for computation, in two out of three different studies conducted during the course of this thesis. The correlation analysis (CA) helps to select an optimal pair of wavelengths which can be used to segregate the cankered citrus fruits from normal or other peel conditions. First of all the reflectance spectra of canker, normal and five other disease conditions (greasy spot, insect damage, melanose, scab

and wind scar) were extracted using ENVI 4.3 software (ITT Visual Information Solutions, Boulder, CO, USA). Instead of extracting the reflectance spectra from a single pixel of respective peel condition, it was acquired by averaging over number of pixels by using the region of interest (ROI) tool in ENVI. The ROI was manually selected in the zoom window that contained typical diseased or normal peel areas using various drawing methods (e.g., polygon, rectangle, ellipse, point, grow, and merge) offered by ENVI ROI tools. Enough care was taken to preserve the purity of each of the ROIs in a sense that the whole ROI contained pixels from only one desired peel condition while edge and other undesired pixels were excluded. All the grape fruit samples were used for the ROI selections, and at least one ROI was selected from the representative region for each fruit. The mean reflectance spectrum for each fruit was then computed from merged ROIs within each fruit, which was then used as individual reflectance spectrum for the wavelength selection.

The optimal pair of wavelengths selected by correlation analysis was then used to create the two band ratio image (i.e., $R_{\lambda_1}/R_{\lambda_2}$, where R_{λ_n} denotes single band reflectance image at the wavelength of λ_n) which helped us to make the distinction. Ratio method was chosen because the ratio images are invariant to illumination scaling, which is a significant advantage for real-time applications (Qin et al., 2009). All the fruit samples were divided into two classes: 'Canker' class including samples with canker lesions, and 'No Canker' class including normal samples and samples with other five peel diseases. To facilitate the correlation analysis, samples in the 'Canker' class were labeled with '1', and 'No Canker' class with '0'. Then two vectors were generated, one of them was the vector containing ratio of reflectance at respective wavelengths and other

was the vector containing all the label values (i.e., 1 and 0) (Qin et al., 2009). Also it should be noted that there was one vector of ratio of reflectance for each band combination. Correlation coefficients were then calculated comprehensively for every possible two band combination (from 46 bands), between these two vectors i.e., the vector of ratio of reflectance between corresponding band combination and the vector of label values (Qin et al., 2009). The pair of bands which gave the maximum value for the correlation coefficient (which is nothing but the optimum pair mentioned earlier) was selected for further classification study. The detailed procedure for selecting the optimal pair of wavelengths can be found in Qin et al. (2009).

Image Classification

After identifying important wavelengths using CA, band ratio images were generated using ENVI 4.3 software (ITT Visual Information Solutions, Boulder, CO, USA) and the selected wavelength's single band images. The equation $R_{\lambda 1}/R_{\lambda 2}$ was used to create these new ratio images. A simple thresholding approach, which has been used to differentiate cancerous fruits from six other peel conditions (normal peel and other citrus diseases), was applied to the ratio images calculated using the above equations. Different threshold values were used to evaluate classification accuracies for canker identification. A morphological filtering operation followed thresholding, in order to remove undesirable noise (small pixel regions attributed to edge affects and other peel conditions) from the image as these small pixel regions can result in an increase in false positives. It is recognized that this filtering operation can inhibit detection of very small canker lesions, and thus creates a tradeoff between the number of false positives, and false negatives. The morphological "opening" operation was applied to the thresholded image, which by definition means erosion of the image followed by

subsequent dilation. The opening filter from the ENVI morphological filter tools with a kernel size of 3×3 was selected. The purpose of erosion was to remove the undesired small size pixels, with dilation smoothing out the contours of the remaining pixel areas to help restore the round feature of the canker lesions in the final binary images. The method of image classification is demonstrated in Figure 4-3.

Principle Component Analysis (PCA)

As already have mentioned the hyperspectral data has a lot of redundancy. Principal component analysis is one of the many variable reduction techniques which can be employed to remove such redundancy from the hyperspectral data. When the variables of the data are interrelated (i.e., correlated) with one another, possibly because they provide somewhat similar type of information, they are called redundant. Because of this fact it is always possible to reduce the observed variables into a smaller number of artificial variables that accounts for most of the variance in the observed variables. These artificial variables are known as Principle Components. In simple words, a principle component can be defined as a linear combination of optimally weighted observed variables (SAS customer support, 2010). Usually we can extract as many principle components as number of observed variables. However, in most of the explorations only the first few principle components account for meaningful amount of variance and hence only these principle components are retained for further analysis (Palmer, M.). In our case of 3-D hyperspectral data the number of observed variables are nothing but the number of monochrome images (i.e., number of bands) being analyzed and after principle component analysis approximately only first ten components are chosen for detecting the diseases or defects on the biological products.

The few, very important characteristics of the PCA are as follows (SAS customer support, 2010). The first principle components accounts for maximum amount of the total variance in the observed variables. The second and all the preceding components account for the maximum amount of variance in the dataset that was not accounted for by the previous principle components. Also all the principle components are totally uncorrelated with all the previous principle components. So the principle components analysis proceeds in this manner accounting for progressively smaller and smaller amount of variance and this is the reason why we usually retain only first few principle components for further analysis.

The principle component analysis involves the eigenvalue decomposition of the data covariance matrix after mean centering the data for each observed variable (Duda, Hart, Stork, 2004; Bishop, 2006). As the covariance matrix of the data is real and symmetric all the eigenvectors are orthogonal to each other (by characteristic property of a real symmetric matrix). These eigenvectors are the directions (which are called principle axes) along which the data is projected during principle component analysis. In simple terms in principle component analysis, all the data points are projected along the axes those pass through the mean of the data and are mutually orthogonal. Hence PCA is also called orthogonal linear transformation.

Estimation of Detection Limit for Size of Citrus Canker Lesions Based on Hyperspectral Imaging

Overview of the procedure: This study was aimed at estimating the ability of previously developed multispectral algorithm using correlation analysis (Qin et al., 2009), to detect as small canker lesions as possible. The objective was to detect the size of the smallest canker speck in terms of equivalent diameter that can be detected

by the algorithm. The hyperspectral imaging system used for the study was the same as mentioned before in this chapter. The optimal wavelengths were detected using correlation analysis and the image classification method explained in Figure 4-3 was applied to the ratio images (ratio of reflectance images at the selected wavelengths) to create the binary images which highlight canker. Once the binary images were created they were subjected to the smallest lesion estimation algorithm to determine the smallest canker lesion in binary images. These smallest canker lesions in the binary images were then mapped to the actual hyperspectral images to determine the actual size of the lesion in the final stage of the algorithm. The Chapter 5 of this thesis is dedicated to this study and the procedure and computer algorithms are explained in great depth in that chapter.

Detection of Citrus Canker Using RGB Color Image Along with NIR Monochrome Images

Overview of the procedure: The efforts have been made to implement a novel algorithm to detect citrus canker. The algorithm makes use of the visible and NIR wavelengths of hyperspectral image as separate channels lumped together to create a single image. More specifically the RGB color image of the fruit was simulated from the single band images in the visible range (450-700 nm) from the hyperspectral data captured during previous studies. This RGB color image was then mosaicked with the remaining single band images (700-930 nm) to create the image for further analysis. The resulting image was then processed further using correlation analysis (CA) to identify the key wavelengths in the NIR region which will help separating the cankerous citrus fruit from fruits of other peel conditions. The hyperspectral imaging system used was the same as mentioned earlier this chapter. After detecting the key wavelengths

using correlation analysis images were subjected to image classification approach explained in Figure 4-3. The basic objective behind this was to simulate the output of the two camera system installed on the packaging line, including one CCD camera (outputting the RGB image) and one monochrome camera (outputting the single NIR wavelength image) to provide four channels red, green, blue and NIR wavelength which in turn would be used to detect canker. For the detailed explanation of procedure followed and algorithm implemented one can refer to Chapter 6.

Compensation of Edge Effect on Spherical Objects due to Light Source – Hyperspectral Imaging Application

Overview of the Procedure: When the image of a spherical object like a citrus fruit or an apple is captured by any kind of computer vision system, the central area of the fruit appear brighter while the edges emerge out to be darker. When such fruit images undergo some type of automatic segregation system the classification algorithm usually confuses the darkened edges of the fruit as a disease or defect and misclassifies the fruit. This effect where the edges of the fruit appear much darker than the central region when captured by a camera, is called the edge effect. In order to avoid the misclassification two types of corrections are applied to the image. The first is the spatial correction and other is called geometric correction. The light sources like halogen lamps (which are used in the hyperspectral imaging system used in this study) offer high degree of dimensionality which results in spatial variations in the intensity of light source in the plane of the scene (Gomez et al., 2007). These variations are taken care of with the flat field correction procedure mentioned earlier. The geometric correction is required to correct the edge effect which takes the geometric shape of the fruit into account and rectifies the darkening effect. In order to derive the geometric

correction, a 3 dimensional model of the fruit called digital elevation model (DEM) had been developed from its 2 dimensional image. This DEM was used to extract the geometric properties (X, Y, Z Cartesian coordinates) of the fruit which were exploited to estimate the geometric correction factor for each pixel. The detailed description of the algorithm can be found in Chapter 7.

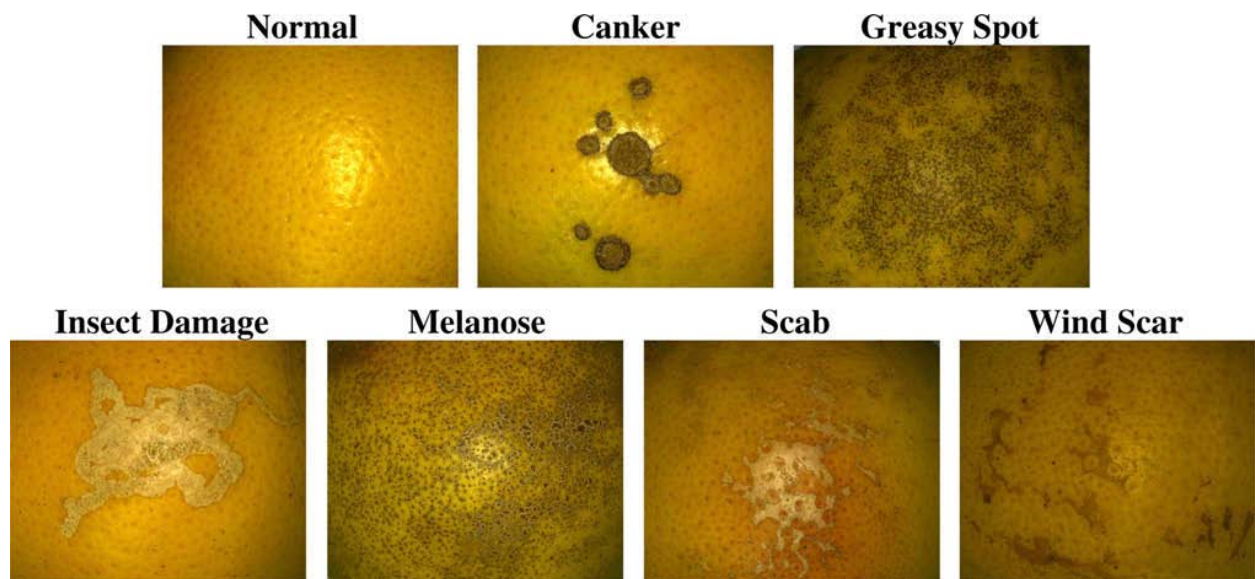


Figure 4-1: Representative normal and diseased peel conditions of grapefruit samples

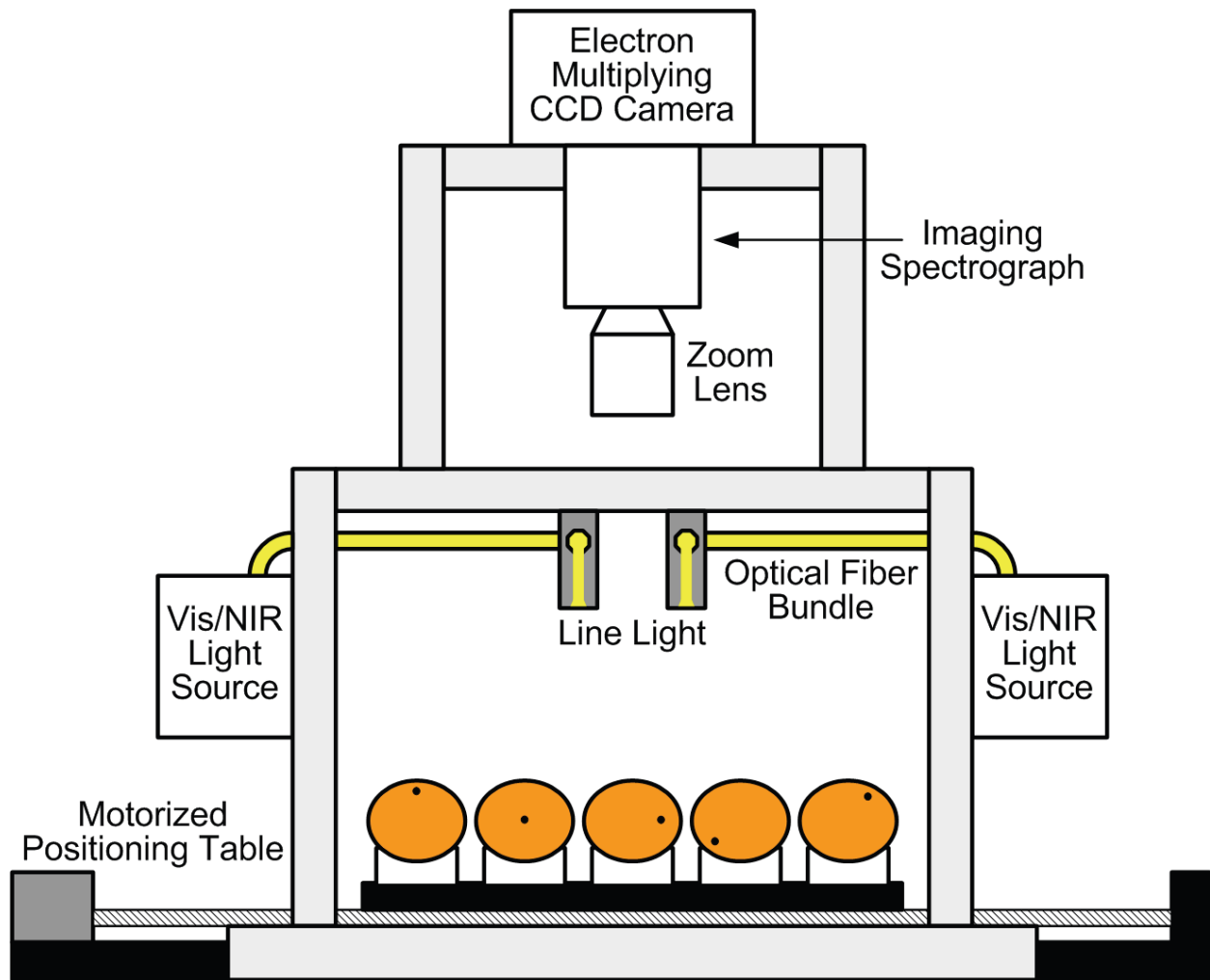


Figure 4-2: Hyperspectral imaging system for reflectance image acquisition from grapefruits

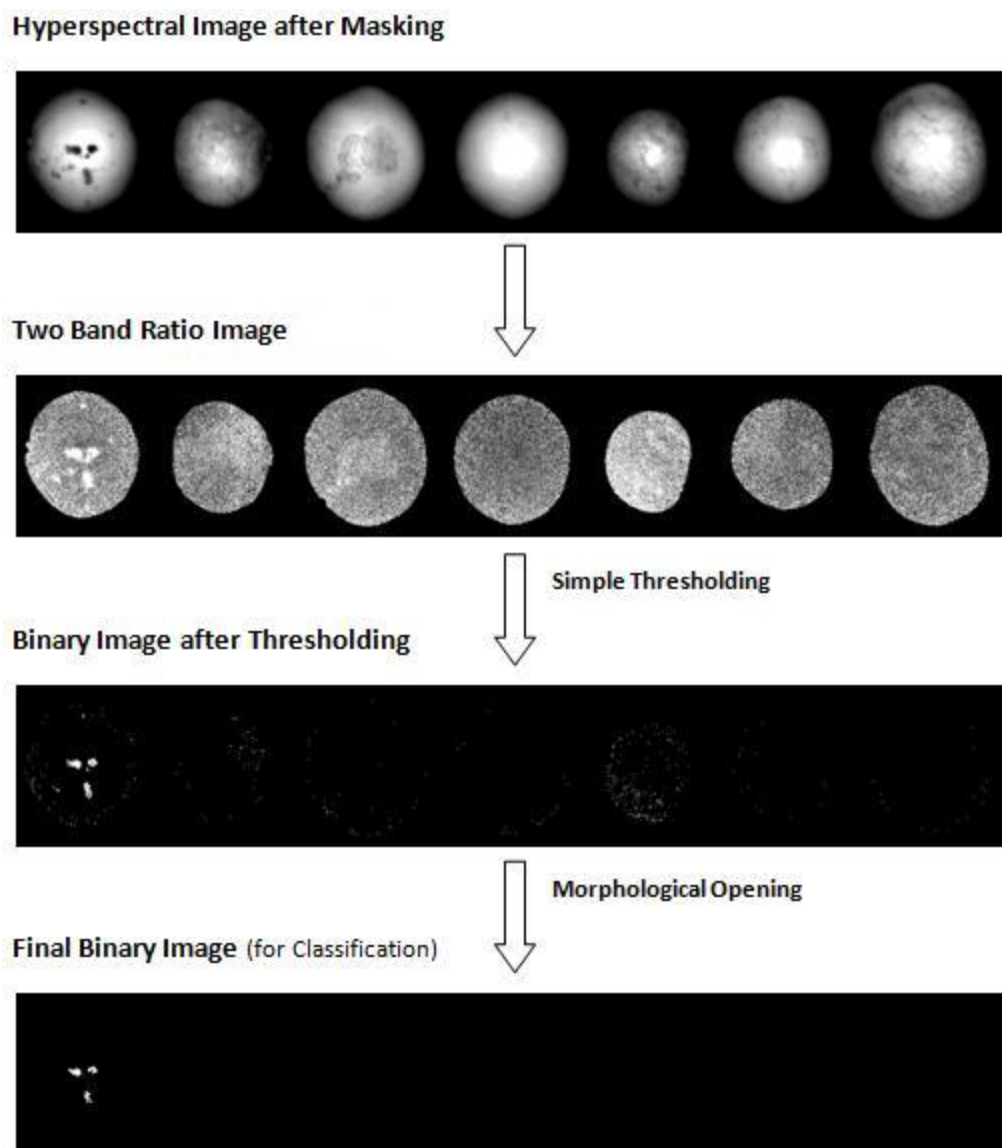


Figure 4-3: Image classification procedure

Table 4-1: Numbers of fruit samples for each peel condition

Peel Condition	Canker	Normal	Greasy Spot	Insect Damage	Melanose	Scab	Wind Scar
Number	210	150	120	60	180	180	60

CHAPTER 5 ESTIMATION OF DETECTION LIMIT FOR SIZE OF CITRUS CANKER LESIONS BASED ON HYPERSPECTRAL REFLECTANCE IMAGING

Introduction

Citrus canker is a serious disease that can infect most commercial citrus varieties. Caused by bacterial pathogen *Xanthomonas axonopodis*, the disease is characterized by conspicuous, erumpent lesions on leaves, stems, and fruit. Citrus canker originated in Southeast Asia-India, and it has spread to Japan, South and Central Africa, the Middle East, Australia, New Zealand, the Pacific Islands, South America, and Florida (Schubert et al., 2001). Some areas of the world (e.g., South Africa, Australia, the Fiji Islands, Mozambique, and New Zealand) have eradicated citrus canker. Eradication programs have been implemented in infected areas such as Argentina, Uruguay, Brazil, and Florida. Citrus canker could cause defoliation, blemished fruit, premature fruit drop, twig dieback, and tree decline. Due to its fast spread, high damage potential, and massive impact on export and domestic trade, canker is considered as one of the most devastating diseases that threaten all citrus-growing areas.

Florida produces more than 70 percent of the citrus supply in the United States, and it is the only growing region in the U.S. that is affected by canker. The Citrus Canker Eradication Program (CCEP), initialized by the Florida Department of Agriculture and Consumer Services - Division of Plant Industry (FDACS-DPI) and the United States Department of Agriculture - Animal and Plant Health Inspection Service (USDA-APHIS) in mid 1990's, was an attempt to alleviate the consequences that canker would have on the Florida citrus industry, as well as to keep other U.S. citrus-producing areas (e.g., Texas and California) from being infected and harmed by this disease. Because canker exhibits endemic features in most infected regions, there is no

universal treatment or prevention that could completely eradicate the disease in all the infected areas. The current emphasis has been on minimizing the level of the disease and preventing its further spread to the areas that are unaffected or were already eradicated. Recently, the Florida eradication program has been terminated since citrus canker is now considered endemic. In certain international canker-free markets, the presence of cankerous fruit in a shipment could result in the whole shipment being deemed unmarketable. It has been the common practice to detect citrus canker and eliminate the infected fruit before they go to the market.

In recent years, Florida had been the only US state under quarantine for citrus canker and therefore could not ship canker blemished fruit within the US or to other countries those block shipment of canker infected fruit. In the fall of 2009, USDA APHIS issued a new ruling based on research which demonstrated that canker cannot be transmitted by infected fruit that had been treated with an appropriate disinfectant (USDA APHIS, 2009). The ruling lifts the within US blockade and now allows free shipment of disinfected fruit. However, there still remain several international markets that have not lifted the ban on canker infected fruit to date.

Finding and removal of citrus fruit with canker is currently performed by human inspectors in the packing house, which is labor-intensive and time-consuming. Technologies that can efficiently identify citrus canker would assure fruit quality and safety, which would enhance the competitiveness and profitability of the citrus industry. Also sometimes the canker lesions are so small that they cannot be readily identified by human eyes, and yet if such fruits are included in the shipment, they can cause the entire shipment to be rejected at the port of entry into some markets. A number of

optical sensing techniques (e.g., machine vision and spectroscopy) have been investigated to detect citrus-related diseases and defects, such as fruit blemish features (Miller and Drouillard, 2001), leaf diseases (Pydipati et al., 2006), fruit surface defects (Blasco et al., 2007), fruit rottenness (Gómez- Sanchis et al., 2008) and citrus canker detection using limited number of hyperspectral wavelengths (Qin et al., 2009b). However, only limited efforts have been made to detect the size of the smallest possible canker affected lesion.

In the recent years, hyperspectral and multispectral imaging techniques have been developed as useful tools for quality and safety evaluation of food and agricultural products. The hyperspectral imaging technique acquires spatial information across a sequence of individual band in a broad wavelength range, which generates a 3-D image cube with a high spectral resolution. Although a large amount of spectral information is useful for laboratory research, the hyperspectral cube contains redundant information across tens or hundreds of bands. Consequently, real-time hyperspectral image acquisition and processing is challenging due to the large amount of data. Hyperspectral band selection, therefore, is usually performed to find a subset containing few significant wavelengths (usually less than ten) with an aim of useful information extraction and image dimensionality reduction.

Our recent studies (Qin et al., 2008, 2009a,b) have demonstrated that hyperspectral imaging technique coupled with appropriate image processing and classification methods [i.e., principal component analysis (PCA) and spectral information divergence (SID), etc.] provides a useful means for detecting canker lesions on citrus fruit. However, the full spectral information used by the PCA and SID

algorithms would limit their applications such as rapid on-line disease inspection due to the large amount of 3-D hyperspectral data. Hence our team (Qin et al., 2009b) has built a technique to select a set of hyperspectral bands for citrus canker detection using multispectral algorithms in which the correlation analysis has been used to identify important wavelengths for citrus canker detection based on hyperspectral reflectance data. The objective of this particular research was to develop an algorithm to detect the smallest possible canker affected lesion for real time online application, using the previously urbanized multispectral algorithm.

Materials and Methods

Citrus Samples

Ruby Red grapefruits with normal surface, canker, and five common diseased peel conditions (i.e., greasy spot, insect damage, melanose, scab, and wind scar) were tested in this study. Color images for each typical peel condition are shown in Figure 5-1. The diseases on the fruit surface show different symptoms. Greasy spot, melanose, and scab are all caused by fungi, which generate surface blemishes that are formed by infection of immature fruit during the growing season. Greasy spot produces small necrotic specks, and the affected areas are colored in brown to black and exhibit greasy in appearance. Melanose is characterized by scattered raised pustules which are dark brown to black in color. Scab appears as corky raised lesions usually with the color of light brown. Different from the fungal diseases, citrus canker is caused by bacteria, and it is featured with conspicuous dark lesions. Most circular in shape, canker lesions vary in size and they are superficial (up to 1 mm deep) on the fruit peel (Timmer et al., 2000). Diameter of the canker lesions tested in this study was approximately in the range of 1-9 mm. Insect damage is characterized by irregular grayish tracks on the fruit surface,

which are generated by larvae of leafminers that burrow under the epidermis of the fruit rind. Wind scar, which is caused by leaves, twigs, or thorns rubbing against the fruit, is a common physical injury on the fruit peel, and the scar tissue is generally gray.

Fruit samples were handpicked monthly from a grapefruit grove in Fort Pierce, Florida during a seven-month harvest period from October 2007 to April 2008. Thirty samples for each peel condition were collected for each month if the condition was available. Cankerosus samples were collected all seven months, and the samples with other peel conditions were obtained every month according to their availabilities. The grapefruit samples with different sizes of canker lesions were used to evaluate the size detection limits for hyperspectral image processing and classification methods.

A total of 960 grapefruits were collected and tested in this study. Numbers of samples for each peel condition are summarized in Table 5-1. All the grapefruits were washed and treated with chlorine and sodium o-phenylphenate (SOPP) at the Indian River Research and Education Center of University of Florida (UF) in Fort Pierce, Florida. The samples were transported to UF campus in Gainesville, Florida, and stored in an environmental control chamber maintained at 4 °C. The samples were removed from cold storage about 2 hours before imaging to allow them to reach room temperature. During image acquisition, the fruit samples were placed in rubber cups attached to the linear positioning table, with lesions facing upward, to insure that the diseased areas were in the imaging systems field of view.

Hyperspectral Imaging System

A hyperspectral imaging system was used to acquire reflectance images from citrus samples. A schematic diagram of the system is illustrated in Figure 5-2. This hyperspectral imaging system was developed in cooperation with the USDA

Environmental Microbial and Food Safety Laboratory in Beltsville, MD, and is conceptually similar to the system reported in Qin et al. (2008). It is a push broom, line-scan based imaging system that utilizes an electron-multiplying charge-coupled-device (EMCCD) camera (iXon, Andor Technology Inc., South Windsor, CT, USA). The EMCCD has 1004×1002 pixels and is thermoelectrically cooled to -80°C through a double-stage Peltier device. An imaging spectrograph (ImSpector V10E, Spectral Imaging Ltd., Oulu, Finland) and a C-mount zoom lens (Rainbow CCTV H6X8, International Space Optics, S.A., Irvine, CA, USA) are mounted to the camera. The instantaneous field of view (IFOV) is limited to a thin line by the spectrograph aperture slit (30 µm), and the spectral resolution of the imaging spectrograph is 2.8 nm. Through the slit, light from the scanned IFOV line is dispersed by a prism-grating-prism device and projected onto the EMCCD. Therefore, for each line-scan, a two-dimensional (spatial and spectral) image is created with the spatial dimension along the horizontal axis and the spectral dimension along the vertical axis of the EMCCD. The lighting unit consists of two 21 V, 150 W halogen lamps powered with a DC voltage regulated power supply (TechniQuip, Danville, CA, USA). The light is transmitted through optical fiber bundles toward line light distributors. Two line lights are arranged to illuminate the IFOV. A programmable, motorized positioning table (BiSlide-MN10, Velmex Inc., Bloomfield, NY, USA) moves citrus samples (five for each run) transversely through the line of the IFOV. One thousand seven hundred and forty line scans were performed for five fruit samples, and 400 pixels covering the scene of the fruit at each scan were saved, generating a 3-D hyperspectral image cube with the spatial dimension of 1740×400 for each band. Spectral calibration of the system was performed using an Hg-Ne spectral

calibration lamp (Oriel Instruments, Stratford, CT, USA). Because of inefficiencies of the system at certain wavelength regions (e.g., low light output in the visible region less than 450 nm, and low quantum efficiency of the EMCCD in the NIR region beyond 930 nm), only the wavelength range between 450 and 930 nm (totaling 92 bands with a spectral resolution of 5.2 nm) was used in this investigation. The parameterization and data-transfer interface software for the hyperspectral imaging system were developed using a SDK (Software Development Kit) provided by the camera manufacturer on a Microsoft Visual Basic (Version 6.0) platform in the Windows operating system.

Image Pre-Processing

As mentioned in the earlier section (Hyperspectral Imaging System), each hyperspectral image taken with our system consists of 3-D hyperspectral image cube with spatial dimension of 1740×400 and spectral dimension of 92 (92 wavelengths). To reduce the amount of data for computation, spatial binning technique was used in which the hyperspectral image data was averaged by two neighboring pixels in both vertical and horizontal spatial dimensions at each wavelength. This reduced the size of the original 3-D image data from 1740×400×92 (92 bands) to 870×200×92, and resulted in a spatial resolution of 0.6 mm/pixel for both vertical and horizontal dimensions. The image preprocessing procedures described above were executed using programs developed in MATLAB R2007a (Math Works, Natick, MA, USA). Along with this the image preprocessing was performed for the original hyperspectral reflectance images to fulfill flat-field correction and image masking which resulted in normalized and masked hyperspectral cubes with a dimension of 870×200×92 (92 bands). Detailed procedures for hyperspectral image preprocessing can be found in Qin et al. (2008).

Hyperspectral Band Selection

The goal of this research was to determine the minimum size limit at which citrus canker lesions can be reliably detected for real time packing line applications. However, we must first have an effective approach to segregate cankerous citrus fruits from normal peel or other surface defects. The disease defect classification approach implemented in this study used a real-time multispectral algorithm based on correlation analysis for band selection (Qin et al., 2009b).

Even after preprocessing the image data, the 3-D hyperspectral data (870×200×92) is still too large for rapid real time applications and hence a multispectral algorithm is needed that uses a subset of the hyperspectral data to reduce the computation time thus making it more suitable for online applications. The multispectral algorithm exploits correlation analysis (CA) to select the optimal pair of wavelengths that can be used to distinguish between cankered, normal, and other diseased peel conditions. In this method, the selected optimal pair of wavelengths is used to create the two band ratio image (i.e., $R_{\lambda_1}/R_{\lambda_2}$, where R_{λ_n} denotes single band reflectance image at the wavelength λ_n) which helps us to make the distinction. Ratio method was chosen because the ratio images are invariant to illumination scaling, which is a significant advantage for real-time applications. All 960 fruit samples were divided into two classes: 'Canker' class including 210 samples with canker lesions, and 'No Canker' class including 150 normal samples and 600 samples with other five peel diseases (see Table 5-1). To facilitate correlation analysis, samples in the 'Canker' class were labeled with '1', and 'No Canker' class with '0'. Correlation coefficients were calculated between two band ratios of the ROI spectra and the fruit label values (i.e., 1 and 0) in an exhaustive way (i.e., evaluating all possible two band combinations from 92 wavelengths). The pair

of wavelengths which gave the maximum value for the correlation coefficient (the optimum pair previously mentioned) was selected for further classification and lesion size estimation.

Keeping in mind that selecting more additional wavelengths may (or may not) improve classification accuracies, the third and fourth bands were identified by performing the correlation analysis in a sequential forward way. The third band (i.e., R_{λ_3}) was determined by the highest correlation between the fruit label values and ratio values calculated in a form of $(R_{\lambda_1} - R_{\lambda_3})/(R_{\lambda_2} - R_{\lambda_3})$, where R_{λ_1} and R_{λ_2} were two best bands selected from the previous correlation analysis. After the third band was determined, the fourth band was identified using the similar method on two forms of ratio calculations: $(R_{\lambda_1} - R_{\lambda_3})/(R_{\lambda_2} - R_{\lambda_{4a}})$ and $(R_{\lambda_1} - R_{\lambda_{4b}})/(R_{\lambda_2} - R_{\lambda_3})$, where R_{λ_1} , R_{λ_2} , and R_{λ_3} were determined from the previous procedures, and $R_{\lambda_{4a}}$ and $R_{\lambda_{4b}}$ were newly selected bands from the highest correlations. However, as demonstrated in previous studies (Qin et al., 2009b), the two band ratio method gives the best overall classification results and hence this study is an extension of the earlier two band ratio approach. The two bands ratio of 834 nm and 729 nm (R_{834}/R_{729}) was found to give the maximum absolute value for the correlation coefficient of 0.811 and hence was chosen to be the optimal pair of wavelengths to discriminate between fruit exhibiting cankerous and other peel conditions. The detailed procedure for selecting the optimal pair of wavelengths can be found in Qin et al. (2009b).

Image Classification

After identifying important wavelengths using CA, band ratio images were generated using ENVI 4.3 software (ITT Visual Information Solutions, Boulder, CO, USA) and the selected wavelength's single band images. The equation $R_{\lambda_1}/R_{\lambda_2}$ (i.e.,

R_{834}/R_{729}) was used to create these new ratio images. A simple thresholding approach, which has been used to differentiate cancerous fruits from six other peel conditions (normal peel and other citrus diseases), was applied to the ratio images calculated using the above equations. Different threshold values were used to evaluate classification accuracies for canker identification. A Morphological filtering operation followed thresholding, in order to remove undesirable noise (small pixel regions attributed to edge affects and other peel conditions) from the image as these small pixel regions can result in an increase in false positives. It is recognized that this filtering operation can inhibit detection of very small canker lesions, and thus creates a tradeoff between the number of false positives, and false negatives. The morphological “opening” operation was applied to the thresholded image, which by definition means erosion of the image followed by subsequent dilation. The opening filter from the ENVI morphological filter tools with a kernel size of 3×3 was selected. The purpose of erosion is to remove the undesired small size pixels, with dilation smoothing out the contours of the remaining pixel areas to help restore the round feature of the canker lesions in the final binary images.

Binary Lesion Size Detection Algorithm

To determine the smallest canker lesion detected by the above mentioned image classification algorithm, the classified images (Final Binary Images) of the samples were examined. For this task also morphological opening operation was used. The function ‘bwareaopen’ in MATLAB R2007a (Math Works, Natick, MA, USA) was used to determine the number of pixels in the smallest canker lesion detected during the classification process. The function ‘bwareaopen’ removes all connected components (objects) from a binary image that have fewer than certain number of pixels defined in

the syntax, producing another binary image. The number of pixels defined in the syntax was incremented by one at a time and the image before and after applying 'bwareaopen' function were compared for consistency. Whenever some difference was observed between the two images, the number of pixels (defined in syntax of 'bwareaopen') was noted. This pixel count minus one represented the number of pixels (N) in the smallest canker lesion detected in the binary image by the lesion size estimation algorithm.

Mapping Binary Lesion Size to Original Hyperspectral Image

The smallest size lesions obtained by following the above procedure were found in the binary image. Consequently, to obtain an accurate size estimate for the smallest lesion, it was necessary to map the lesion found in the binary image back to the un-eroded lesion in the original hyperspectral image. This was done using ENVI. The X and Y coordinates of the centroid of binary canker lesion (which was detected to be the smallest) were estimated using MATLAB and corresponding lesion in the original hyperspectral image was located. The number of pixels (N) in the original hyperspectral image lesion was counted using the region of interest (ROI) tool in Basic Tools of ENVI.

The spatial resolution of the images was 0.6 mm/pixel in horizontal direction and 0.6 mm/pixel in vertical direction. Hence the surface area of one pixel is 0.6×0.6 sq. mm. Accordingly the surface area of the smallest canker lesion (A) was computed from the number of pixels in the lesion and area per pixel. Then assuming that most canker lesions are approximately circular in shape, the equivalent diameter (d) of the lesion was computed from the following formula:

$$A = \pi d^2/4 \quad (5-1)$$

Results, Observations and Discussion

Image Classification Results

As demonstrated in a previous study (Qin et al., 2009b) it is not possible to detect the citrus canker using a single wavelength, and hence a multispectral imaging solution utilizing information acquired from the hyperspectral bands was developed. The multispectral algorithm explained in previous sections is illustrated in Figure 5-3, where the various image processing steps necessary to generate the final thresholded binary image of a canker infected fruit is shown. In this approach, the two band ratio method (R_{834}/R_{729}) has been applied. As mentioned previously, an important fact that should be remembered is that small cankerous lesions (very few pixels) may be removed along with the undesired pixel noise during the erosion operation. This can be observed in Figure 5-3, where two very small lesions in the 'Binary image' (image after thresholding) disappeared after the morphological opening operation in the 'Final Binary image'. Hence there is risk of removing small canker lesions when filtering resulting in an increase in false negatives. In Figure 5-4, the algorithm's ability to discriminate between canker and other peel conditions is shown. One should note that the images of individual grapefruits in Figure 5-4 were acquired separately and a mosaic containing seven samples was generated to reveal capability of canker detection. As can be seen in Figure 5-4, the 'Final Binary Image' (after morphological opening) contains white pixels at canker lesions locations, while all other pixels were thresholded to black.

The effect of varying threshold values on classification accuracy was analyzed for threshold values ranging from 1.20 to 1.35 for all two band ratio images. It was observed that the threshold value of 1.20 gave the best canker detection accuracy of 99.05% with the overall accuracy of 89.17%. On the other hand a higher threshold value

of 1.35 did a better job in terms of overall accuracy (93.13%) (but not the best overall accuracy), meanwhile the canker detection accuracy was reduced to 77.62%. The reason behind this was, as we increased the threshold value the smaller canker lesions were eliminated thus increasing the false negative errors. The result of variation of threshold value on classification can be easily observed from the graph in Figure 5-5.

We can conclude from graph that, canker classification accuracy diminishes with increasing threshold value (due to filtering out smallest canker lesions); on the other hand the overall accuracy shows opposite trend, increasing with threshold value. However, after a certain threshold value, the overall accuracy also starts dropping as canker misclassification increases at higher threshold values. The threshold value of 1.275 appears to give best tradeoff between canker classification accuracy (94.3%) and overall classification (95.7%). Table 5-2 summarizes these classification results for the two band ratio method. So, when evaluating lesion detection size limits, one should keep in mind that along with the number of erosion cycles, excessively high values of threshold can also result in increased misclassification and thus poor estimation of the size of the smallest detectable canker lesion.

Binary Lesion Size Estimation Results

After classifying all citrus fruits as either “canker” or “no Canker”, the MATLAB algorithm (using ‘bwareaopen’) was applied to detect the smallest cankerous lesion. Figure 5-6 shows the zoomed images of the same sample as in Figure 5-3, before and after applying the ‘bwareaopen’ function. As can be seen from Figure 5-6, two lesions in the left image have disappeared in the right image due to application of the function ‘bwareaopen’. These two lesions were the smallest lesions detected by our algorithm. One should not get confused between the application of erosion in the opening filter and

the use of MATLAB function 'bwareaopen'. We made use of the morphological opening filter to get rid of unwanted pixels like edges and other minor peel disease conditions, which is a normal filtering approach that would be implemented in the online detection system. On the other hand, the function 'bwareaopen' was simply used as an analysis tool to assist in detecting the smallest cankerous lesion present in the binary image.

Two most important factors which influence the estimation of the smallest canker lesion present are, 1} the number of erosion cycles used in the morphological opening operation and 2} the threshold value used in image classification. The effect of variation of threshold values on the lesion size study is already evident from the classification results (refer Figure 5-5). As we increase the threshold value, small sized and lighter canker lesions were removed from the final binary image resulting in reduced classification accuracy because of increased false negative errors.

The effect of the number of erosion cycles is explained in Table 5-3, which shows a classification summary for 210 cankerous grapefruit samples with a threshold of 1.275 and different number of erosion cycles. As the number of erosion cycles is increased from 1 to 5, our classification results vary from 94.29% to 11.90%, respectively. Also if we look at the size of smallest lesion detected in terms of number of pixels, the size can be seen increasing with the number of erosion cycles. The reason behind this was the small sized and lighter lesions were removed by the increased number of erosion cycles. In this study, a single erosion cycle and a classification threshold of 1.275 has been used to avoid increasing false negative errors of classification.

Results of Mapping Binary Lesion Size to Original Hyperspectral Image

Figure 5-7 portrays the process of mapping the binary canker lesion to the original hyperspectral image. As can be seen, the image at center shows the detected lesion in

binary image. The corresponding original lesion is encircled in the left image. The right most image shows the same lesion being located in the original hyperspectral image and region of interest (ROI) being grown (red in color) using ENVI's ROI tool to calculate the number of pixels in the actual canker lesion in the original hyperspectral image. Each one of the 210 cankerous grapefruit samples was examined and the smallest canker lesion was detected in the corresponding binary images and then mapped back to the original hyperspectral image. The plot in Figure 5-8 shows probability distribution of the actual canker lesion size in pixels.

As can be seen from Figure 5-8, most of the data is concentrated in the lesion size range of 6 to 35 pixels and the plot could be approximated by a 'Log-Normal' distribution. Contrary to the characteristics of a Normal or Gaussian distribution this data set does not exhibit a central tendency and thus has some other probability distribution. However, we can observe that the mode of the dataset corresponds to the lesion size range of 8 to 14 pixels with a frequency of occurrence of 37 out of 210, while 73 out of 210 would fall in the range of 8 to 21. This suggests that when using the optimal number of erosions and threshold, the two-band classification approach is consistently classifying lesions in this size range at above 94% accuracy. Figure 5-9 shows more details of the encircled part of the plot in Figure 5-8.

The size of the smallest canker lesion, in terms of surface area (sq. mm.) was determined utilizing the spatial resolution of each pixel (0.6 mm in both horizontal and vertical directions) as,

$$A = \text{Number of pixels in smallest lesion} \times 0.6 \text{ mm} \times 0.6 \text{ mm} \quad (5-2)$$

Assuming that the canker lesions can be approximated by a circular shape, the equivalent diameter of the smallest lesion can be calculated in mm. The smallest canker lesion detected consisted of 6 pixels. The surface area of corresponding lesion was 2.16 sq. mm. and the corresponding equivalent diameter was 1.66 mm.

One other important point to be noted is that the original resolution of the image has not been used to calculate the size of the smallest lesion. The size of the original 3-D hyperspectral image cube was 1740×400×92 (92 bands) which was reduced to 870×200×92 by image preprocessing to lessen the computation, resulting in reduction of the pixel resolution from 0.3×0.3 sq. mm. to 0.6×0.6 sq. mm. If the original image size, of 1740×400×92 with a pixel resolution of 0.3×0.3 sq. mm, was used then smaller sized canker lesions may be detected, but at the cost of increased computation time and memory usage.

Summary and Conclusion

Although quarantine of canker infected fruit has ended in the US, in several international markets the inspection of canker is still considered crucial for the prevention of the spread of the disease. Detection of this disease is vital to all the citrus growing regions due to its high damage potential, fast spread and enormous impact on the export and domestic trade. Early symptoms of canker can have very small canker specks which are difficult to detect with the human eyes and yet they can end up in the shipment. This research focused on determining the limit for detecting small canker lesions for rapid real time applications. Hyperspectral reflectance imaging was found to be capable of detecting very small citrus canker lesions when utilizing a two band multispectral algorithm developed using correlation analysis. The two wavelengths in the near infrared (NIR) region, 834 nm and 729 nm, are the most suitable wavelengths

to detect cankerous lesions. The ratio of reflectance for these two wavelengths along with a simple thresholding and morphological opening approach forms the basis for canker detection. It was observed that smaller values of thresholds gave better canker classification accuracy (up to 99%), while giving a lower overall accuracy (89%). On the other hand, the trend was opposite for higher threshold values. Also as the numbers of erosion cycles were increased, the classification accuracy dropped drastically, as the small canker lesions were removed by the erosion operation. Therefore, the minimum canker lesion sizes detected at a higher number of erosion cycles were significantly larger than those detected at a fewer number of erosion cycles. The threshold value of 1.275 and a single erosion cycle in the opening filter gave the optimum classification accuracy. The best overall classification accuracy was found to be 95.7%. The statistics of the lesion size showed that the probability distribution is approximately log-normal and hence we cannot use central tendency as a representative of the data. Most minimum lesion size data accumulated in the low pixel range (6-35 pixels in number). The grape fruit samples with canker lesions as small as 6 pixels in size were classified accurately. The corresponding size of the smallest cankerous lesion in terms of surface area was 2.16 sq. mm. and in terms of equivalent diameter was 1.66 mm. The resolution of a pixel used in this study was 0.6×0.6 sq. mm. If we use higher resolution images, we should be able to detect even smaller canker lesions than that detected during this study.

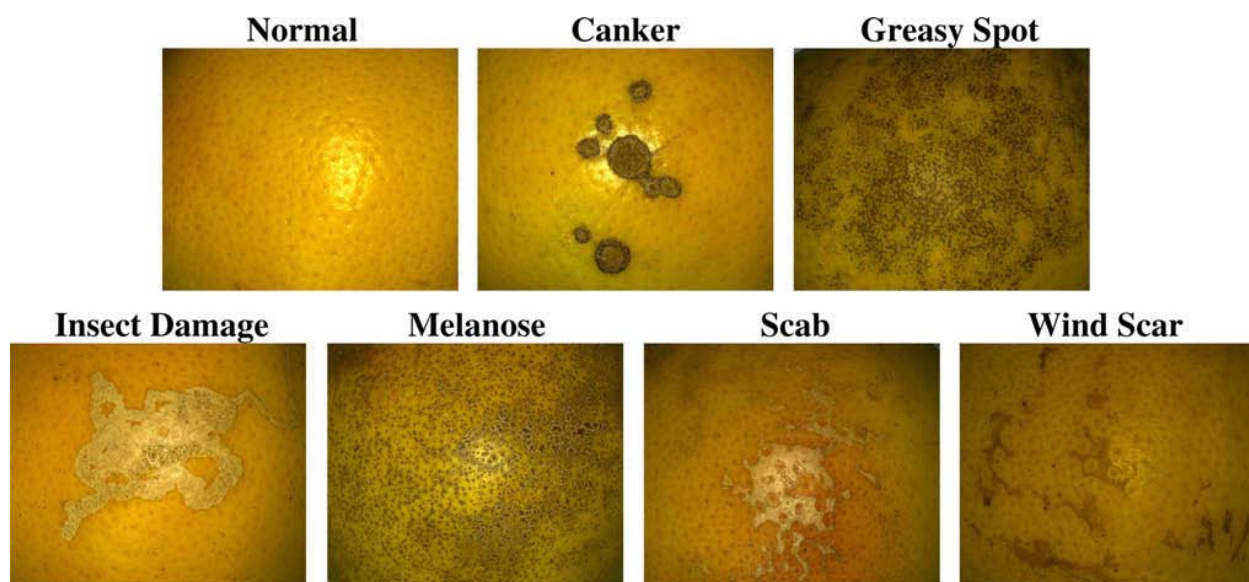


Figure 5-1: Representative normal and diseased peel conditions of grapefruit samples

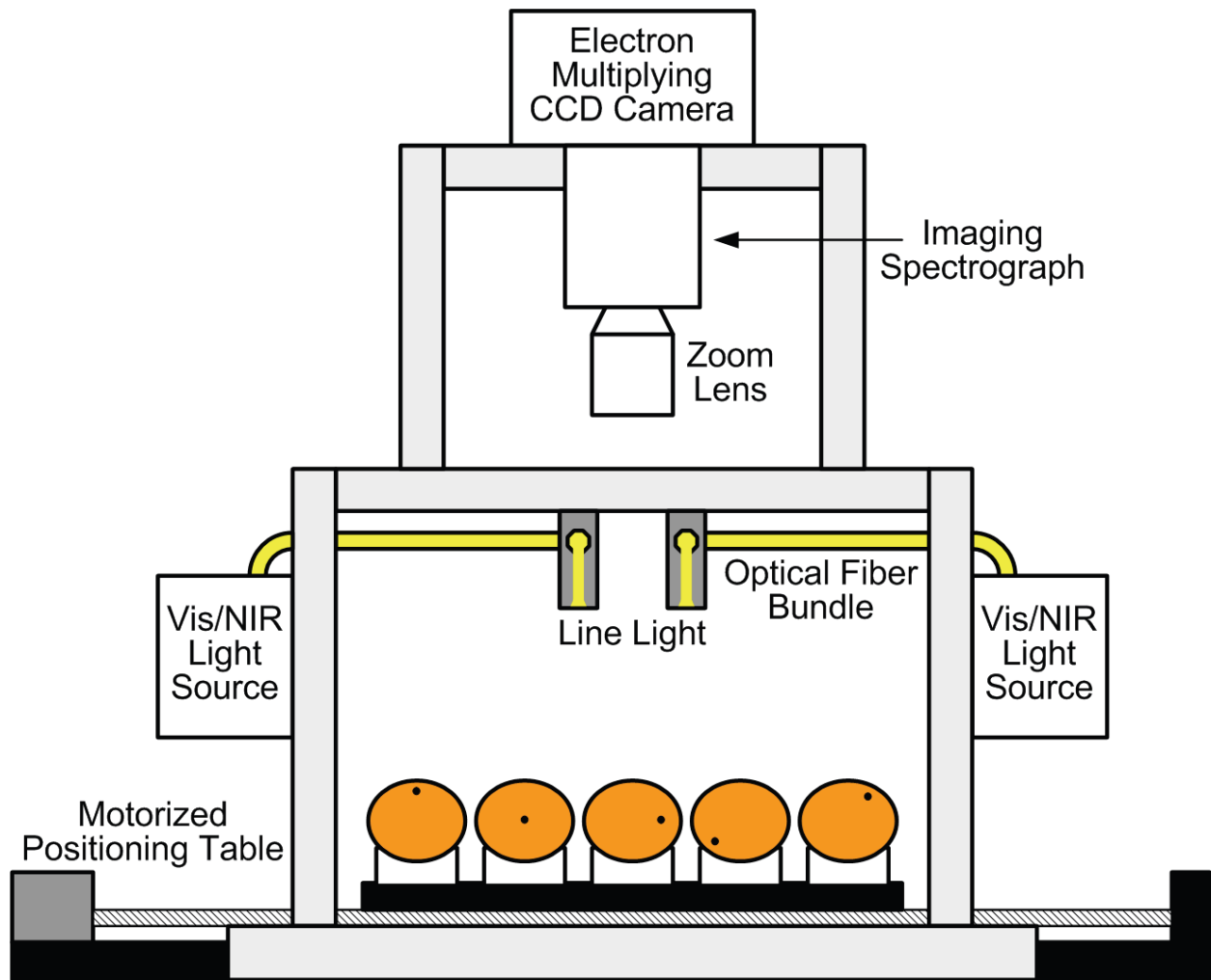


Figure 5-2: Hyperspectral imaging system for reflectance image acquisition from grapefruits

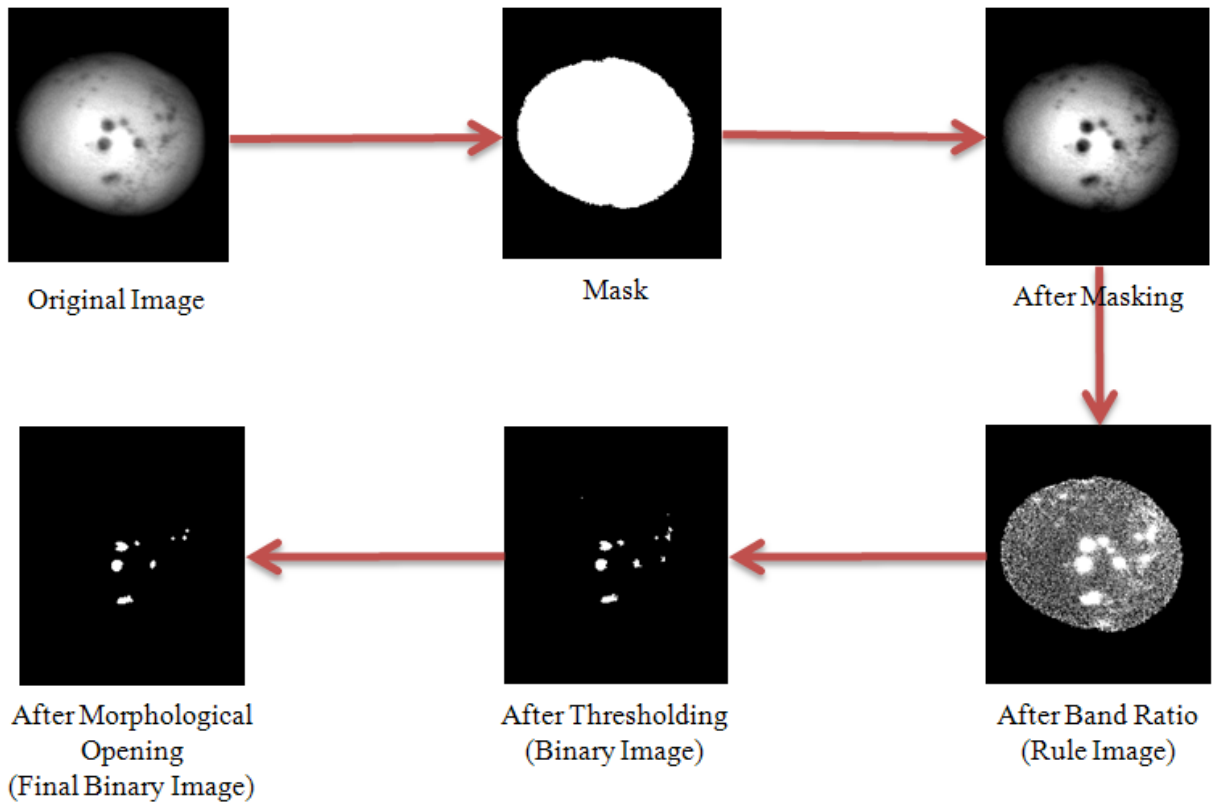


Figure 5-3: Image Classification Procedure

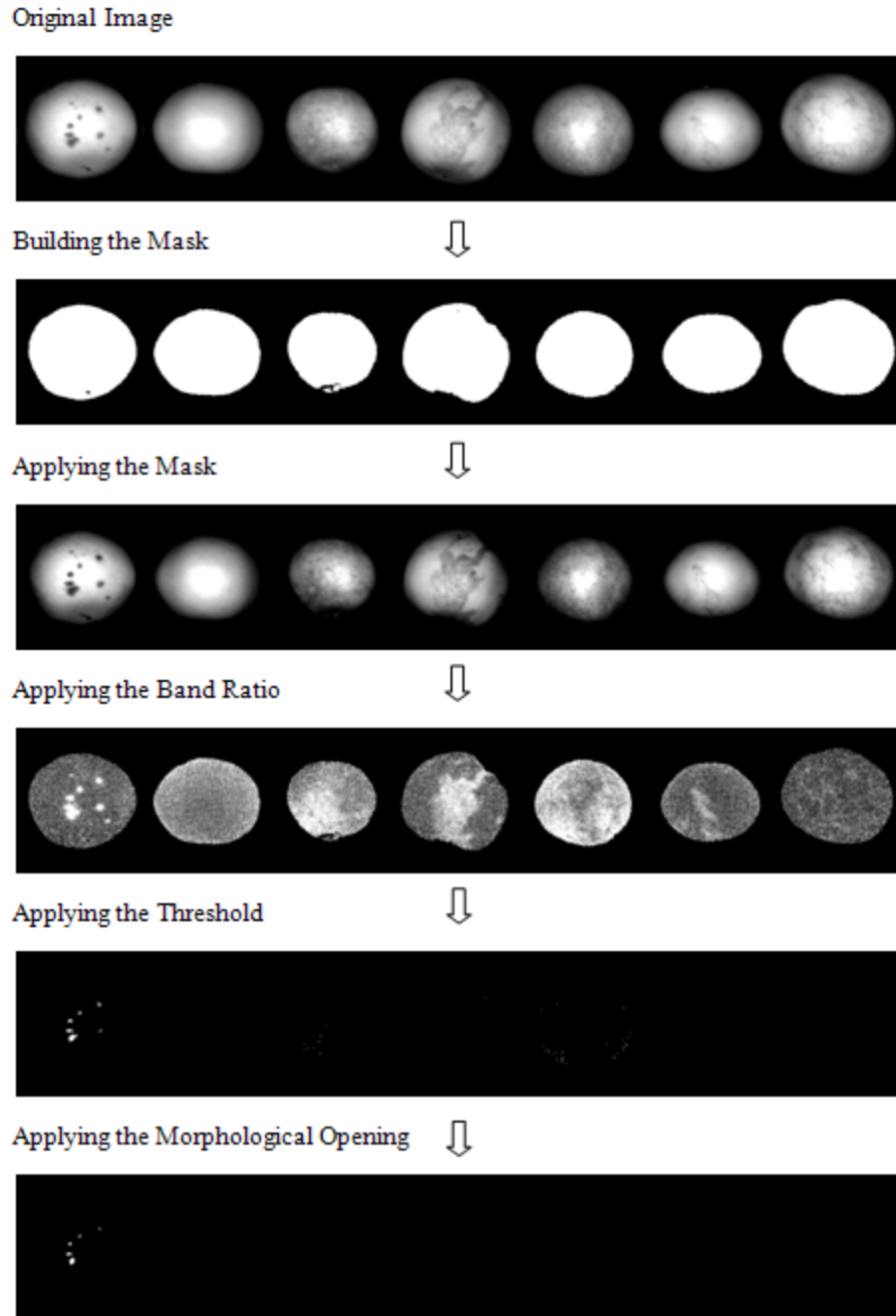


Figure 5-4: Classification Method-Discrimination of canker from other peel conditions

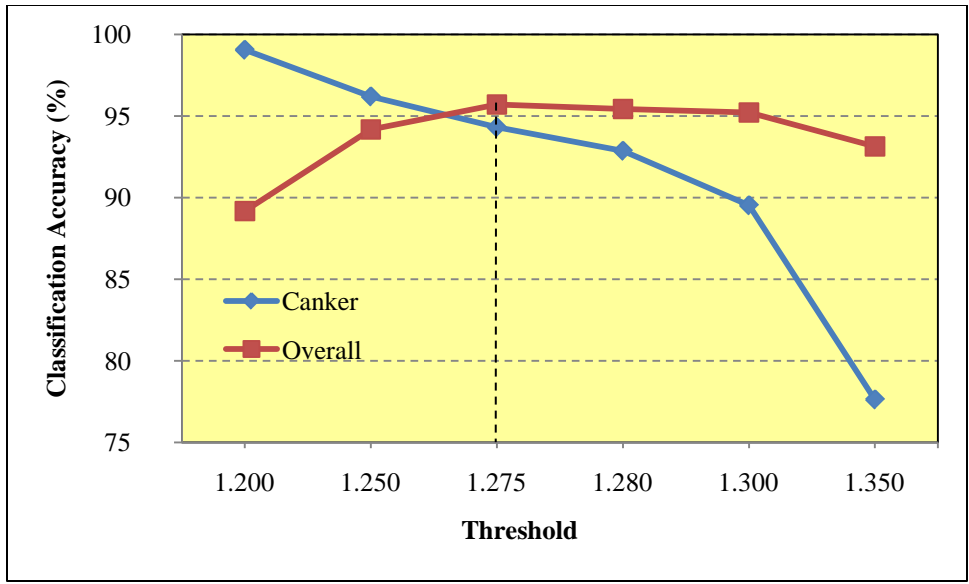


Figure 5-5: Effect of variation of threshold values on classification accuracies

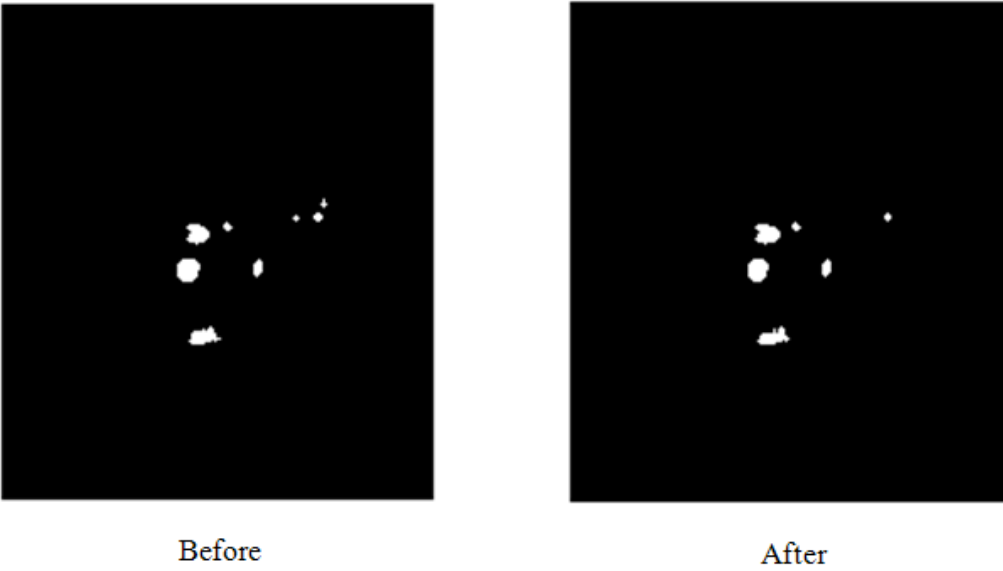


Figure 5-6: Final Binary Image of a sample before and after applying the 'bwareaopen' function

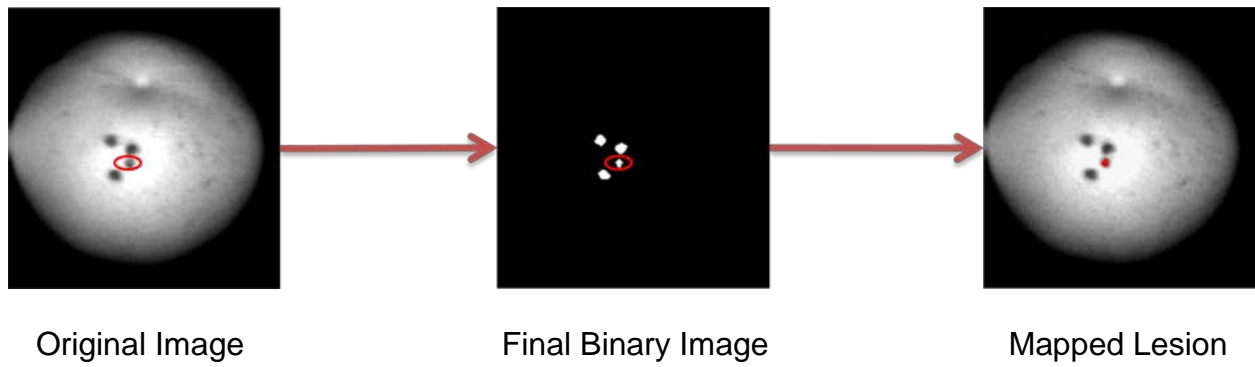


Figure 5-7: Mapping binary lesion size to original hyperspectral image

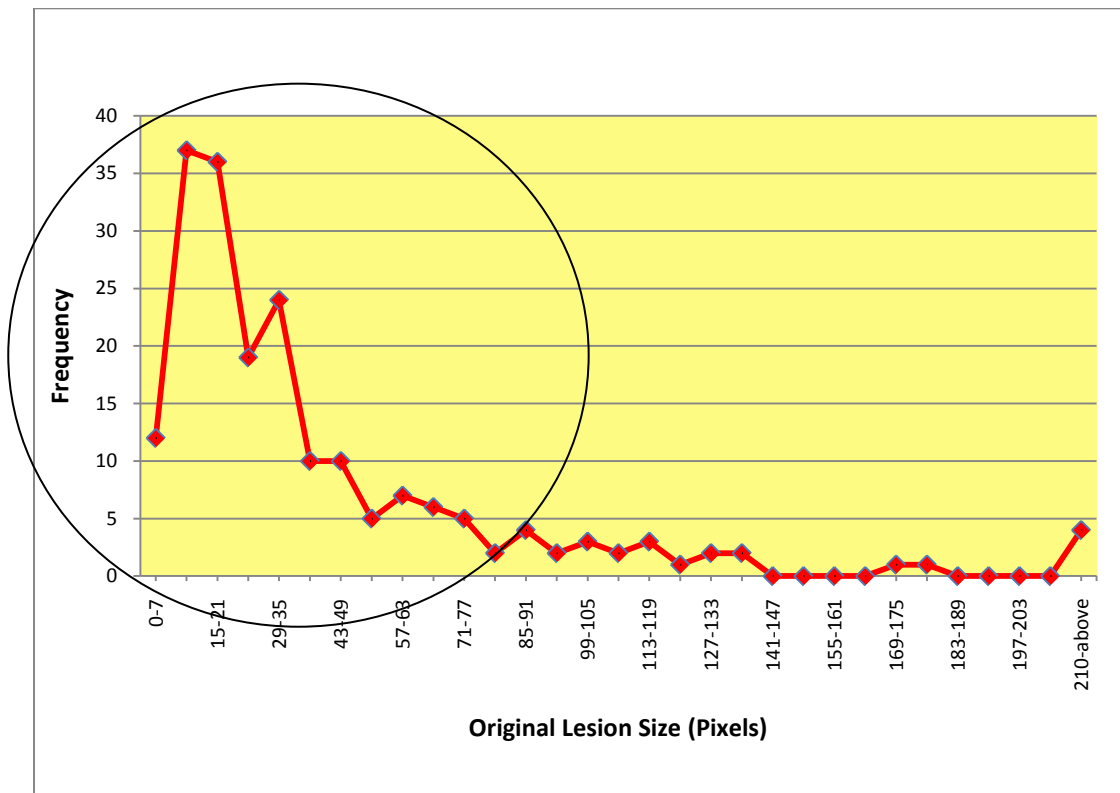


Figure 5-8: Probability distribution of lesion size of all samples

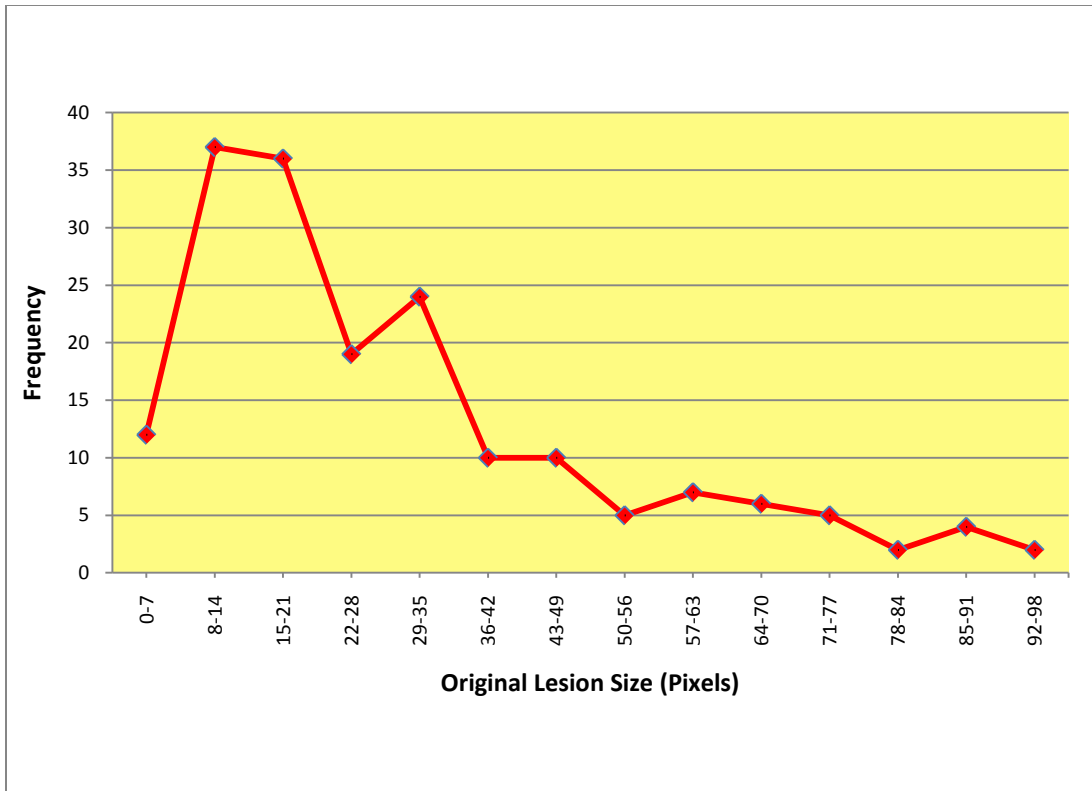


Figure 5-9: Probability distribution of lesion size of subset of all samples

Table 5-1: Numbers of fruit samples for each peel condition

Peel Condition	Canker	Normal	Greasy Spot	Insect Damage	Melanose	Scab	Wind Scar
Number	210	150	120	60	180	180	60

Table 5-2: Summary of classification results

Disease	Number of Samples	Rule Classifier Threshold	Number of Misclassified	Classification accuracy (%)
Canker	210	1.275	12*	94.29
Greasy spot	120	1.275	12	90.00
Insect damage	60	1.275	1	98.33
Melanose	180	1.275	10	94.44
Scab	180	1.275	5	97.22
Wind scar	60	1.275	0	100.00
Market	150	1.275	1	99.33
Overall	960		41	95.73

* Represents the number of misclassified canker samples out of the total of 210 canker infected samples.

Table 5-3: Effect of number of erosion cycles on canker lesion size estimation

Number of Erosion Cycles	Number of Misclassified Samples ¹	Canker Classification Accuracy (%)	No. of Pixels in Smallest Lesion
1	12	94.29	5
2	60	71.43	13
3	109	48.10	25
4	162	22.86	41
5	185	11.90	61

¹ Represents the number of misclassified canker samples out of the total of 210 canker infected samples.

CHAPTER 6 DETECTION OF CITRUS CANKER USING RGB COLOR IMAGE ALONG WITH NEAR-INFRARED MONOCHROME IMAGES

Introduction

Citrus canker is one of the most devastating diseases that the citrus industry is presently fighting with. Citrus canker which is caused by bacterial pathogen *Xanthomonas axonopodis*, is spread almost all over the world. However few areas like South Africa, Australia, the Fiji Islands, Mozambique, and New Zealand have been proven successful for eradicating canker completely. Active ongoing eradication programs still continue in other infected areas such as Argentina, Uruguay, Brazil, and Florida. Due to its fast spread, high damage potential, and massive impact on export and domestic trade, canker is considered as one of the most disturbing diseases that threaten all citrus-growing areas.

Florida which produces more than 70% of citrus supply is the only region in United States which is under the influence of this disease. It is really difficult to eradicate canker completely from all the infected regions and hence the present objective of Citrus Canker Eradication Program (CCEP) is to minimize the level of disease and to prevent the spread of the disease to the unaffected or already eradicated area. The presence of cankerous fruit in a shipment could result in the whole shipment being deemed unmarketable to some 'canker-free' areas, such as the European countries. It is therefore crucial to detect citrus canker and eliminate the infected fruit before they go to the market.

Present human inspection is labor intensive and time consuming. Also it is subjected to the skill level of the labor. So the need of an automated disease detection system gets highlighted. Some machine vision and image processing related

approaches have been used by different researchers to detect defects on the biological items like fruits and leaves which include citrus disease detection using color texture features and discriminant analysis (Pydipati et al., 2006), poultry carcasses defect detection using co-occurrence texture features (Park and Chen, 2000), statistical and neural network classifier for citrus disease detection (Pydipati et al., 2005), classification of different weed species using color co-occurrence method and neural network classifier (Burks et al., 2000), and many more.

In the recent years, hyperspectral and multispectral imaging techniques have been developed as useful tools for quality and safety evaluation of food and agricultural products. The hyperspectral imaging technique acquires spatial information across a sequence of individual band in a broad wavelength range, which generates a 3-D image cube with a high spectral resolution. Although plenty spectral information is fairly useful for laboratory research, the hyperspectral cube contains redundant information across tens or hundreds of bands. Consequently, real-time hyperspectral image acquisition and processing is challenging due to the large amount of data. Hyperspectral band selection, therefore, is usually performed to find a subset containing few significant wavelengths (usually less than ten) with an aim of useful information extraction and image dimensionality reduction. Such attempts using hyperspectral and multispectral imaging include bruises detection on apples using NIR hyperspectral imaging (Lu, 2002), online defect and fecal contamination detection on apples (Kim et al., 2007), multispectral wavelength selection using correlation analysis for detection of defects on apples (Lee et al., 2008), wavelength selection for discriminating weeds from crop (Piron et al., 2007), PCA based image classification for citrus canker detection (Qin et

al., 2008), multispectral wavelength selection for citrus canker detection using correlation analysis (Qin et al., 2009) etc.

The literature also reveals that RGB color images, with or without hyperspectral / multispectral imaging, have been successfully used to detect defects, physical damages and diseases on the biological produce. Stem ends and sooty mold conditions can also be separated from diseases condition using RGB color imaging. Noordam et al. (2005) made use of RGB color images along with multispectral images to detect the latent defects and diseases on raw French fries. Kim et al. (2009) also used high resolution RGB images of citrus fruits and leaves to detect the presence of canker and greening diseases.

Our research team (Qin et al., 2009) has recently developed an algorithm for real time online detection of the cankerous fruits using two monochrome camera assemblies. The two wavelengths of the cameras were selected by applying the correlation analysis to the 3-D hyperspectral image cube. However, it is needless to mention that a single 3-CCD camera is definitely cheaper than multiple monochrome cameras required for capturing the independent single band multispectral images or electron multiplying charge-coupled-device (EMCCD) camera assemblies required for acquiring hyperspectral images. So this particular exploration was aimed at investigating if one of the monochrome cameras can be replaced by a CCD camera so that RGB color image can be used in conjunction with a monochrome image to detect cankerous citrus fruit. This novel two camera system (with one CCD color camera and other monochrome camera) then would allow us to exploit the RGB color image for other detection tasks like sooty mold detection, physical damage detection etc. as well.

As this was an experimental attempt, instead of purchasing a CCD camera to capture RGB images, the RGB color images of the fruits were simulated using previously captured hyperspectral images (450 – 700 nm). The final image, which was further processed for diseases detection, would then be created by combining the RGB color image and the selected single wavelength image from the hyperspectral data which were not considered while creating the RGB image (700 – 930 nm).

Materials and Methods

Citrus Samples

Ruby Red grapefruits with normal surface, canker, and five common diseased peel conditions (i.e., greasy spot, insect damage, melanose, scab, and wind scar) were tested in this study. Color images for each typical peel condition are shown in Figure 6-1. The diseases on the fruit surface show different symptoms. Greasy spot, melanose, and scab are all caused by fungi, which generate surface blemishes that are formed by infection of immature fruit during the growing season. Greasy spot produces small necrotic specks, and the affected areas are colored in brown to black and exhibit greasy in appearance. Melanose is characterized by scattered raised pustules with dark brown to black in color. Scab appears as corky raised lesions usually with the color of light brown. Different from the fungal diseases, citrus canker is caused by bacteria, and it is featured with conspicuous dark lesions. Most circular in shape, canker lesions vary in size and they are superficial (up to 1 mm deep) on the fruit peel (Timmer et al., 2000). Diameter of the canker lesions tested in this study was approximately in the range of 1-9 mm. Insect damage is characterized by irregular grayish tracks on the fruit surface, which are generated by larvae of leafminers that burrow under the epidermis of the fruit

rind. Wind scar, which is caused by leaves, twigs, or thorns rubbing against the fruit, is a common physical injury on the fruit peel, and the scar tissue is generally gray.

Fruit samples were handpicked monthly from a grapefruit grove in Fort Pierce, Florida during a seven-month harvest period from October 2007 to April 2008. Thirty samples for each peel condition were collected for each month if the condition was available. Cankerosus samples were collected all seven months, and the samples with other peel conditions were not obtained every month due to their availabilities. The grapefruit samples with different sizes of canker lesions were used to evaluate the size detection limits for hyperspectral image processing and classification methods.

A total of 960 grapefruits were collected and tested in this study. Numbers of samples for each peel condition are summarized in Table 6-1. All the grapefruits were washed and treated with chlorine and sodium o-phenylphenate (SOPP) at the Indian River Research and Education Center of University of Florida (UF) in Fort Pierce, Florida. The samples were transported to UF campus in Gainesville, Florida, and stored in an environmental control chamber maintained at 4 °C. The samples were removed from cold storage about 2 hours before imaging to allow them to reach room temperature. During image acquisition, the fruit samples were placed on the rubber cups, which were fixed on the positioning table of the imaging system, to make sure the diseased areas were on the top of each fruit.

Hyperspectral Imaging System

A hyperspectral imaging system was used to acquire reflectance images from citrus samples. Schematic diagram of the system is illustrated in Figure 6-2. It is a push broom, line-scan based imaging system that utilizes an electron multiplying charge-coupled-device (EMCCD) camera (iXon, Andor Technology Inc., South Windsor, CT,

USA). The EMCCD has 1004×1002 pixels and is thermoelectrically cooled to -80°C through a double-stage Peltier device. An imaging spectrograph (ImSpector V10E, Spectral Imaging Ltd., Oulu, Finland) and a C-mount zoom lens (Rainbow CCTV H6X8, International Space Optics, S.A., Irvine, CA, USA) are mounted to the camera. The instantaneous field of view (IFOV) is limited to a thin line by the spectrograph aperture slit (30 μm), and the spectral resolution of the imaging spectrograph is 2.8 nm. Through the slit, light from the scanned IFOV line is dispersed by a prism-grating-prism device and projected onto the EMCCD. Therefore, for each line-scan, a two-dimensional (spatial and spectral) image is created with the spatial dimension along the horizontal axis and the spectral dimension along the vertical axis of the EMCCD. The lighting unit consists of two 21 V, 150 W halogen lamps powered with a DC voltage regulated power supply (TechniQuip, Danville, CA, USA). The light is transmitted through optical fiber bundles toward line light distributors. Two line lights are arranged to illuminate the IFOV. A programmable, motorized positioning table (BiSlide-MN10, Velmex Inc., Bloomfield, NY, USA) moves citrus samples (five for each run) transversely through the line of the IFOV. One thousand seven hundred and forty line scans were performed for five fruit samples, and 400 pixels covering the scene of the fruit at each scan were saved, generating a 3-D hyperspectral image cube with the spatial dimension of 1740×400 for each band. Spectral calibration of the system was performed using an Hg-Ne spectral calibration lamp (Oriel Instruments, Stratford, CT, USA). Because of inefficiencies of the system at certain wavelength regions (e.g., low light output in the visible region less than 450 nm, and low quantum efficiency of the EMCCD in the NIR region beyond 930 nm), only the wavelength range between 450 and 930 nm (totaling 92 bands with a

spectral resolution of 5.2 nm) was used in this investigation. The parameterization and data-transfer interface software for the hyperspectral imaging system were developed using a SDK (Software Development Kit) provided by the camera manufacturer on a Microsoft Visual Basic (Version 6.0) platform in the Windows operating system.

Image Pre-Processing

As mentioned in the earlier section (Hyperspectral Imaging System), each hyperspectral image taken with our system consists of 3-D hyperspectral image cube with spatial dimension of 1740×400 and spectral dimension of 92 (92 wavelengths). To reduce the amount of data for computation, the binning technique was used in which the hyperspectral image data was averaged by two neighboring pixels in both vertical and horizontal spatial dimensions at each wavelength. This reduced the size of the original 3-D image data from 1740×400×92 (92 bands) to 870×200×92, and resulted in a spatial resolution of 0.6 mm/pixel for both vertical and horizontal dimensions. The image preprocessing procedures described above were executed using programs developed in MATLAB R2007a (Math Works, Natick, MA, USA). Along with this the image preprocessing was performed for the original hyperspectral reflectance images to fulfill flat- field correction and image masking which resulted in normalized and masked hyperspectral cubes with a dimension of 870×200×92 (92 bands). Detailed procedures for hyperspectral image preprocessing can be found in Qin et al. (2008).

Simulation of RGB Color Image

When white light falls on the 3-CCD camera lens, the lens amplifies the incoming signal (light) and this signal is filtered through the Red, Green and Blue filters' assembly so that only red / green / blue light is directed to the respective CCD chips. The CCD chips generate the signals proportional to the light falling on them which when

processed by camera electronics, the red, green and blue channels of the digital image are created (The Imaging source, 2005). The similar principle was employed while simulating the red, green and blue channels for this study. The filter characteristics were simulated and the resulting filter was applied to previously captured hyperspectral images to generate the red, green and blue response of the image.

First of all, the transmission characteristics of the red, green and blue filters were assumed to have a Gaussian bell shape in the wavelength range of 600-700 nm, 500-600 nm and 400-500 nm, respectively with corresponding means at 650, 550 and 450 nm (Kondo and Ting, 1998). These filter characteristics were then simulated using MATLAB R2009a and are presented in Figure 6-3. These filters were then applied to the monochrome images of respective wavelength ranges from the 3-D hyperspectral image cube. The filter characteristics gave a particular value of transmittance for every wavelength in the respective red, green and blue range. The monochrome image of a particular wavelength was then multiplied by the corresponding transmittance value. The monochrome images in the range 600-700 nm, 500-600 nm and 400-500 nm processed in this way were combined together (taking average of all the monochrome images in a particular channel) to generate the red, green and blue channels of the RGB image.

Combining RGB Color Image and Remaining Monochrome Images

As mentioned earlier the hyperspectral images were captured in the range of 450 to 930 nm. The simulated RGB image had considered the wavelengths in the range of 450 to 700 nm. So the remaining wavelengths (700-930 nm) were combined with the simulated red, green and blue channels so as to create a new hyperspectral image. This new hyperspectral RGB + NIR simulated image had 46 bands or channels, the first

three of them were red, green and blue while the remaining 43 were the single band images at respective wavelengths in the range 700 to 930 nm. So this hyperspectral image of size 870×200×46 (46 bands) was used for further analysis.

Hyperspectral Band Selection

After simulating the RGB color image and combining it with the single band images as explained in previous section, the resulting hyperspectral image was of size 870×200×46 (46 bands). Even if this image was of size smaller than the previous one (870×200×92), this size was still too large from computation point of view. Hence to obtain computationally viable approach, previously developed multispectral algorithm (Qin et al., 2009) was used to select optimal wavelengths by applying correlation analysis to hyperspectral image cube of size 870×200×46. The main objective was to observe if the correlation analysis picks any of the red, green or blue channels along with some NIR wavelength for identifying canker.

The correlation analysis (CA) helps to select an optimal pair of wavelengths which can be used to segregate the cankered citrus fruits from normal or other peel conditions. First of all the reflectance spectra of canker, normal and five other disease conditions (greasy spot, insect damage, melanose, scab and wind scar) were extracted using ENVI 4.3 software (ITT Visual Information Solutions, Boulder, CO, USA). Instead of extracting the reflectance spectra from a single pixel of respective peel condition, it was acquired by averaging over number of pixels by using the region of interest (ROI) tool in ENVI. The ROI was manually selected in the zoom window that contains typical diseased or normal peel areas using various drawing methods (e.g., polygon, rectangle, ellipse, point, grow, and merge) offered by ENVI ROI tools. Enough care was taken to preserve the purity of each of the ROIs in a sense that the whole ROI contained pixels

from only one desired peel condition while edge and other undesired pixels were excluded. As this study was conducted on the experimental basis; only 70 samples, 10 each of the seven peel conditions (canker, greasy spot, insect damage, melanose, scab, wind scar and normal) were selected at random from the total of 960 samples for the exploration. All the 70 grape fruit samples were used for the ROI selections, and at least one ROI was selected from the representative region for each fruit. The mean reflectance spectrum for each fruit was then computed from merged ROIs within each fruit, which was then used as individual reflectance spectrum for the wavelength selection.

In this investigation the optimal pair of wavelengths selected by correlation analysis was used to create the two band ratio image (i.e., $R_{\lambda 1}/R_{\lambda 2}$, where $R_{\lambda n}$ denotes single band reflectance image at the wavelength of λn) which helped us to make the distinction. Ratio method was chosen because the ratio images are invariant to illumination scaling, which is a significant advantage for real-time applications. All the 70 fruit samples were divided into two classes: 'Canker' class including 10 samples with canker lesions, and 'No Canker' class including 10 normal samples and 50 samples with other five peel diseases. To facilitate the correlation analysis, samples in the 'Canker' class were labeled with '1', and 'No Canker' class with '0'. Then two vectors were generated, one of them was the vector containing ratio of reflectance at respective wavelengths for every sample (size = 1 × number of samples) and other was the vector containing all the label values (i.e., 1 and 0) (size = 1 × number of samples). Also it should be noted that there was one vector of ratio of reflectance for each band combination. Correlation coefficients were then calculated comprehensively for every

possible two band combination (from 46 bands), between these two vectors i.e., the vector of ratio of reflectance between corresponding band combination and the vector of label values. The pair of bands which gave the maximum value for the correlation coefficient (which is nothing but the optimum pair mentioned earlier) was selected for further classification study. The ratio of reflectance of the two bands 771 nm and 739 nm (R_{771}/R_{739}) is found to give the maximum absolute value for the correlation coefficient of 0.8284 and hence was chosen to be the optimal pair of wavelengths to discriminate between cankered and other peel conditions. The detailed procedure for selecting the optimal pair of wavelengths can be found in Qin et al. (2009).

Image Classification

After important wavelengths were identified, band ratio images were computed using ENVI 4.3 software (ITT Visual Information Solutions, Boulder, CO, USA) based on the wavelengths, selected using correlation analysis. The equation $R_{\lambda_1}/R_{\lambda_2}$ (i.e., R_{771}/R_{739}) was used to calculate these ratio images. A simple thresholding approach, which has been used to separate the cancerous fruits from six other peel conditions (normal peel and other citrus diseases), was applied to the ratio images calculated using the above equations. Different threshold values were used to evaluate the classification accuracies for canker identification. Morphological filtering succeeded thresholding in order to remove undesired small size pixels (e.g., edges and peel diseases other than canker) from the image as these small pixels can confuse the algorithm of lesion size detection. The morphological “opening” operation was applied to the thresholded image, which by definition means erosion of the image followed by subsequent dilation, for this purpose. The opening filter from the ENVI morphological filter tools with a kernel size of 3×3 was selected. The purpose of erosion is to remove

the undesired small size pixels with dilation smoothing out the contours of the remaining pixel areas to help restore the round feature of the canker lesions in the final binary images.

Results, Observations and Discussion

Key Wavelengths for Canker Detection

The contour plot of the correlation coefficients (r) between two band ratios (i.e., $R_{\lambda_1}/R_{\lambda_2}$) and fruit peel conditions is shown in Figure 6-4. As can be seen there are three regions which display relatively high values for correlation coefficients in the upper triangle of the plot. The largest region has horizontal spectral range of 718 to 750 nm and vertical spectral range of 857 to 943 nm. The smallest region has horizontal spectral range of 725 to 739 nm and vertical spectral range of 848 to 852 nm. The region of moderate size has horizontal and vertical spectral ranges of 731 to 750 nm and 760 to 783 nm, respectively. This moderate size region was of most interest as the maximum correlation coefficient was found in this region. The two band ratio between the wavelengths 771 nm and 739 nm (R_{771}/R_{739}) gave the maximum absolute correlation value of 0.8284, which points out the potential for canker detection. The point to be noted here is both the wavelengths are in near infrared (NIR) region of the electromagnetic spectrum. That is, the red, green or blue bands of the mosaicked hyperspectral image, neither alone nor together (with any of the red, green or blue channels or any other wavelengths) illustrated the capacity to detect canker.

Figure 6-5 shows the reflectance spectra of the grapefruit samples with different peel conditions including canker, greasy spot, insect damage, melanose, scab, wind scar and normal, over the spectral region of 450 to 930 nm. Out of this spectral region, 450 to 700 nm was considered in the red, green and blue channels, while the remaining

was covered by the monochrome images in the range 700 to 930 nm. In order to obtain the spectrum for each peel condition, all the ROI spectra (from all the samples) for one peel condition were averaged together and plotted. As can be seen, all the peel conditions consistently portrayed lower reflectance than that of the normal peel over the entire spectral range, except in the red, green and blue channels where all the spectra were seem to be overlapping each other. Melanose had the lowest reflectance throughout the range except between 724 to 750 nm where reflectance of canker was lower.

In Figure 6-5, the dotted lines indicate the important wavelengths (i.e., 739 nm and 771 nm) for canker identification selected by correlation analysis. As can be observed the rate of change of reflectance of canker was higher than any other peel condition within the two wavelengths selected. In other words reflectance of canker within these two wavelengths showed remarkable increase towards longer wavelength than any other peel condition which indicated that canker has larger spectral slope in the spectral range of 739 nm to 771 nm than any other fruit surface condition. This unique distinctive spectral feature of canker in this spectral range could be the reason why the band ratio of these two wavelengths can highlight canker. The previously mentioned point, that none of the red, green or blue channels are useful for canker discrimination, is also in line with what we can see from the mean spectra of different peel conditions as displayed in Figure 6-5. In the red, green and blue channels the spectra of all the conditions overlap, and hence it is really difficult to separate the fruits with different diseases in this region.

Ratio Images

The Figure 6-6 shows the two band ratio images for all the disease conditions. As can be seen, none of the diseases except canker appeared brighter than the normal fruit surface. This distinctive brightness of canker lesions was the result of their higher ratio values. On the other hand the normal fruit peel emerged to be darker than canker because of their small ratio values using the optimal pair of wavelengths (771 nm and 739 nm) selected by correlation analysis. This peculiar brightness of canker lesions could be the result of its higher spectral slope within the selected wavelengths.

Image Classification Results

The image classification procedure explained in the Materials and Methods section is demonstrated in Figure 6-7. The image contains one fruit each from the seven representative peel classes. Images of all the individual fruits were generated separately by combining the simulated RGB image and the monochrome images from the independently acquired hyperspectral images. All the images of different peel conditions were then mosaicked together to create the image of seven fruits. Figure 6-7 not only portrays the classification procedure but also it highlights the capability of the two selected wavelengths to discriminate canker from other peel conditions. The ratio images were calculated using the optimal wavelengths, 771 nm and 739 nm. As can be seen all the diseased regions of the fruit peel, including canker, greasy spot, insect damage, melanose, scab and wind scar, appeared brighter than sound peel of the fruits in the ratio image. This is a result of relatively higher ratio values of the diseases than the normal peel. After the thresholding had been applied to the ratio images most of the fruit peel background as well as other diseases disappeared in the binary image except for canker. The unwanted small size pixels such as edges and remains of other

diseases were then removed efficiently using the morphological opening operation. However, care must be taken while applying the morphological opening filter as the erosion operation in the filter might wipe out the light and small size canker lesions (like the one in top central region of first fruit) and increase the false negative error rate. As a result of the above image post-processing, all the fruit surfaces including diseases other than canker turned dark leaving canker lesions as bright spots which can easily be identified by any computer vision system for online as well as offline applications. Another important point noted during the classification is, none of the 70 fruits' stem ends were misclassified as disease. So it can be concluded that the selected pair of wavelength can successfully discriminate between stem ends and diseases.

It was found that when the reflectance values of all the 70 citrus fruits at the two selected wavelengths, 771 nm and 739 nm, were plotted separately, it formed a cluster with no specific demarcation between different peel conditions. On the other hand when the ratio values of the fruits were plotted, it portrayed quite apparent separation between canker and all the rest peel conditions which can be viewed from Figure 6-8. Figure 6-8 displays the two band ratio values (R_{771}/R_{739}) for all the 70 grapefruits. The vertical dotted lines in the figure divide the data points into seven groups according to peel conditions. As can be seen all the canker ratios have higher values than ratios of other skin conditions which was the result of higher spectral slope of canker within the region between the selected wavelengths. Hence the simple and reasonable approach of thresholding based on the two band ratio values using the wavelengths selected by correlation analysis turned out to be successful for canker discrimination. The horizontal dotted line represents the threshold (value = 1.14) which separates the cankerous

grapefruits from rest of the peel conditions of the grapefruits. The above discussion is enough to prove that it is not practical to inspect citrus canker based on single band reflectance measurement and the spectral information of at least two bands must be used to achieve the goal.

For completeness, the study of effect of threshold values on the canker classification is also included here. Figure 6.9 shows this effect of variation of threshold values on the classification accuracies. One of the two plotted curves represents the variation of canker classification accuracy while the other represents the variation of overall classification accuracy with the threshold values. Four threshold values in the range 1.12 to 1.15 were utilized to evaluate this effect based on the two band ratio images R_{771}/R_{739} . As can be seen, the threshold value of 1.12 gave the best canker classification accuracy of 100.00%, while the corresponding overall classification accuracy was 88.57%. On the other hand, the threshold value of 1.15 achieved the overall classification accuracy of 91.43% (not the best overall classification accuracy though) and canker classification accuracy of 70.00%. As we increase the threshold value the light and small size canker lesion were wiped out increasing the false negative errors, resulting in lower canker classification rate. So after observing the trend of the curves, it was concluded that the canker classification accuracy gets worse with increase in the threshold value while that of overall classification gets better. However after a particular value of threshold, the overall classification accuracy also starts to drop as the canker classification accuracy falls at higher rate (at higher threshold values). The threshold value of 1.14 demonstrated the best tradeoff between the canker and overall classification accuracies. This threshold of 1.14 can also be viewed as a

horizontal dotted line in Figure 6-8 which separates the cankerous fruits from non-cankeraus fruits. It could achieve the canker classification accuracy of 90.00% and overall classification accuracy of 92.86%. The detailed results of classification of the 70 grapefruits corresponding to this threshold of 1.14 are shown in Table 6-1. As can be seen all the market, scab and wind scar samples were classified accurately. The greasy spot and melanose samples were classified with accuracy of 90.00% and 70.00% respectively due to their higher ratio values. As already mentioned in the lesion size estimation study (Chapter 5), greasy spot and melanose might have similar reflectance characteristics as that of canker. This could be the reason behind the low classification accuracies of greasy spot and melanose. And hence the degree of these two diseases was one of the controlling factors for the threshold value. Also it should be noted that as this was just an experimental study, only 70 fruits were examined. Our research group is confident to achieve better classification results if all the 960 samples were considered for the study and the threshold was adjusted accordingly. However, the goal of this study was to verify whether the red, green and / or blue channels of the image along with some other single band monochrome image can be used to identify canker on citrus fruits not to achieve best classification. Hence rests of the samples were not tested for the disease condition during this particular study.

Why RGB Image Can't Be Used for Canker Identification?

As mentioned earlier the objective of the study was to evaluate if the RGB color image can be used with some single band monochrome image to identify canker on the citrus fruits. The reason behind this was the CCD color cameras have typically been used for detecting several other characteristics such as size, color, ripeness of the fruits (based on color) and blemish sizes etc on the agricultural produce. Also utilizing a CCD

color camera instead of a monochrome camera would prove to be less expensive because of their costs as well as if CCD camera is used we do not have to invest in the beam splitter, filters, front and rear lenses and other components necessary for the monochrome cameras. So if we could show that RGB color image, in conjunction with another single band image, can be used for canker identification then one of the single band monochrome cameras in the present two camera system can be replaced with simple CCD color camera to save some capital cost.

The hyperspectral reflectance images were used for this as well as lesion size estimation study. The reflectance of the object at a particular wavelength under consideration was the deciding factor in both the studies. The reflectance values vary with changes in the surface condition of the fruit like disease or defects on the surface. In this particular study, these reflectance properties of citrus fruits were exploited for discriminating citrus canker from other peel conditions. Such reflectance values of all the seven types of peel conditions at different wavelengths i.e., reflectance spectra were plotted in Figure 6-5. As can be seen from this figure, in the range from 708 to approximately 780 nm, canker spectrum is separated from rest of the peel conditions except melanose. So even if we find some band / channel to discriminate canker from other peel conditions based on single band reflectance image, it is very likely that the classification algorithm will get confused and misclassify melanose as canker because of the similar reflectance properties of the two diseases in this spectral range. Also if we observe the rest of the spectral range from 780 nm to 930 nm, reflectance of canker falls between that of the normal peel and the peel with melanose. However, the reflectance of rest of the skin conditions is very similar to that of canker in this range. So

again canker cannot be separated from greasy spot, insect damage, scab and wind scar in this range based on the single band reflectance property. So in summary, single band reflectance images cannot be used for separating canker from other peel conditions and we need at least two or more channels for this task. So with the help of correlation analysis we selected the two wavelengths in NIR region, 771 nm and 739 nm. The ratio of reflectance at these two wavelengths i.e., R_{771}/R_{739} , can discriminate canker from other peel conditions.

The mechanism behind the successful working of the ratio method is the spectral slope of canker between the two selected wavelengths. It can be seen from the reflectance spectra of all the skin conditions in Figure 6-5, that the spectral slope of canker is higher than rest all conditions, between the selected two wavelengths. Hence the ratio of reflectance of canker at these two wavelengths, R_{771}/R_{739} , resulted in the value which was higher than that of any other peel condition. And hence when a threshold was applied to such ratio images, canker was easily being separated from other peels. Now if we observe the reflectance of all the peel conditions in the R, G and B channel range, it can be seen that spectra of all the conditions overlap. And hence all the surface conditions have similar spectral slope in this range. So neither single channel out of R, G, or B channels nor any combination of these channels could be used for canker discrimination.

Another reason why none of the red, green or blue channels could be useful for canker discrimination lies in one of the basic assumptions of correlation analysis. Correlation analysis assumes that the bandwidth of the single band images considered for analysis is very narrow. In the study previously conducted by our research team (Qin

et al., 2009) the bandwidth of each of the single band image was 10 nm. Correlation analysis selects such few bands with the narrow bandwidth having a very specific spectral signature which could be useful identifying the particular surface defect, skin condition or disease. On the other hand each of the red, green and blue channels was created by combining such narrow bandwidth bands. Each of the red, green and blue channels had the bandwidth of 100 nm. Because of these higher bandwidths these R, G and B channels contains more spectral information than the other narrow bandwidth monochrome images. Usually it's always better to have more information in order to better classify the objects however in this particular case this turned out to be a detriment. Because of the wide bandwidth, even if the R, G and B channels contain some information that could help identifying canker, they also might contain the information that would highlight some other surface conditions. And hence none of the R, G and B channels could separate canker from other diseased peel conditions even if they could identify that the fruit peel is not sound. If we observe the reflectance spectra in Figure 6-5, all the fruit peel conditions having similar reflectance in the region covered by R, G and B channels, second the fact that the algorithm might recognize the presence of disease on the fruit surface in that region but it may not be able to discriminate between the different diseases.

Along with the correlation analysis, principle component analysis (PCA) was also conducted on the RGB + NIR simulated image just to check if we get any principle component that would be able to discriminate between canker and other peel conditions. From such principle component it would have been possible to identify any important wavelengths / channels to segregate canker. The algorithm to carry out PCA

was coded in MATLAB R2009a. It was observed that either the second or third principle component was able to identify the presence of some diseases on the fruit peel but both of them were failing to discriminate between canker, greasy spot and melanose. The reason behind this could be the similar reflectance properties of the three diseases. Also the pattern demonstrated by canker was inconsistent, the canker lesions were either appearing as white spots on dark background or dark spots on white background. One interesting observation however was the canker lesions appeared just opposite in second and third principle components for few tested samples. If canker was highlighted as white on black background in second principle component, it appeared black on white background in third principle component. So in the modified algorithm the second and third components were multiplied together to create a new image in which the canker lesions appeared darker than the unaffected peel of fruit. This approach of multiplying the two principle component was used by Lu (2002) during his studies for detecting the bruises on apples. However, this modified algorithm also could not differentiate between canker, greasy spot and melanose. So it was concluded after conducting the tests on few more samples that principle component analysis was incapable of discriminating canker from other peel conditions using this thresholding approach.

Also when the principle component analysis was conducted on the RGB + NIR simulated image, it was observed that most of the times the algorithm was recognizing the presence of disease on the fruit skin but it was not able to discriminate between different diseases which also backs the conclusion that because of the wider bandwidths of the red, green and blue channels, they might be containing information

which not only highlights canker but also other skin defects and hence confusing the algorithm. So finally it can be stated that the RGB color image (along with some single band monochrome image) cannot be utilized to discriminate canker from other peel conditions based on simple thresholding technique. Nevertheless it should be noted that even if this threshold based approach is incompetent of segregating canker, it does not rule out the possibility of RGB color image (along with the selected NIR bands) being helpful in discriminating canker based on some other approach like the one which is feature based or texture based.

Summary and Conclusion

One of the most challenging issues Florida citrus industry is facing is Canker. Due to the fast spread and very high damage potential, the detection of this disease is given utmost priority. Lots of researchers have been investigating different techniques to segregate cankerous citrus fruits from other types of diseases which not only include hyperspectral and multispectral imaging approaches but also simple RGB color imaging practices. This particular study was an attempt to aggregate the merits of both hyperspectral imaging and RGB color imaging. The aim of the study was to investigate whether red, green and/or blue channels of the RGB color image along with some NIR wavelength are capable of identifying canker and discriminating it from other peel diseases. The RGB color image was simulated from the monochrome images in the visible range (450 to 700 nm) from the previously captured hyperspectral image cube. This RGB color image was then combined with the rest of the monochrome images from the hyperspectral image cube (700 to 930 nm) to generate the new input hyperspectral image (870×200×46 bands) for this study. The correlation analysis was then carried out on this new hyperspectral image to identify the key channels with the

intension to check if any of the R, G or B channels is getting recognized as an important channel for canker identification. The correlation analysis chose 771 nm and 739 nm as the important wavelengths. None of the red, green or blue channels were found to be useful for canker identification probably because of their high bandwidths (100 nm). Because of the higher bandwidths; they contained more spectral information than other single band images. This fact could help recognizing the presence of unsound peel but was unable to discriminate between different types of diseases.

For completeness and to verify if the selected two wavelengths are capable of discriminating canker, 70 grapefruit samples (10 samples per condition) were chosen at random from the original 960 samples. The ratio of reflectance images at the selected two wavelengths R_{771}/R_{739} was carried out and image classification procedure (simple thresholding followed by morphological opening) was applied to the ratio image. It was found that 5 out of 70 grapefruits were misclassified achieving around 93.0% of overall classification accuracy and 90.0% canker classification accuracy. Greasy spot and melanose misclassification was the reason for lowering the overall classification rate, the reason being their comparatively higher ratio values. It was observed that as the threshold value was increased the canker classification was getting worse but improving overall accuracy. However after a certain threshold both canker and overall classification accuracies were dropping. The best tradeoff between overall and canker classification accuracies was obtained by the threshold value of 1.14 which achieved the above mentioned figures. The highest spectral slope of canker among all the peel conditions between the two selected wavelengths was the reason behind why the ratio of reflectance at these two wavelengths can distinguish canker. Our research team is

confident of achieving better classification results with higher number of samples and by adjusting the threshold.

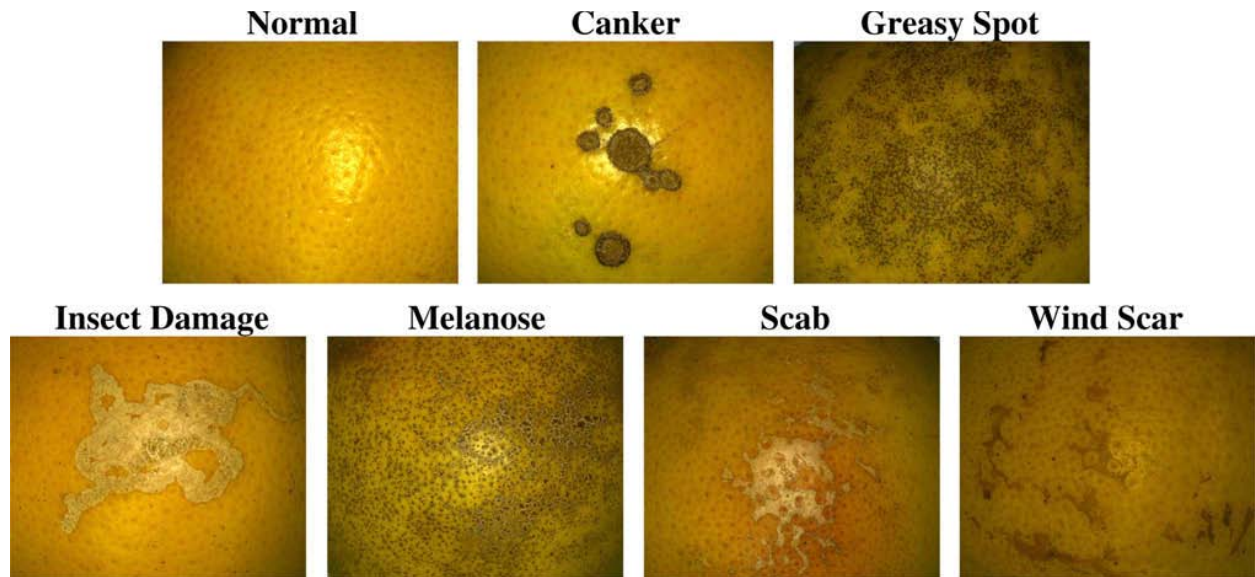


Figure 6-1: Representative normal and diseased peel conditions of grapefruit samples

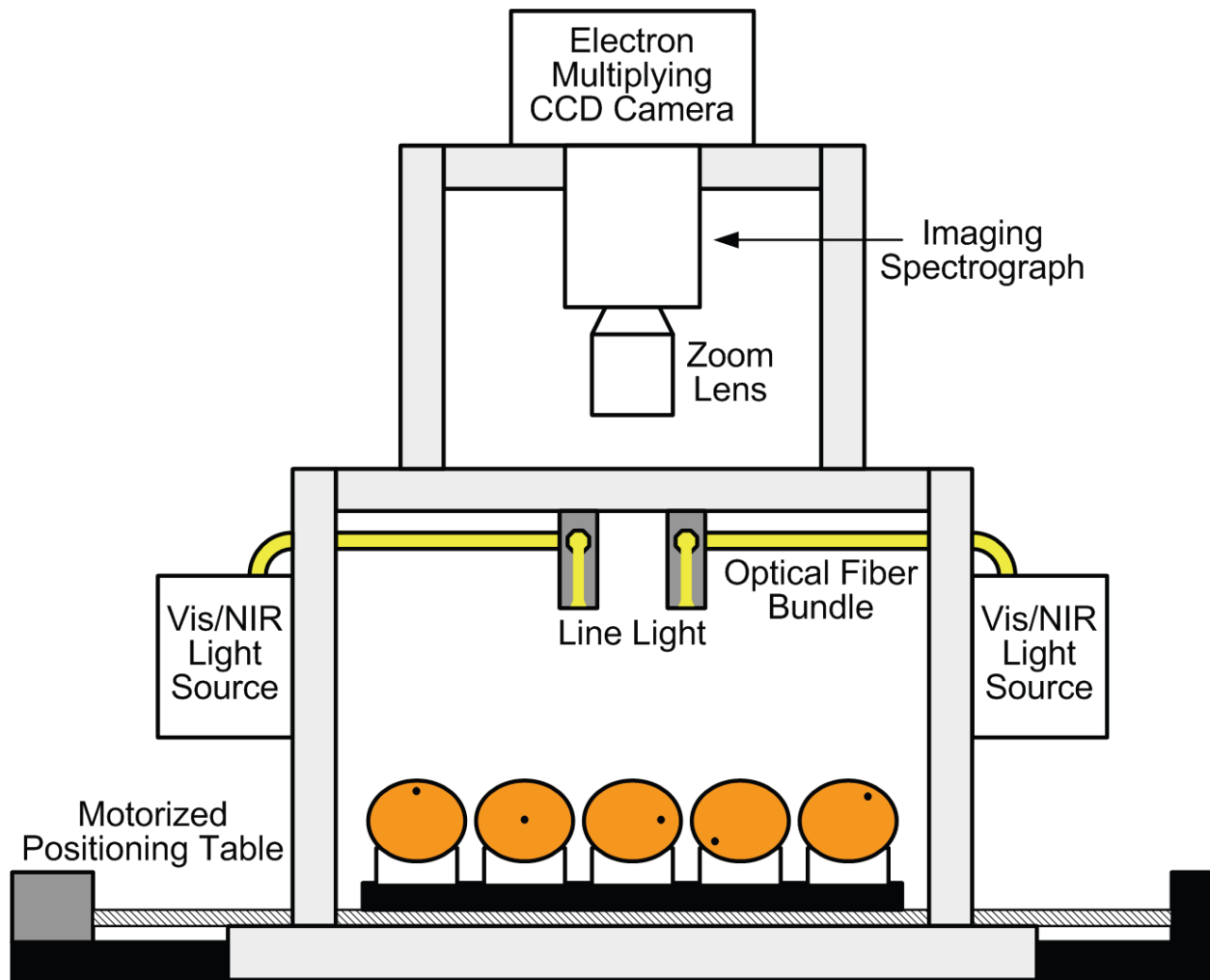


Figure 6-2: Hyperspectral imaging system for reflectance image acquisition from grapefruits

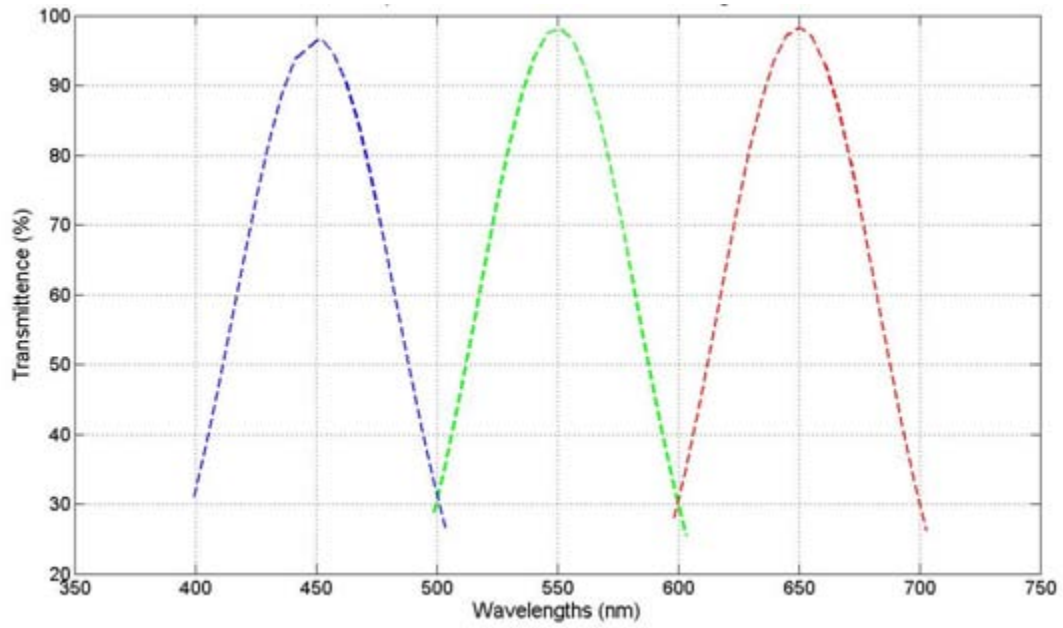


Figure 6-3: Red, Green and Blue filter transmittance characteristics

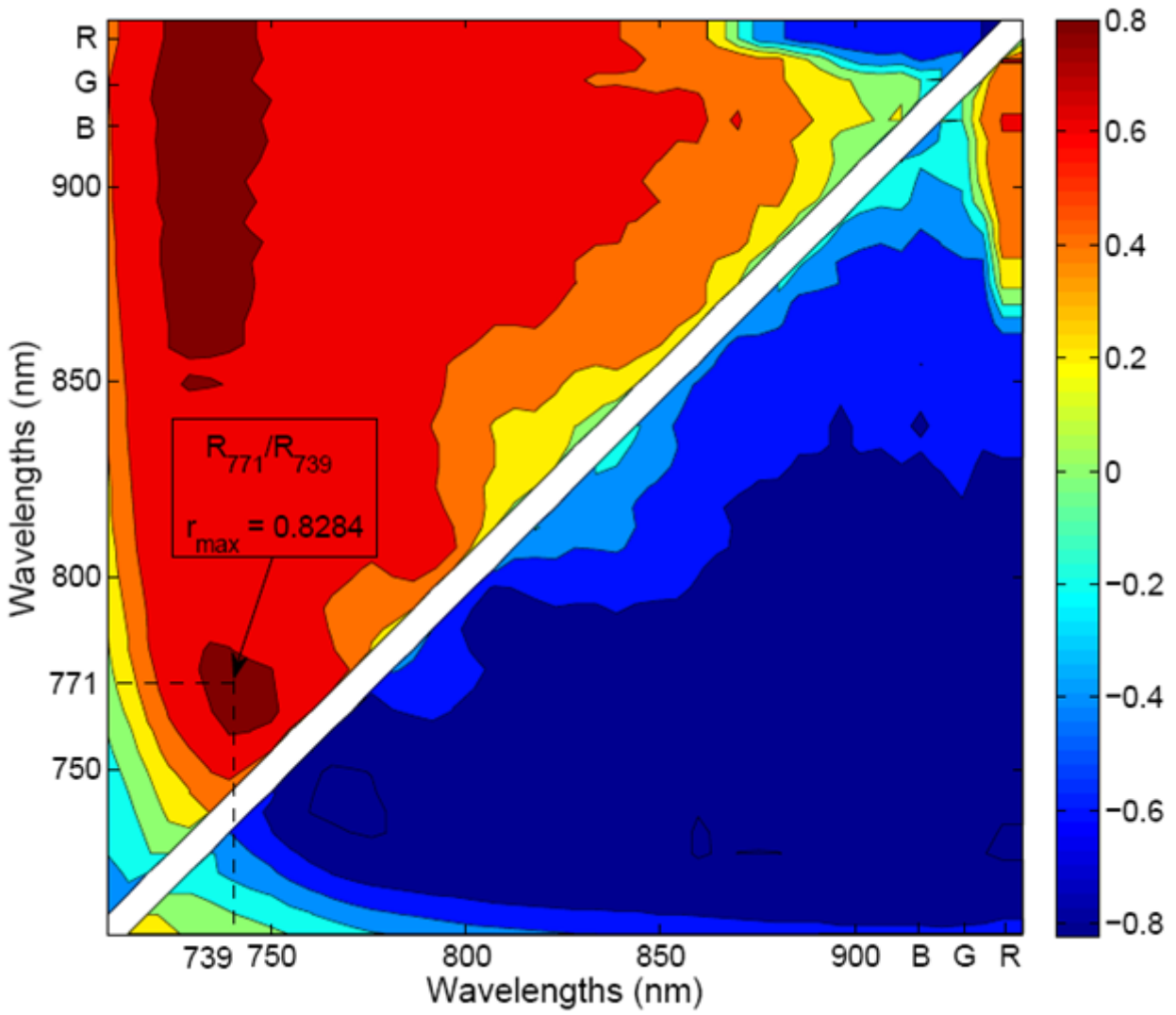


Figure 6-4: Contour of correlation coefficients between two band ratios and fruit peel conditions

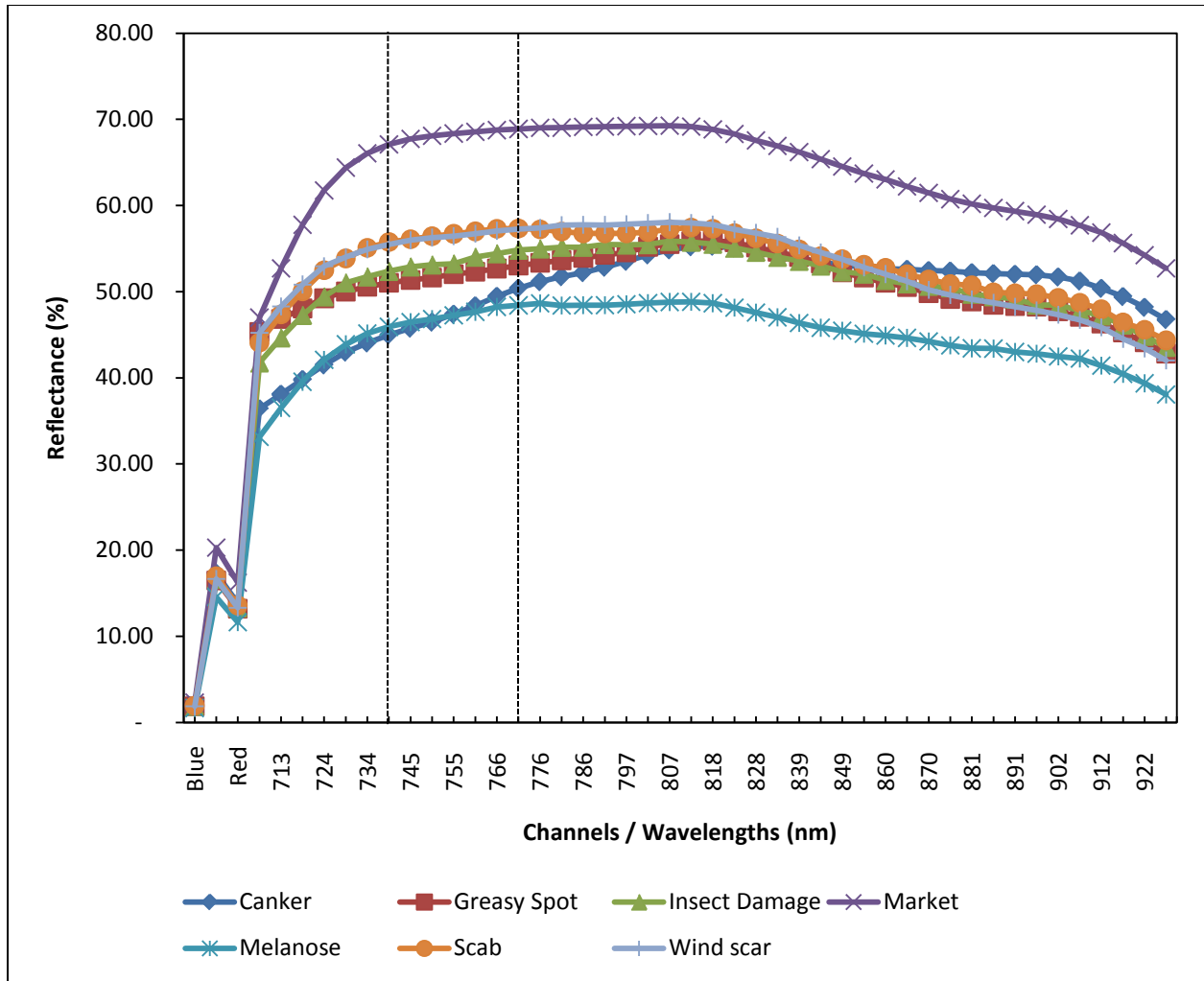


Figure 6-5: Mean reflectance spectra of grapefruits with different peel conditions

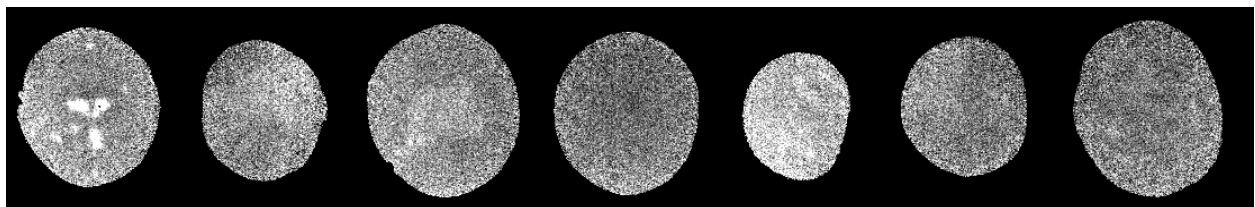
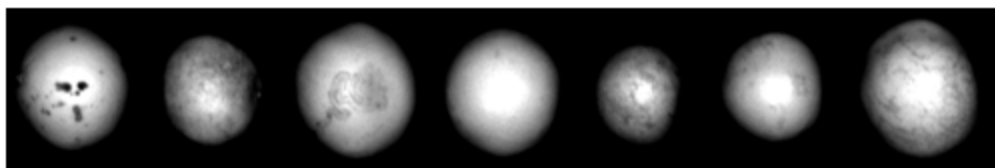
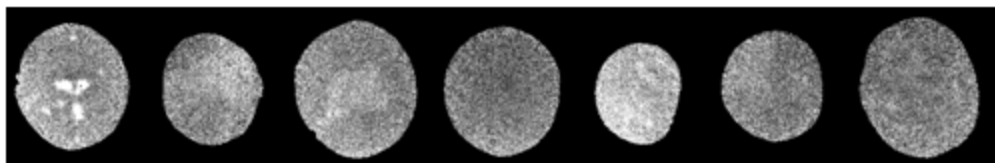


Figure 6-6: Two band Ratio images for different disease conditions. (From L to R Canker, Greasy Spot, Insect Damage, Normal, Melanose, Scab, Wind Scar)

Hyperspectral Image after Masking



Two Band Ratio Image (R_{771}/R_{739})



Simple Thresholding

Binary Image after Thresholding



Morphological Opening

Final Binary Image (for Classification)

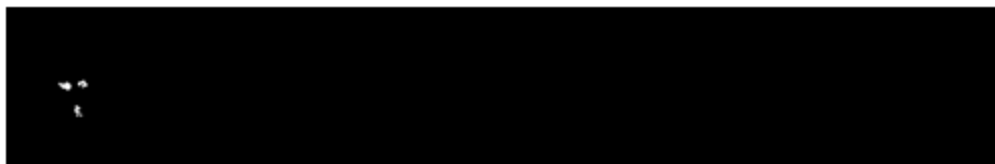


Figure 6-7: Image classification procedure

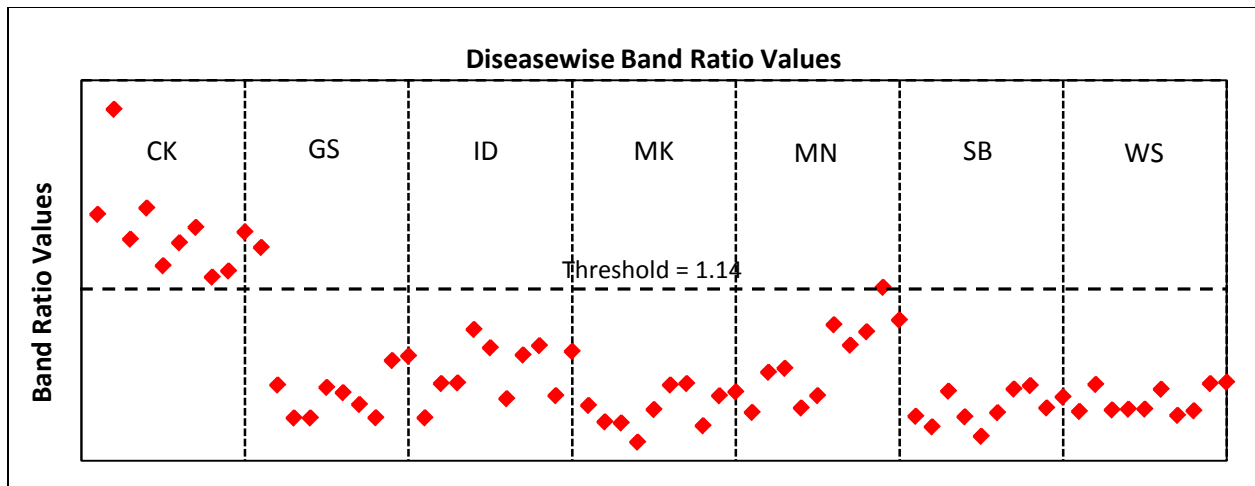


Figure 6-8: Values of two band ratio between 771 and 739 nm (R_{771}/R_{739}) for different peel conditions

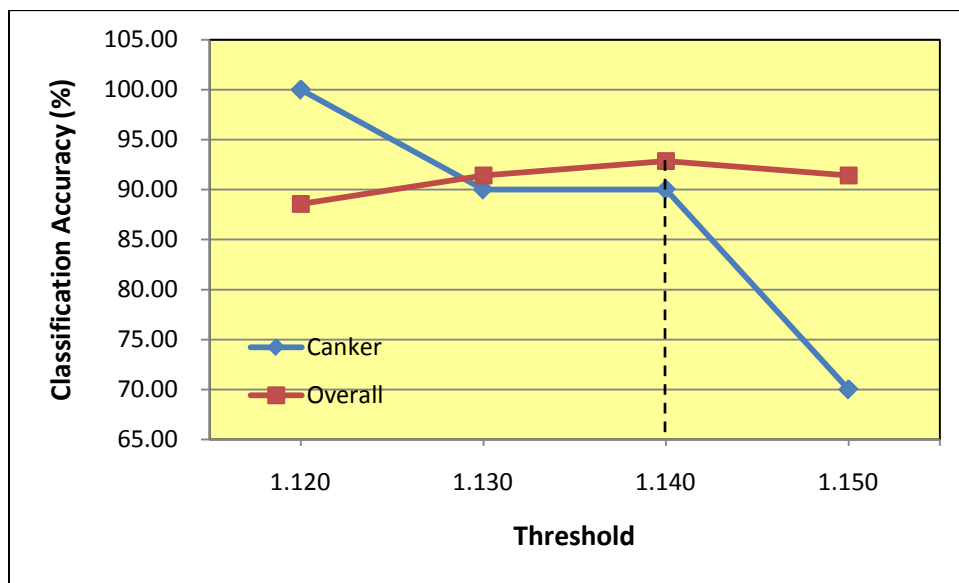


Figure 6-9: Effect of variation of threshold values on classification accuracies

Table 6-1: Summary of classification results

Sr. No.	Disease	No. of Samples	Rule Classifier Threshold	No. of Misclassified	Classification Accuracy (%)
1	Canker	10	1.140	1*	90.00
2	Greasy spot	10	1.140	1	90.00
3	Insect damage	10	1.140	0	100.00
4	Melanose	10	1.140	3	70.00
5	Scab	10	1.140	0	100.00
6	Wind Scar	10	1.140	0	100.00
7	Market	10	1.140	0	100.00
	Overall	70		5	92.86

* Represents the number of misclassified canker samples out of the total of 10 canker infected samples.

CHAPTER 7
COMPENSATION OF EDGE EFFECT ON IMAGES OF SPHERICAL OBJECTS DUE
TO LIGHT SOURCE – HYPERSPECTRAL IMAGING APPLICATION

Introduction

Citrus industry has been a vital source to improving the economy of the State of Florida. Florida produces around 70% of the overall citrus supply throughout United States. Being such a big hub in citrus industry, Florida citrus industry has proved to be a source of income for a considerable number of Floridians. The jobs created by the citrus industry not only include the actual citrus growth but also the peripheral areas like fertilizer production, pest control, disease detection and elimination etc.

Among others, one of the biggest problems which Florida citrus industry is facing is citrus canker. Canker which can spread rapidly under certain conditions and can cause high damage, is affecting the export of citrus from Florida to canker free areas like Europe. Citrus farms are spread over large acres and hence pest control is very time and cost consuming as well as laborious. The solution to this problem could be detecting canker at early stages using some automatic technique. Recently the computer vision and machine learning technologies have been evolved as a potential source to detect the diseases and defects on the biological and horticultural produce. Also the hyperspectral and multispectral techniques have proven to be very effective in automatic disease detection for the biological products like fruits and vegetables.

Essentially all these computer vision technologies include some kind of camera to capture images of the objects which are then processed further for detection of the defects. The distribution of light reflected by the objects and captured by the system camera greatly depends on the position of the light source as well as the geometry of the object. The images captured typically undergo calibration to rectify the spectral as

well as spatial inhomogeneities caused by the lighting system. This calibration is usually based on a plane model correction utilizing a calibrating material with known reflectance. When the object being captured is flat by geometry, above method works perfectly fine. However if the object is not flat then this method introduces problems. In case of spherical objects, the reflection of light causes the edges of the object to appear darker while the central area appears brighter (Gomez et al., 2007; Unay and Gosselin, 2007; Aleixos et al., 2002). This edge effect is always experienced during the inspection of citrus fruits, apples, tomatoes, peaches etc. which are more or less spherical in shape. If the illumination system is improperly implemented it may also cause the edge effect. In many cases this edge effect leads the classification algorithm to draw wrong conclusions by identifying this darkened but sound peel at the edge of the fruit as diseased or defected. In the previous two chapters (canker legion size estimation and disease detection using RGB color image along with NIR monochrome image) one of the most important problems faced by the classification algorithm was this edge effect. The darkened edges of the citrus fruit were being misclassified as canker. To avoid this problem the mask was being applied to the fruit images before it was submitted to the classification algorithm to remove few pixels at the edge (the darkened region at the edge) to minimize the classification error rate. However there is a drawback to this approach. There is a chance that the edge pixels may contain some useful information which could be lost in the masking operation. Also suggestions had been made to add additional lights sources on the sides of the fruit along with the one on top to remove the edge effect. Even if this might solve the problem of edge effect, it is possible that these additional light sources may generate some shadows on the fruit resulting in varied

brightness over the fruit surface. And hence some other method has to be developed to rectify this edge effect in case of the spherical objects to avoid misclassification.

The inappropriate lighting system can also cause the quality of the image to deteriorate and hence it is always recommended to have as effective illumination system as possible to avoid the costly (both monetarily and computationally) preprocessing stages. If the illumination system is not efficient enough, it may generate glare or shadows at particular locations of the object being photographed. It should however be noted that it is not always possible to alter the illumination system because of cost or other constraints. In those situations, it becomes necessary to preprocess the images and make them suitable for further analysis by correcting the images for uniform reflectance.

The issue of edge effect is experienced by classical computer vision system as well as the hyperspectral imaging approach. In hyperspectral imaging technique, we usually capture number of images of the same view at different wavelengths with a very narrow bandwidth (approximately 10 nm). Even if the hyperspectral imaging is a lot different than normal RGB color imaging in principle, it also uses some sort of camera (usually EMCCD), and hence while capturing the images of a spherical object, it faces the edge effect problem. As mentioned earlier, hyperspectral imaging is emerging as a revolutionary technique in the field of automatic disease and defect detection on the agricultural and horticultural products such as fruits and vegetables. However, this technique has been reported to be very sensitive to the illumination system. Hence it becomes necessary to eliminate the negative effects of illumination edge effect,

shadows or saturated regions in order to properly investigate disease defects on the surface of a fruit.

Gomez et al. (2007) introduced a technique which considers the geometry of the object and corrects the edge effect. They assumed the spherical object to be a Lambertian surface and produced its digital elevation model (DEM) by predicting the height of each pixel in the 2-D image. Uniform reflection of the light in all directions irrespective of the direction from which it is being observed, is the inherent characteristic of the Lambertian surface. After doing that they computed a correction factor for each pixel by using the three coordinates (X, Y and height) of each pixel from the digital elevation model. When this correction factor was applied to the original image, the darkening of the edges of the spherical objects was vanished thereby equalizing the grey level of the object surface throughout.

The overall objective of this thesis was to investigate citrus canker identification. In this chapter of the thesis, the technique invented by Gomez et al. for edge effect compensation was re-implemented and was applied to citrus fruits to improve the classification rate of citrus canker by avoiding the false positive errors due to edge blackening. Hence the objectives of this particular exploration were,

- To re-implement the algorithm designed by Gomez et al. for edge effect compensation
- To test the effectiveness of the algorithm by applying it to the citrus fruits and checking the grey level of the fruit image in different areas (edge and center)

Materials and Methods

Hyperspectral Imaging System

A hyperspectral imaging system was used to acquire reflectance images from citrus samples. Schematic diagram of the system is illustrated in Figure 7-1. It is a push

broom, line-scan based imaging system that utilizes an electron multiplying charge-coupled-device (EMCCD) camera (iXon, Andor Technology Inc., South Windsor, CT, USA). The EMCCD has 1004×1002 pixels and is thermoelectrically cooled to -80°C through a double-stage Peltier device. An imaging spectrograph (ImSpector V10E, Spectral Imaging Ltd., Oulu, Finland) and a C-mount zoom lens (Rainbow CCTV H6X8, International Space Optics, S.A., Irvine, CA, USA) are mounted to the camera. The instantaneous field of view (IFOV) is limited to a thin line by the spectrograph aperture slit (30 μm), and the spectral resolution of the imaging spectrograph is 2.8 nm. Through the slit, light from the scanned IFOV line is dispersed by a prism-grating-prism device and projected onto the EMCCD. Therefore, for each line-scan, a two-dimensional (spatial and spectral) image is created with the spatial dimension along the horizontal axis and the spectral dimension along the vertical axis of the EMCCD. The lighting unit consists of two 21 V, 150 W halogen lamps powered with a DC voltage regulated power supply (TechniQuip, Danville, CA, USA). The light is transmitted through optical fiber bundles toward line light distributors. Two line lights are arranged to illuminate the IFOV. A programmable, motorized positioning table (BiSlide-MN10, Velmex Inc., Bloomfield, NY, USA) moves citrus samples (five for each run) transversely through the line of the IFOV. One thousand seven hundred and forty line scans are required for five fruit samples, and 400 pixels covering the scene of the fruit at each scan are saved, generating a 3-D hyperspectral image cube with the spatial dimension of 1740×400 for each band. However as this was just an experimental study and not many samples were used only 700 lines were captured for two fruits saving the 3-D image containing two fruits having dimensions 700×400 for each band. Later on while estimating the

geometric correction factor, the algorithm demands treating single fruit at a time and hence the image of the two fruits was cut into two images each containing one fruit. Spectral calibration of the system was performed using an Hg-Ne spectral calibration lamp (Oriel Instruments, Stratford, CT, USA). Because of inefficiencies of the system at certain wavelength regions (e.g., low light output in the visible region less than 450 nm, and low quantum efficiency of the EMCCD in the NIR region beyond 930 nm), only the wavelength range between 450 and 930 nm (totaling 92 bands with a spectral resolution of 5.2 nm) was used in this investigation. The parameterization and data-transfer interface software for the hyperspectral imaging system were developed using a SDK (Software Development Kit) provided by the camera manufacturer on a Microsoft Visual Basic (Version 6.0) platform in the Windows operating system.

Flat Field Correction

As mentioned in the earlier paragraph, halogen lamps (21 V, 150 W) were used for the illumination in the hyperspectral imaging system. The problem associated with the lighting provided by the halogen lamps is that it suffers with high order of directionality. The above mentioned fact results in varied intensity of the light source in the plane of the scene which is called the spatial variation of light source. In order to take care of this issue, the flat field correction was carried out. During the procedure of the flat field correction the image was pre-processed using a flat white panel of known reflectance. This white panel is usually called a white reference. In this study the white Spectralon panel was used as a reference. The first step was to perform the correction of the hyperspectral image based on the ratio of reflectance of the fruit ($\rho(\lambda)$) and the radiance of the light source ($I(\lambda)$) as denoted by equation (7-1).

$$R(\lambda) = \frac{\rho(\lambda)}{I(\lambda)} \quad (7-1)$$

Where, $R(\lambda)$ is the spatially corrected reflectance image of the fruit. However the reflectance of the fruit ($\rho(\lambda)$) and the radiance of the light source ($I(\lambda)$) cannot be measured as absolute values using the hyperspectral imaging system. Hence in order to achieve this correction the white and dark references were used. Therefore the spatial variation of the light source was rectified using the following equation:

$$R(\lambda) = \frac{R_s(\lambda) - R_d(\lambda)}{R_w(\lambda) - R_d(\lambda)} * \Psi_{Ref} \quad (7-2)$$

Where,

λ = Wavelengths

$R_s(\lambda)$ = Original (uncorrected) reflectance image of the fruit

$R_d(\lambda)$ = Reflectance image of dark current

$R_w(\lambda)$ = Reflectance image of white reference

Ψ_{Ref} = Reflectance factor of the white reference panel

The dark current image $R_d(\lambda)$ was acquired with the light source off and the camera lens covered with the cap and the white reference image $R_w(\lambda)$ was acquired using the white Spectralon panel. The actual reflectance factor (Ψ_{Ref}) of the white panel was around 98.5% in the wavelength range covered for the study (450 – 930 nm) however in this exploration for simplicity it was assumed to be 100%. The correction mentioned in the equation (7-2) was applied to all the monochrome images in the wavelength range mentioned above. The relative reflectance images processed using above mentioned procedure were then multiplied by a factor of 10,000 so as to achieve the pixel values for resultant images in the range 0 to 10,000. This multiplication factor was applied in order to attain the pixel value range comparable to that of the original data from the

hyperspectral imaging camera and also to reduce the round off errors for further data analysis. Further details about the flat field correction can be found in Qin et al. (2008).

Image Masking and Binning

After correcting the images for spatial variation the mask for the fruit image was created with an intention of removing the noisy background. The mask template was formed by determining the threshold value by visual inspection of one of the monochrome images (765 nm) that had good contrast between fruit surface and the background. The mask was then applied to extract the fruit pixels and remove the background from all the monochrome images in the hyperspectral image cube. The subsequent analysis used these masked images for further processing.

Since hyperspectral image involves a large amount of data, spatial binning technique is used for data reduction. In this process the image data is averaged by few neighboring pixels in horizontal or vertical direction or in both directions (as per requirement) at each wavelength. Image binning was used during first two studies but it was not performed during the third part i.e., edge effect compensation as it was just an experimental study. The algorithms for flat field correction as well as image masking and binning were developed by our research team (Qin et al. 2008) during prior explorations. For further details one can refer to Qin et al. 2008.

Derivation of Geometric Correction Factor

In order to remove the blackened edges of the image of citrus fruit due to the edge effect and to make the intensity of the fruit surface uniform throughout, the geometric correction was applied to the image. The expression for the geometric correction factor (ϵ_g) was derived by starting with the illumination model. The illumination provided to the spherical object by the light source ($I_T(\lambda)$) was modeled as a function of two illumination

components, the direct component ($I_D(\lambda)$) and the fuzzy component ($I_F(\lambda)$). As the name suggests the direct component directly comes from the light source. The illumination provided by the direct component depends on the angle of incidence (Φ) which is the angle between the beam of direct light and the direction normal to the surface at the point of incidence. On the other hand, fuzzy light is the indirect illumination provided by numerous reflections of the light from the surrounding (i.e., from the walls of the illumination chamber). The model described above can be represented in the mathematical form in the following way:

$$I_T(\lambda) = I_D(\lambda) * \cos(\Phi) + I_F(\lambda) \quad (7-3)$$

It should be noted that the model mentioned in equation (7-3) takes into account the geometry of the object. As mentioned earlier we had assumed the surface of the citrus fruit to be a Lambertian surface. This type of surface is recognized by the fact that irrespective of the direction of observation, it reflects the light falling on it in exactly the same way in all the directions and this reflected light obeys the cosine law by distributing reflected energy in proportion to the cosine of the incidence angle (Φ) (Green and MacDonald 2002). According to Foley et al. (1996) and Gomez et al. (2007) also, in case of the Lambertian surface, the light received by the viewer depends on the angle of incidence (Φ) (same as what we used in the direct component of the illumination). So it can be concluded that the illumination model described in equation (7-3) exactly suits the needs.

If we were to capture the images of the flat surface, with light source located right above the surface, the illumination model mentioned in equation (7-3) can be expressed as,

$$I(\lambda) = I_D(\lambda) + I_F(\lambda) \quad (7-4)$$

Where,

$I(\lambda)$ is the total average lights which is nothing but radiance of the light source mentioned in equation (7-1). In the present study the light source was located right above the object being captured. Hence it should be noted that if the light source is located right above the object, the illumination model no longer depends on the angle of incidence (Φ). When it comes to a flat surface, the angle Φ is equal to zero for every point on the surface, making the “ $\cos(\Phi)$ ” term in equation (7-3) equal to one every time. So one should keep in mind that equations (7-3) and (7-4) represent the same model while capturing the images of a flat object. However they are potentially different models when it comes to capturing a spherical object (provided that the light source is located right above the object being captured).

In order to derive the expression for the geometric correction factor (ϵ_g), two parameters, α_D and α_F were defined. The parameter α_D was the ratio of the direct light ($I_D(\lambda)$) and the total average lights ($I(\lambda)$), while the parameter α_F was the ratio between the fuzzy light ($I_F(\lambda)$) and the total average lights ($I(\lambda)$). Hence,

$$\alpha_D = \frac{I_D(\lambda)}{I(\lambda)} \quad (7-5)$$

And,

$$\alpha_F = \frac{I_F(\lambda)}{I(\lambda)} \quad (7-6)$$

Rearranging equations (7-5) and (7-6) we get,

$$I_D(\lambda) = I(\lambda) * \alpha_D \quad (7-7)$$

$$I_F(\lambda) = I(\lambda) * \alpha_F \quad (7-8)$$

If (7-7) and (7-8) were substituted in (7-4) we get the following identity:

$$\alpha_D + \alpha_F = 1 \quad (7-9)$$

Substituting (7-7) and (7-8) in (7-3) we get the following expression.

$$I_T(\lambda) = [I(\lambda) * \alpha_D * \cos(\Phi)] + [I(\lambda) * \alpha_F] \quad (7-10)$$

Now rearranging equation (7-9) to get expression for α_F and substituting that in equation (7-10) we get,

$$I_T(\lambda) = I(\lambda) * [\alpha_D * \cos(\Phi) + (1 - \alpha_D)] \quad (7-11)$$

Rearranging equation (7-11) to obtain expression for $I(\lambda)$ in terms of $I_T(\lambda)$, α_D and Φ ,

$$I(\lambda) = \frac{I_T(\lambda)}{[\alpha_D * \cos(\Phi) + (1 - \alpha_D)]} \quad (7-12)$$

Substituting equation (7-12) in equation (7-1) and rearranging we get,

$$\frac{\rho(\lambda)}{I_T(\lambda)} = \frac{R(\lambda)}{[\alpha_D * \cos(\Phi) + (1 - \alpha_D)]} \quad (7-13)$$

Equation (7-13) represents the spatially as well as geometrically corrected image.

Equation (7-13) suggests that if the reflectance image of the fruit ($\rho(\lambda)$) is divided by the illumination model which considers the spherical geometry of the fruit ($I_T(\lambda)$), we achieve the spatial and geometrical correction of the image. The expression on the right hand side of equation (7-13) proposes that we can achieve the geometric correction of the spatially corrected image ($R(\lambda)$) by dividing it with the factor of $[\alpha_D * \cos(\Phi) + (1 - \alpha_D)]$. This expression represents the expression for the Geometric correction factor (ϵ_g).

Hence,

$$\epsilon_g = [\alpha_D * \cos(\Phi) + (1 - \alpha_D)] \quad (7-14)$$

Rewriting the equation (7-13) in terms of geometric correction factor,

$$\rho(\lambda) = \frac{R(\lambda)}{[\alpha_D * \cos(\Phi) + (1 - \alpha_D)]} = \frac{R(\lambda)}{\epsilon_g} \quad (7-15)$$

Where,

$q(\lambda)$ is the spatially as well as geometrically corrected image.

Gomez et al. (2007) had defined α_F as the ratio between the average amount of light (across all bands) detected by CCD (levels of grey) at the points those coincide with the perimeter of the fruit and the total average amount of light received by the CCD from the whole fruit. At the perimeter, as the angle of incidence (Φ) is 90 degrees, the only component that provides lighting to the fruit is the fuzzy illumination ($I_F(\lambda)$) while for the entire fruit surface the lighting is the combination of direct ($I_D(\lambda)$) and fuzzy illumination ($I_F(\lambda)$) i.e., $I(\lambda)$. Gomez et al. conducted a study and plotted the value of α_F for different points on the perimeter of the clemenules mandarins and then averaged them for each fruit to get value of α_F for every fruit. Finally the mean value of α_F was computed, by taking the mean of values of α_F for all the fruits, to be 0.4896. Also when he plotted the values of α_F for all the points on the perimeter of one single fruit the values were distributed around the mean value very close to 0.4896. The mean value of parameter α_D was then calculated from equation (7-9) as 0.5104. According to the hypothesis of Gomez et al. (2007), the parameters α_D and α_F are related to the illumination system and not to the objects being captured. Hence the values of these parameters were assumed to be constant during their entire study. In the case of our investigation, the value of α_D was not estimated through tests but it was assumed to be a constant and equal to the mean value obtained by Gomez et al. during their studies of mandarin (i.e., equal to 0.5104).

Generating the Digital Elevation Model

The geometric correction factor (ε_g) is a function of two elements, the parameter α_D which is the ratio direct lights (I_D) and the total average lights (I) and the angle of

incidence Φ which is the angle between the beam of direct light and the direction normal to the surface. In order to calculate the angle Φ , we need to know the Cartesian coordinates (i.e., X, Y and heights) of each pixel of the fruit image. However, from the 2-D image of the fruits we obtain only the X and Y coordinates and not the height of any pixel. This is precisely the reason why we generate the Digital Elevation Model (DEM). DEM is the 3-D model of the fruit produced from the 2-D image. The basic assumption in the process of developing this 3-D DEM is that the citrus fruits are quasi-spherical. We can compute the geometric correction factor ε_g for each pixel as soon as the model has been constructed and elevations (heights) of each of the pixels have been estimated. However, the DEM should be developed separately for each fruit because of the possible difference in the sizes of different fruits. The subsequent steps should be followed to construct this DEM:

Step I – Locating the center of mass (C_g) of the fruit and determining the interpolation network meridians: In order to locate the center of mass (C_g) of the fruit we first need to determine the pixels that belong to the fruit and separate them from the background i.e., to obtain the fruit mask. This mask was extracted from the image by using an algorithm previously developed by our research team as mentioned in the 'Image Masking and Binning' section (Qin et al., 2008). This mask creates the black and white binary image with white pixels (value = 1) indicating pixels belonging to fruit while black pixels (value = 0) represent the background. Once the mask was extracted, the X and Y locations of the pixels on the edge of the mask were identified. Now in order to locate the center of mass, few (n_p) equidistant points on the edge of the mask were selected which were called pilot points. The higher the number of pilot points selected,

the more accurate the location of center of mass and the more accurate end results we can obtain. In this study we selected 30 ($n_p = 30$) pilot points on the edge. This was done by translating the edge of the mask to the origin (0, 0) and then grabbing the (X, Y) locations of all the pixels on the edge at an angular step of $(2\pi / n_p - 1)$. Then the center of mass was (C_g) calculated using the equation (7-16).

$$C_g = \frac{1}{n_p} * \sum_{i=1}^{n_p} P_i \quad (7-16)$$

Where, P_i are the (X, Y) locations of the selected n_p pilot points on the edge. Now the lines joining each of those P_i points and the center of mass (C_g) are nothing but the meridians of interpolation network in the DEM. Figure 7-2 shows the 30 selected pilot points (P_i) on the edge of the mask of the fruit image, which when connected with the center of mass (C_g) forms the meridians of the interpolation network. The pilot points are highlighted as solid circles while the center of mass is shown by a star.

Step II – Obtaining the maximum height of the fruit: To facilitate the construction of digital elevation model (DEM) it is mandatory to obtain the height coordinate i.e., elevation of each pixel of the fruit image. To achieve this goal, the maximum height of the fruit was determined and then the elevations of each individual pixels were obtained by interpolation. The maximum height of the fruit was computed from the distance between the center of mass (C_g) and the pilot points (n_p) using the equation (7-17).

$$h_c = \frac{1}{n_p} * \beta * \sum_{i=1}^{n_p} \|C_g P_i\| \quad (7-17)$$

Where,

$\|C_g P_i\|$ = Distance between center of mass C_g and pilot point P_i i.e., the radius of the fruit.

β = Flattening factor.

As the algorithm may be sensitive to surface irregularities and may result in estimating less spherical shape, the flattening factor was used to take into account such irregularities which are often found in the biological products. However in the present study the flattening factor (β) was assumed to be one for simplicity.

Step III – Determining the elevations of the interpolation network: As

mentioned earlier the elevations of each of the image pixels were calculated using the maximum height of the fruit (h_c). But before that the nodes of interpolation and the interpolation network need to be obtained. This was done by subdividing each of the radii (C_gP_i) into few numbers of radii segments (r_{ij}) and then locating the interpolation node at the end of each of the segments. The (XY) coordinates of all the nodes were also determined during the process. In the segment r_{ij} , the index ‘i’ varies from 1 to n_p for n_p number of radii ($n_p = 30$ in our case) and the index ‘j’ varies from 1 to the number of segments. In this study we chose to divide each of the radii into 16 segments. After determining the (XY) coordinates of the nodes, their heights (h_{ij}) were evaluated by modeling the ellipses in the plane formed by each of the radii (C_gP_i) and the maximum height (h_c) of the fruit with (C_gP_i) and h_c to be the semi axes of the ellipse in the respective plane. The following characteristic equation of ellipse was used to compute the heights of the nodes i.e., h_{ij} .

$$\frac{r_{ij}^2}{\|C_gP_i\|^2} + \frac{h_{ij}^2}{h_c^2} = 1 \quad (7-18)$$

This procedure was repeated for n_p number of times for the n_p number of ellipses formed on the n_p number of planes in order to compute the heights of all the nodes on the n_p number of radii. Once this was done we had obtained the (X, Y, Z) coordinates

for all the interpolation nodes. The interpolation network for the DEM was formed by these coordinates of all the nodes of interpolation.

Step IV – Acquiring the elevations of each pixel belonging to fruit by interpolation: After the interpolation network was formed and the (X, Y, Z) coordinates of all the interpolation nodes were computed, the elevations of all the intermediate pixels of the fruit were obtained by interpolation. The MATLAB commands 'meshgrid' and 'griddata' were used for the task. The command 'meshgrid' was used to duplicate the X and Y coordinates of all the pixels of the fruit image for generating the 3-D model of the fruit. The command 'griddata' was used in conjunction with the (X, Y, Z) coordinates of the interpolation nodes in order to obtain the Z or height coordinates i.e., elevations of all the intermediate pixels. After this was done the 3-D wireframe parametric surface of the fruit was produced using the MATLAB command 'mesh'. Once the above mentioned four steps were followed the 3-D digital elevation model (DEM) was generated, the properties of which were then used to estimate geometric correction factor for each fruit pixel.

Estimation of Geometric Correction Factors

As derived earlier, the geometric correction factor (ϵ_g) is given by the following equation (7-19).

$$\epsilon_g = \alpha_D * \cos(\Phi) + (1 - \alpha_D) \quad (7-19)$$

It should be recalled that the geometric correction factor (ϵ_g) was a function of two parameters, the parameter α_D which is the ratio of direct lights (I_D) and the total average lights (I) and the angle of incidence Φ which is the angle between the beam of direct light and the direction normal to the surface. The geometric parameters obtained from

the digital elevation model were exploited for estimating the value of angle Φ . The angle Φ was calculated from the spatial coordinates of each pixel (i.e., X, Y, Z Cartesian coordinates) as follows:

$$\tan(\Phi) = \frac{\sqrt{X^2 + Y^2}}{Z} \quad (7-20)$$

Where, Z is the elevation of each pixel (h_{XY}) estimated in the digital elevation model. The geometric correction factor (ϵ_g) was estimated for each pixel using the equations (7-19) and (7-20). The constant α_D was obtained from the work of Gomez et al. (2007) as equal to 0.5104.

After calculating the geometric correction factors (ϵ_g) for all the pixels, each pixel is divided by the corresponding correction factor. One should note that while calculating the center of mass (C_g) we had translated the edge of the fruit mask to the origin (0, 0). So while applying the correction factor to each pixel one should take enough care to divide each pixel by appropriate correction factor by properly matching the contour of the correction factors with that of the mask.

Algorithm Validation Tests

In order to validate the edge effect compensation algorithm few tests were conducted. A couple of market quality oranges were purchased from the supermarket for the tests. The first experiment was carried out to prove that the same region of the citrus fruit has similar reflectance in different areas of the image after applying the geometric correction factor. This experiment was conducted by rotating the fruit in steps of approximately 20 degrees and capturing the images at all the locations. The reflectance of the same region of interest in the fruit was measured at different locations and compared. The reflectance measurement was done using ENVI 4.3 software (ITT

Visual Information solutions, Boulder, CO USA). The fruits were marked with angular graduations with step size equal to 20 degrees using a black permanent marker. Each fruit was marked with three regions of interest, square in shape and random in size. The images of the fruit at 0, 20 and 40 degrees were captured and the mean reflectance of each of the region was plotted (at 0, 20 and 40 degrees) separately as the reflectance spectra by averaging the reflectance of each pixel included in the region of interest using ENVI 4.3. The pixels in the regions of interest were selected in the zoom window manually, by using various drawing methods (e.g., polygon, rectangle, ellipse, point, grow, and merge etc.). Enough care was taken while selecting the pixels to avoid the edges of the square regions marked with the permanent marker. The reflectance spectra of the region of interest of the fruit, before and after applying the correction factor were compared to identify the effect of applying the correction.

The second experiment included measuring and comparing the reflectance of the market quality orange peel at different locations before and after applying the geometric correction factor. This was done by acquiring the reflectance spectra of the different regions of interest of the fruit over the wavelength range for the study (450 – 930 nm) and comparing them. The aim of this trial was to prove that the reflectance of the pixels in different regions of the fruit equalizes or at least the difference between the reflectance of pixels at edge and that of at the center reduces after application of the correction. The technique similar to that of the first test was used for second test also. The three regions of interest were selected in such a way that one was at the center and the other two were closer to the edge. The reflectance of all the three regions of interest at 0, 20 and 40 degrees was plotted in separate plots and compared for

evaluating the effect of the correction. The reflectance measurement was done in the same way as that in the first experiment.

Results, Observations and Discussion

Digital Elevation Model Observations

The digital elevation model (DEM) was constructed in order to obtain the geometric parameters needed to compute the geometric correction factor for each pixel. The process was initiated by acquiring the mask of the fruit and choosing 30 pilot points (P_i) on the edge of the mask for computing the center of mass of the fruit. The Figure 7-2 portrays the mask obtained from the fruit image along with the pilot points on the perimeter of the mask. After the pilot points were captured, the meridians of the interpolation network were formed by joining the center of mass (C_g) and all the pilot points (P_i). Once the meridians are in place, the maximum height (h_c) of the elevation model of the fruit was calculated. Each meridian of the interpolation network was then divided into 16 segments (r_{ij}) to obtain the nodes of the interpolation. Figure 7-3 shows these interpolation nodes (green in color) on one of the meridians of the network along with all the 30 pilot points (red in color) on the perimeter of the fruit. The elevations of all the nodes were then computed by modeling the ellipses in the plane formed by each of the radii (C_gP_i) and the maximum height (h_c) of the fruit with (C_gP_i) and h_c to be the semi axes of the ellipse in the respective plane. One such transversal plane along with the computed elevations of the respective nodes are demonstrated in the Figure 7-4. The modeled ellipse with the interpolation nodes on it can be viewed from Figure 7-5 and Figure 7-6 which are drawn in Solid Works 2009 - 2010. Figure 7-5 is a side view (viewed from direction normal to the transversal plane in which ellipse is modeled) and Figure 7-6 is the 3-D view of that ellipse. Figure 7-3 shows the view of Figure 7-6 taken

from top (i.e., top view of Figure 7-6). The interpolation network was generated as soon as the estimation of elevations of all the nodes on all the meridians were estimated and the (X, Y, Z) coordinates of all the nodes were determined. The construction of interpolation network was followed by the estimation of heights of all the intermediate pixels by interpolation. This concluded the structuring of the digital elevation model. The digital elevation model for one of the fruits is shown in Figure 7-7.

Geometric Correction Factor Observations and Results

As noted earlier, the geometric correction factor (ϵ_g) was a function of two elements, the parameter α_D which is the ratio of direct lights (I_D) and the total average lights (I) and the angle of incidence Φ which is the angle between the beam of direct light and the direction normal to the surface. However, as mentioned previously the parameter α_D had been assumed to have a constant value of 0.5104 that was obtained from the work of Gomez et al. (2007) which he computed as the average value of α_D for different citrus fruit samples. So the geometric correction factor (ϵ_g) only depends on angle of incidence Φ . The angle Φ was calculated for each pixel based on the Cartesian coordinates of that pixel which were obtained from the digital elevation model. The geometric correction factor for each pixel was then plotted in the XY plane to examine its contour. Figure 7-8 shows this contour of the geometric correction factor. When an image of the citrus fruit is captured, the top-center area of the fruit appears brightest and as we move towards the fruit edge the image becomes darker. So when we apply the geometric correction to the image, ideally the pixels at the center of the image should get divided by a factor of 1 as this is the brightest region of the fruit while as we go away from the center towards edge the geometric correction factor should have lower value.

Figure 7-8 supports the ideology mentioned here. The geometric correction factor had the highest value (i.e., 1) in the central region while it was found to be decreasing gradually towards the edge in concentric manner with minimum at edge. Also one other point to be observed in Figure 7-8 is that the geometric correction factor of the fruit background (i.e., the pixels of the image those don't belong to fruit) is 1 which is logical as these pixels need not to be corrected.

The effect of application of the geometric correction to one of the citrus samples is shown in the Figure 7-9. The left image is the citrus fruit before application of the geometric correction while the right one is after application of the correction. The fruit was affected with canker and the image was captured during prior studies. The image shown is the monochrome image at 724 nm. As can be viewed from the left image, before applying the algorithm the image appeared brighter in the central part while the peripheral area was darker. As discussed earlier, this was because of the spherical geometry of the fruit which resulted in this edge effect. Clearly the image after correction appears brighter than the one before correction. Also the brightness of the entire image seems to have more uniformity throughout than the uncorrected image.

Validation Test Results

The first experiment was to measure and compare the reflectance of the same region of the fruit at different orientations of the fruit, before and after applying the geometric correction. Figure 7-10 shows one of the fruits marked with the angular graduations and the regions of interest. The reflectance spectra of all three regions of interest were plotted before and after application of the geometric correction. For demonstration purposes the reflectance spectra of region of Interest 3 (ROI 3) are shown in the Figure 7-11(A) and 7-11(B) before and after application of the geometric

correction factor respectively. As can be seen from Figure 7-11(A), the reflectance of the ROI 3 at 0 and 20 degrees are pretty close to each other. However the reflectance at 40 degrees is quite lower than the other two. One reason behind this could be the number pixels selected in the region of interest at different angles. At 0 and 20 degrees the pixels selected in the ROI were 385 and 367; respectively however those selected at 40 degrees were 230. As we rotated the fruit by higher angle lesser the portion from the ROI was visible to the camera and hence at 40 degrees a fewer number of pixel were selected. Also it should be noted that the maximum reflectance has occurred at around 660 nm at all three angles. The maximum reflectance at 0 degrees was around 60%, at 20 degrees it was approximately 57% and at 40 degrees it was close to 39%. These observations make sense because as the angle of rotation was increased the portion at top moved closer to the edge in the darkened region (which is a result of edge effect). Now if we observe the reflectance spectra of ROI 3 after geometric correction in Figure 7-11(B) it can be witnessed that the maximum reflectance at 0, 20 and 40 degrees is respectively 67, 65 and 49% approximately. The significant improvement in the reflectance of the fruit image after the correction is clearly visible from the spectra. Also the difference between reflectance of the region at different orientations can be observed to be reduced after application of the correction. These results conclude that the same region of the fruit had similar reflectance in different areas of the image after subjecting it to the geometric correction proposed in the study.

The second experiment consisted of measuring and comparing the reflectance of different regions of the fruit before and after application of the correction. As mentioned earlier three regions were selected on the fruit image, one at center and two closer to

the edge. The reflectance of all three regions was measured at 0, 20 and 40 degrees. The reflectance spectra of all three regions captured at 40 degrees rotation are shown in Figure 7-12 for display purpose. Figure 7-12(A) shows the spectra before correction and Figure 7-12(B) shows that after the correction was applied. Obviously the two plots differ from one another. The spectra of the three regions before applying the correction are quite dispersed and they portray considerably high degree of variability in spite of being a part of the same homogeneous fruit peel. On the other hand after correction all the spectra can be seen to be overlapping each other in Figure 7-12(B). The difference between the reflectance of the three regions has reduced by significant amount. Also if observed carefully the maximum reflectance of ROI 1, 2 and 3 was found to be 45, 33 and 39% at around 660 nm before correction. After the correction was applied, these numbers increased to 51, 45 and 49%. These numbers are effective enough to highlight the consequences of application of geometric correction. At the rotation of 40 degrees the ROI 1 had curvature only in one direction while ROI 2 and 3 had curvature in two directions. That was the reason behind ROI 1 having highest reflectance out of the three regions. Also after closer examination it was observed that ROI 2 had a little mark of a blue pen inside it. This might have caused ROI 2 to have the minimum reflectance of all. The fruit being observed had uneven curvature in the regions 2 and 3 which also could have contributed to the different reflectance of the regions. It was concluded after the test that after application of the geometric correction different regions on the fruit portray similar reflectance.

In the above experimentation all three regions represented normal peel conditions on the same fruit belonging to the marketable class. However, the darkening edge effect

contrasted with the brighter central area, creating confusion in the classification algorithm (which can be seen from the spectra in Figure 7-12(A)). The point to be noted here is that, when applying the correction, edge effect variability within the same class reduced significantly (refer to the spectra in Figure 7-12(B)). This fact is very important from the point of view of an automatic segregation system as it reduces the misclassification rate by sizeable amount, regardless of the class of peel conditions being considered. The algorithm was implemented for correcting the monochrome images captured by the hyperspectral imaging system, however according to the inventor of the method, Gomez et al. (2007); the methodology can be used for any single band images including basic three channel RGB color images.

Summary and Conclusion

Florida citrus industry is a central part of the economy of the State of Florida. It has provided tremendous amount of employment to the residents not only in the agricultural production areas but also related jobs like packaging, processing, shipping agricultural chemicals and so on. Florida citrus industry has been facing the threat of canker for quite some time and the state government is continuously stressing on identifying the diseased citrus fruits and preventing them from entering canker-free areas inside and outside United States. The automatic disease detection systems using computer vision, image processing and pattern recognition techniques have proven themselves to be very effective in identifying and separating cankerous citrus fruits from other peel conditions. One of the major concerns every computer vision system faces while capturing the images of a spherical object is the edge effect. This edge effect may cause the segregation algorithm to confuse between sound fruit peel and the diseases due to darkening of the edges. A model to compensate for this edge effect was

implemented following the study of Gomez et al. (2007) during this course of exploration. The algorithm assumes the fruit to be a Lambertian ellipsoidal surface. With this assumption a 3-D digital elevation model of the fruit was developed from its 2-D image. The cartesian coordinates (X, Y and Z) of each pixel on the fruit surface were determined from the digital elevation model. These coordinates were used to estimate the geometric correction factor (ϵ_g) for each pixel. When the reflectance of each pixel was divided by the corresponding correction factor (ϵ_g), the image corrected for the curvature effect of the spherical object was obtained. During the process of correction, the value of α_D from Gomez et al. (2007) was assumed, yielding excellent image enhancement. The only disadvantage of the method is that each fruit has to be treated separately in order to create the digital elevation model. As we can process only one fruit at a time with this methodology, it is time consuming and thus computationally expensive. If the algorithm is implemented in a real time online application it may demand a considerably fast processor.

As a consequence of this geometric correction it becomes feasible to retrieve the portion of the reflected signal that was lost while capturing an image of a spherical object due to its curvature. We can then estimate the true reflectance that should actually reach the camera. The correction helped to equalize the intensity of radiation over the whole surface of the fruit and hence eliminate edge effect darkening. Additional experiments were conducted to show that the reflectance becomes more uniform over the fruit surface thus correcting the image for geometric variation. These results might interest the researchers and scientists as they lead to reduced misclassification due to edge effect.

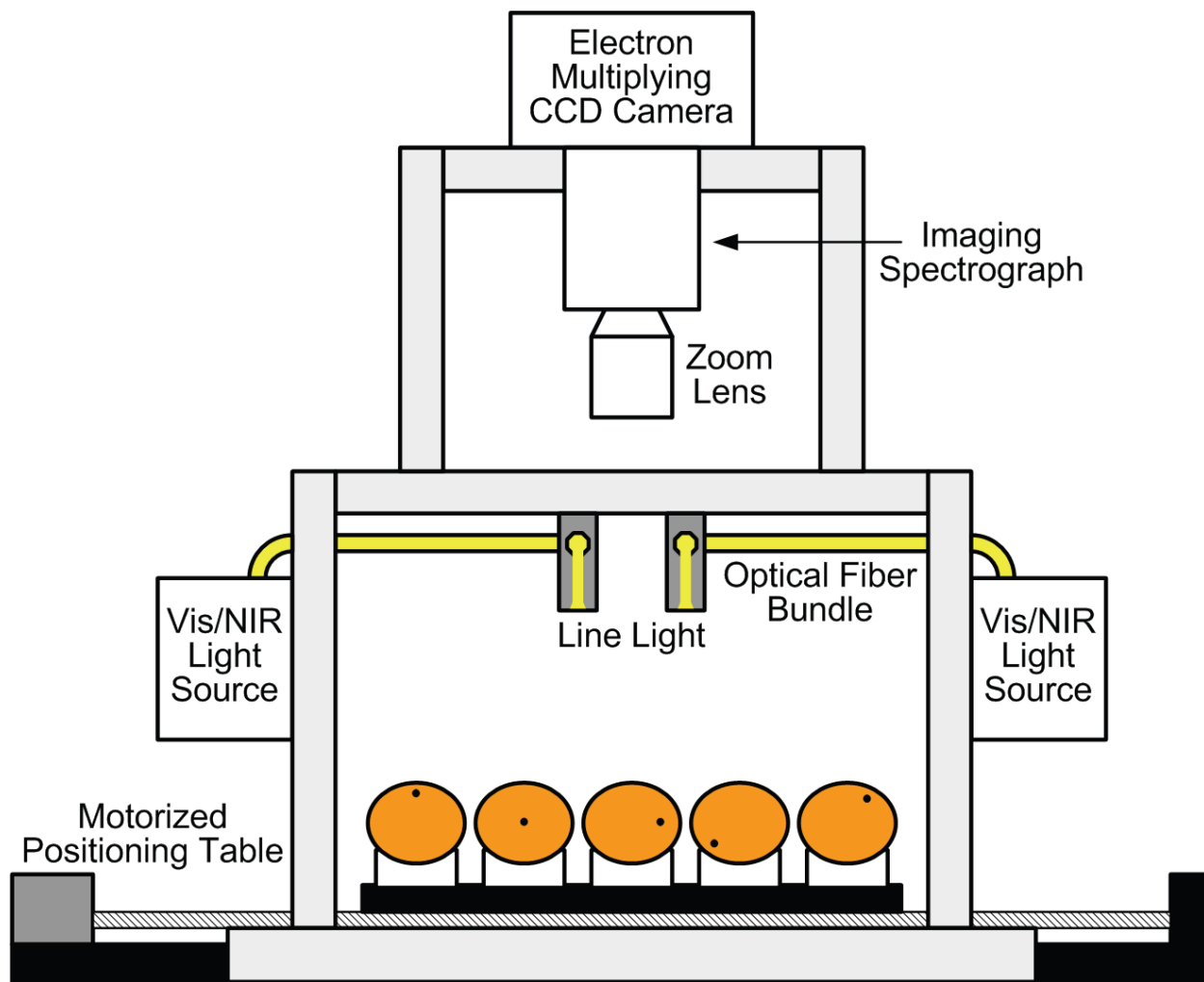


Figure 7-1: Hyperspectral imaging system for reflectance image acquisition from grapefruits

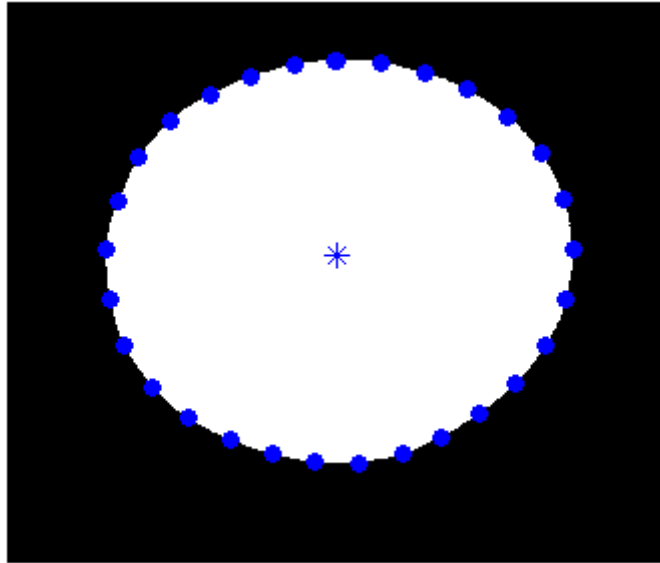


Figure 7-2: Pilot points and center of mass

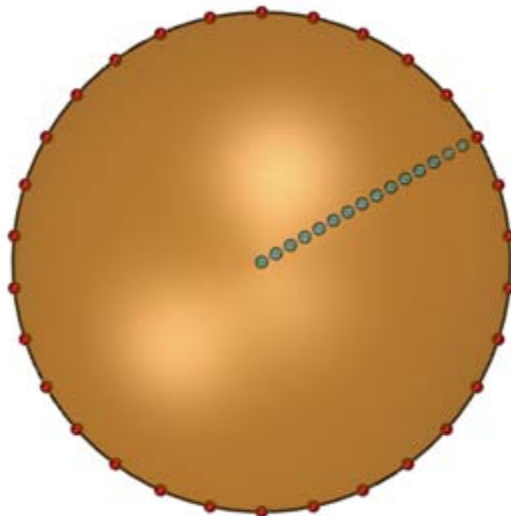


Figure 7-3: Pilot points (red in color) and nodes of interpolation (green in color) of one of the meridians

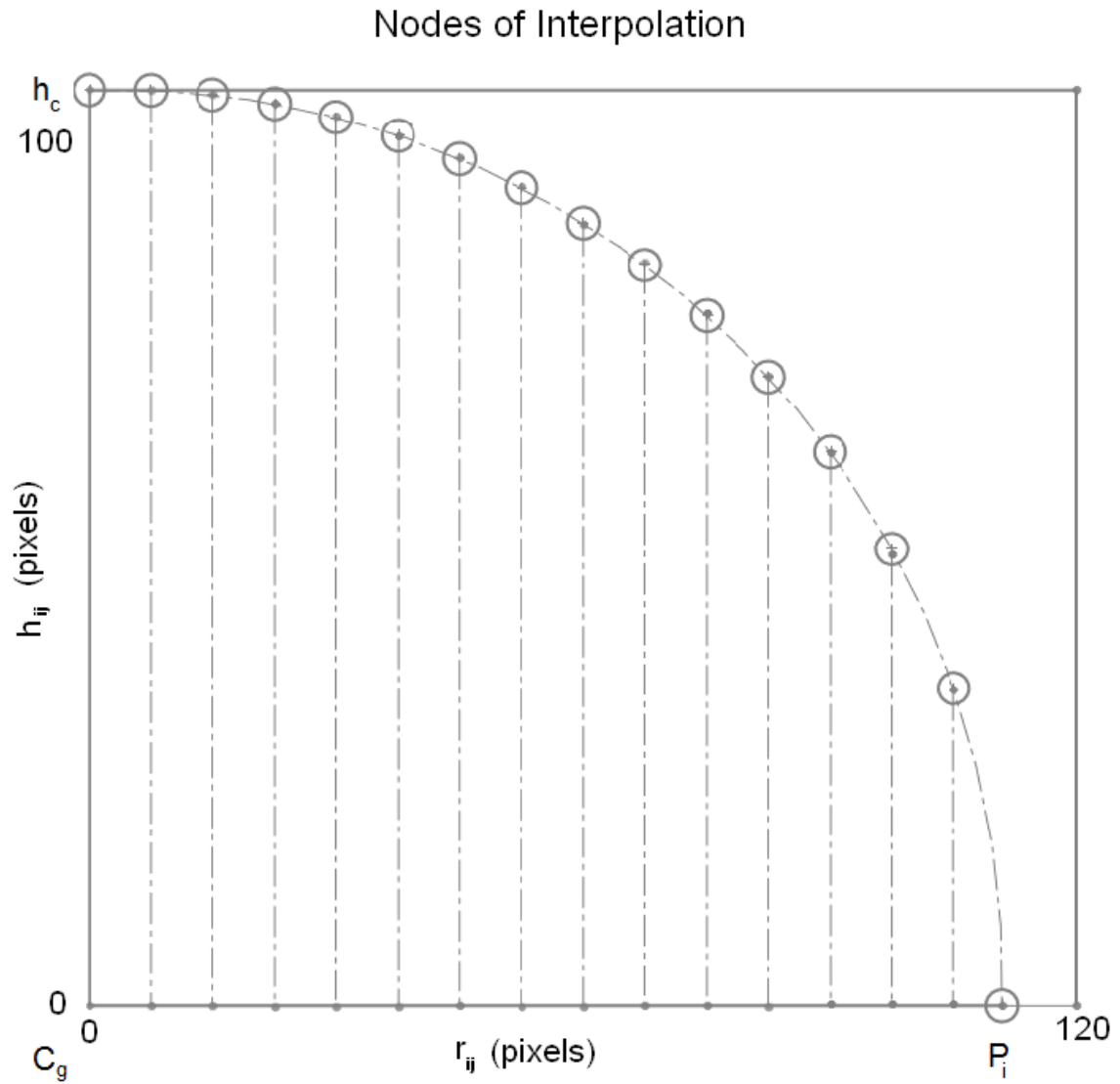


Figure 7-4: Transversal plane formed by maximum fruit height (h_c) and center of mass of the fruit (C_g). The computed elevations of the interpolation nodes is also shown by 'center line'

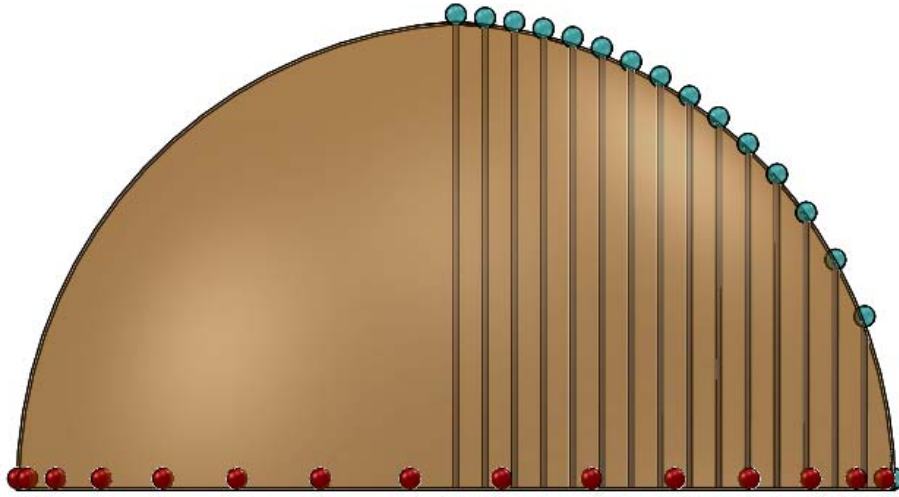


Figure 7-5: Side view of the modeled ellipse and the elevations of interpolation nodes

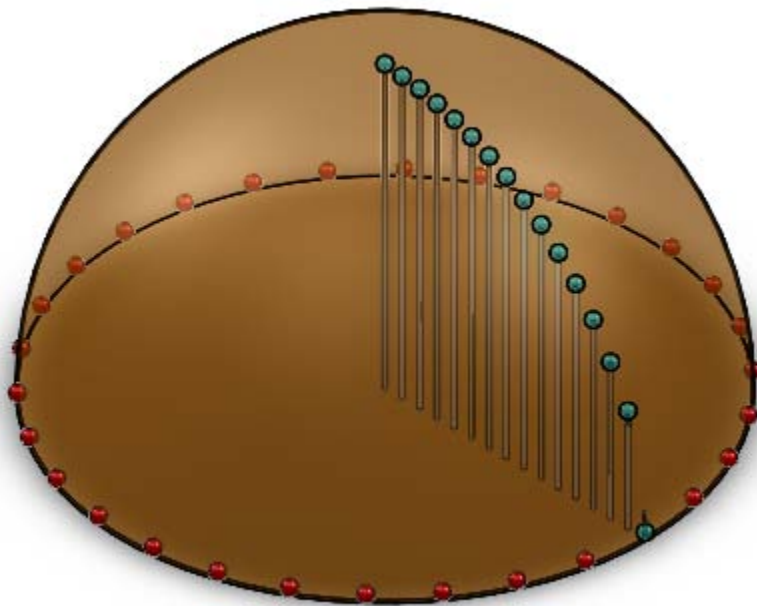


Figure 7-6: 3-D view of the modeled ellipse and the elevations of interpolation nodes

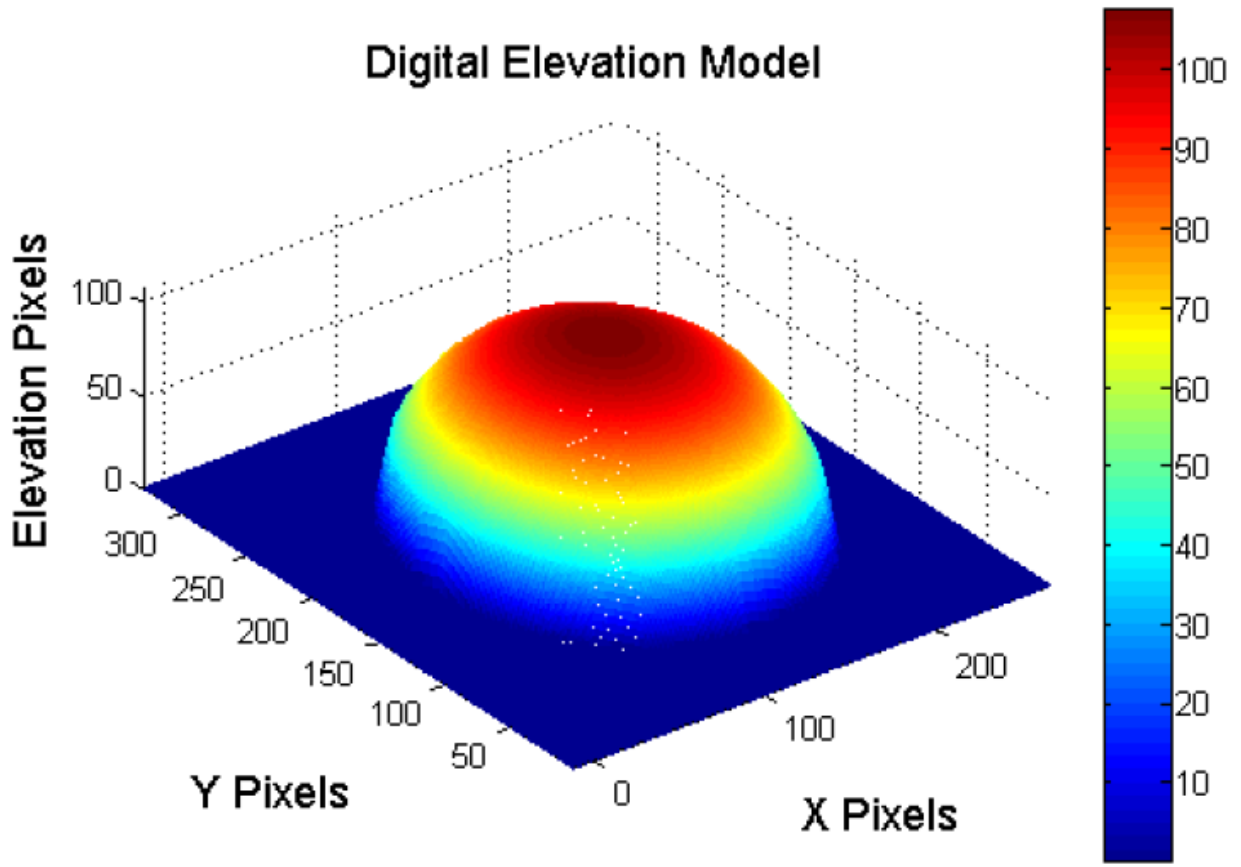


Figure 7-7: Digital elevation model

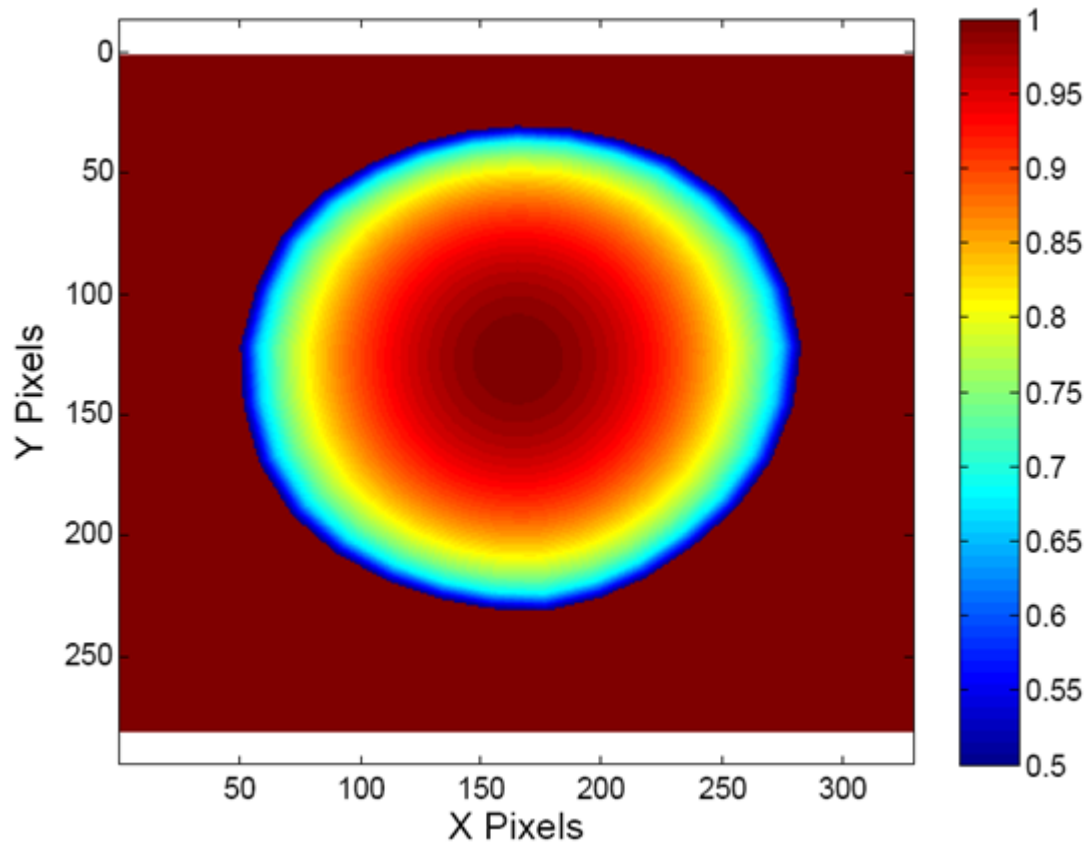


Figure 7-8: Contour of geometric correction factor (ϵ_g)

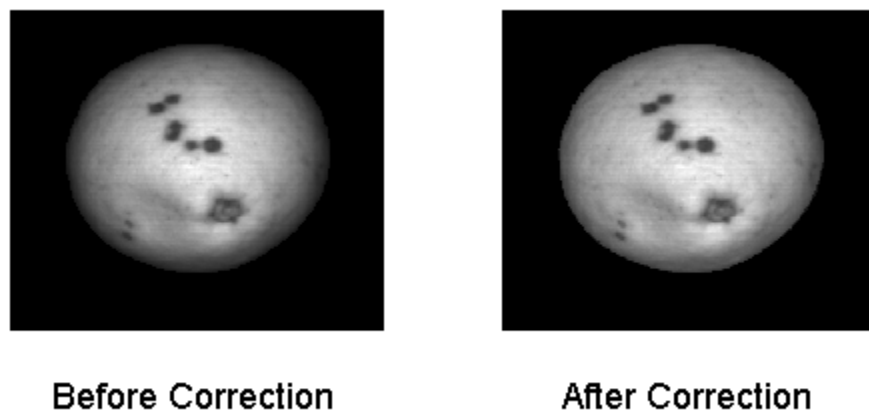
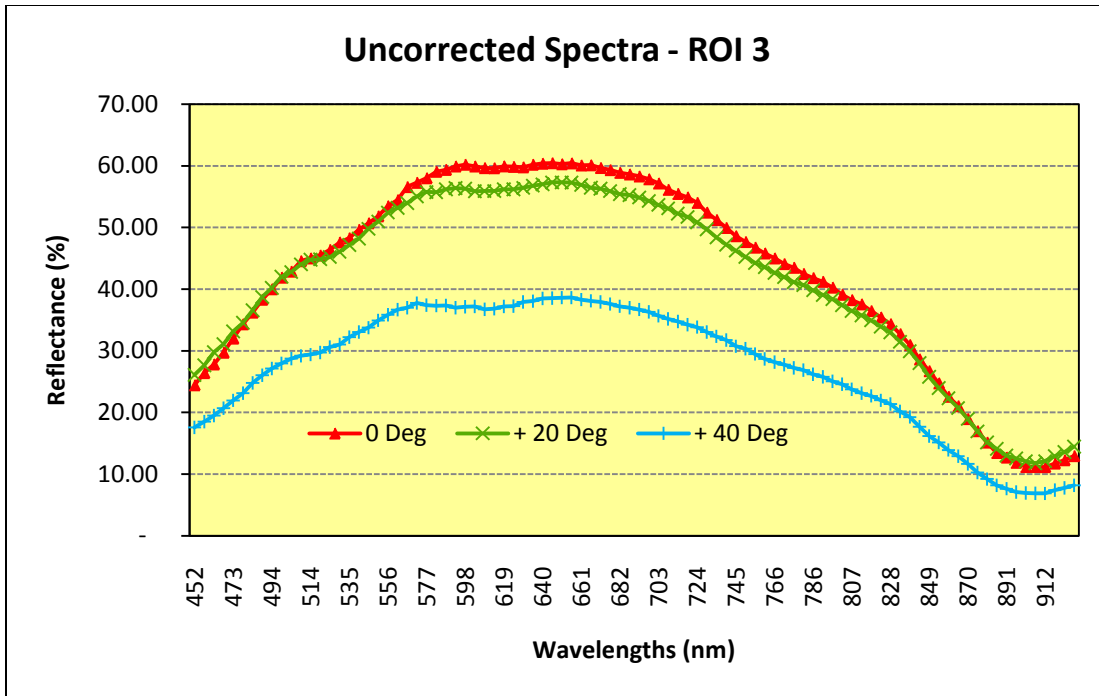


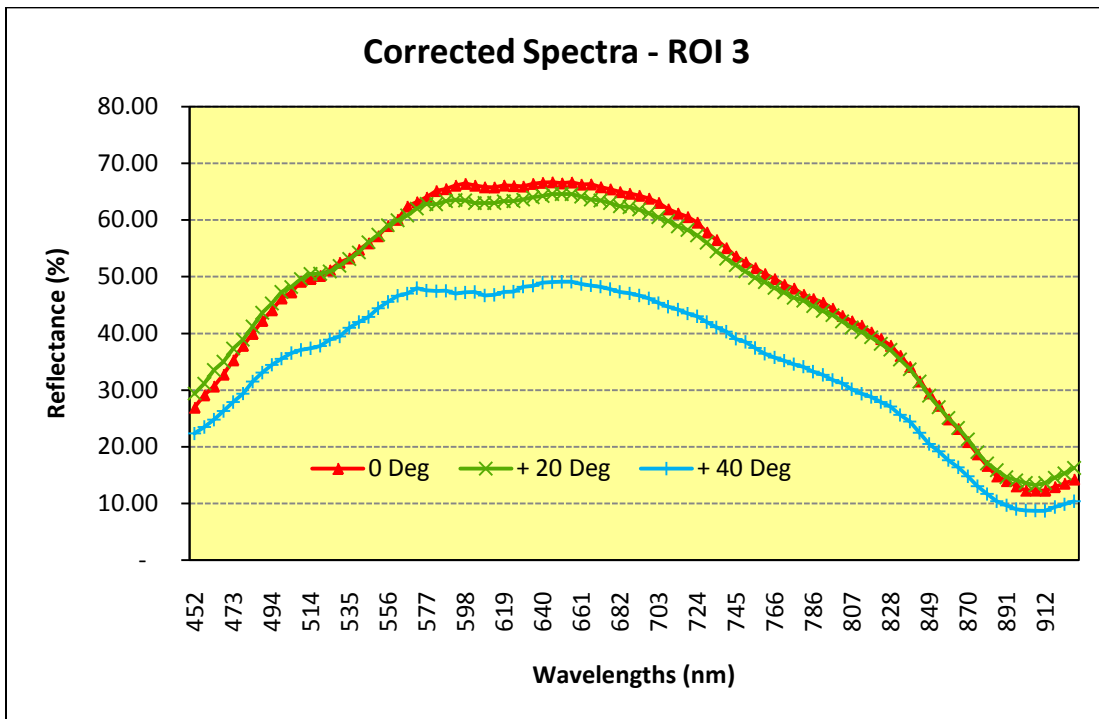
Figure 7-9: Effect of application of geometric correction – Single band image at 724 nm



Figure 7-10: Citrus sample marked with the angular graduations and the regions of interest

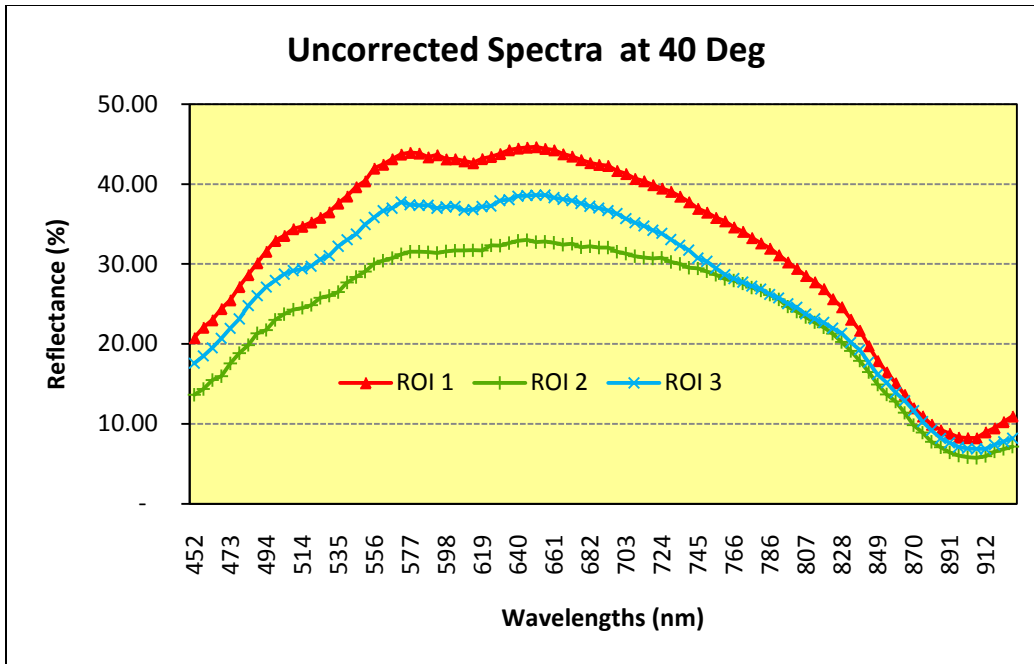


(A)

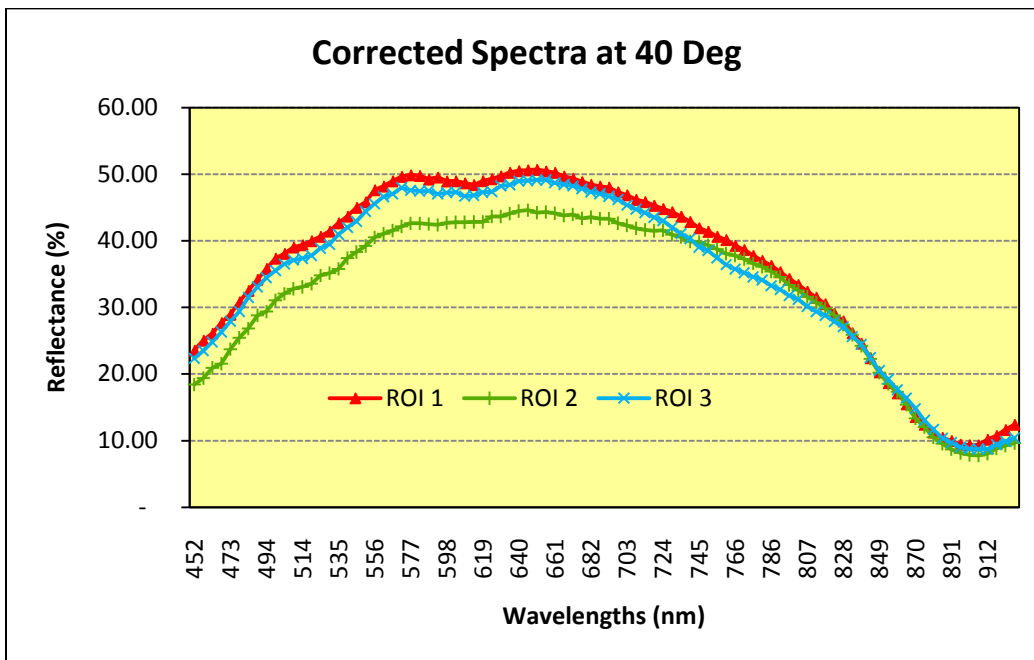


(B)

Figure 7-11: Reflectance spectra of ROI 3 (A) Before applying correction (B) After applying correction



(A)



(B)

Figure 7-12: Reflectance spectra of all three ROIs at the rotation of 40 degrees (A) Before applying correction (B) After applying correction

CHAPTER 8 OVERALL SUMMARY, CONCLUSIONS AND FUTURE SCOPE

Summary and Conclusions

Being the second largest industry in Florida, the citrus industry represents an 8.7 billion dollars industry employing tens of thousands of employees in various related jobs. Citrus industry has become a backbone of the economy of the State of Florida during the last century. However citrus canker is one of the biggest challenges the industry is facing right now as it is affecting the export of citrus fruits to several international markets including the European countries. The State has taken considerable amount of measures to stop the spread of the disease. The basic underlying objective of this thesis was to develop an approach for canker detection on the packaging line. Three different types of studies were conducted during the course of this research.

The first study was aimed at estimating the capability of the previously developed multispectral algorithm using correlation analysis to detect smallest possible canker lesion on the citrus fruit. More specifically the goal of this work was to determine the size of the smallest canker lesion that can be detected. The optimal wavelengths selected using correlation analysis were 834 nm and 729 nm. The best overall classification accuracy achieved was 95.7% when the binary threshold value of 1.275 was used. This threshold value was found to give best tradeoff between canker classification and overall classification. The smallest lesion detected by the lesion size estimation algorithm had the surface area of 2.16 sq. mm. and equivalent diameter was 1.66 mm.

The second part of the thesis consisted of an attempt to develop a novel approach to discriminate citrus canker from other surface conditions. The idea was to explore if a two camera system with one CCD color camera (to capture RGB color image) and one monochrome camera (to capture NIR single band image) could be built for canker detection in online real time packaging application. As this was an experimental study, the RGB color image was simulated from the single band images in the visible range (450-700 nm) from the previously captured hyperspectral data. The red, green and blue channels of the RGB image were then concatenated with remaining single band images from the hyperspectral data (700-930 nm) to generate the image for analysis. This image was then subjected to the correlation analysis (CA) to identify the key channels. The CA did not select any of the red, green or blue channels as a significant channel for canker identification. The reason being higher bandwidths of the R, G and B channels which not only might have included the information to detect canker but also other peel conditions. It was concluded that RGB color image (along with some single band monochrome image) cannot be utilized to discriminate canker from other peel conditions based on simple thresholding technique.

The third and final piece of the thesis was to re-implement the compensation algorithm to eliminate the adverse effects of light source while capturing the image of spherical objects like citrus fruits. The motivation behind this study was to reduce the misclassification of citrus fruits due to the edge blackening effect which our research team had been facing. The algorithm was developed by Gomez et al. 2007. The image was corrected for the spatial variations caused by intensity of light source as well as geometrical variation caused by the spherical geometry of the citrus fruit. The spatial

correction which commonly known as “flat field correction” was achieved with the help of a white panel of known reflectance. The geometric correction was accomplished by constructing a 3-D digital elevation model (DEM) of the fruit from its 2-D image. This DEM provided us with the geometric properties of the fruit like X, Y, and Z coordinates which were exploited in the course of estimating the geometric correction factor for each pixel. The corrected image portrayed improved and uniform brightness of the citrus fruit surface throughout. Few tests were also conducted to validate the results of the algorithm.

Future Scope

The basic limitation of all the three explorations was all of them were developed for the laboratory based study. The most important future step would be to adapt these algorithms for rapid real time online packaging applications. The RGB + NIR images were subjected to simple binary threshold based classification approach. The prospective work might include some texture based studies for canker discrimination. Also if such texture based algorithm works the next challenge would be to tune the algorithm for processing the citrus fruits for canker detection in the real time applications.

The edge effect compensation algorithm seemed to work absolutely fine during these laboratory based studies. However it was observed that the algorithm takes quite some time to process the 3-D hyperspectral image data of high resolution. Also each fruit had to be treated separately during the geometric correction estimation process. So the basic challenge is to minimize the processing time of the algorithm. Also the future work might include processing more than one fruit at a time. The algorithm will be fine

tuned and implemented on the packaging conveyor available with the research team to demonstrate its applicability for the real time applications.

APPENDIX A

MATLAB CODE FILES - ESTIMATION OF DETECTION LIMIT FOR SIZE OF CITRUS CANKER LESIONS BASED ON HYPERSPECTRAL REFLECTANCE IMAGING

```
%% Program to compute the Number of pixels in the smallest canker lesion
%% and to find the (X, Y) coordinates of the center of that lesion
```

```
clear all;
clc;
close all;
```

```
K = 0.6; % mm/pixel (pixel resolution)
a = K^2; % area of one pixel
n = 1;
```

```
%% Finding the Number of Pixels in smallest canker lesion
```

```
% org_img = Final Binary image obtained during the Image Classification
method
```

```
org_img = imread('fruit30_final_binary.tif');
level = graythresh(org_img);
org_img_binary = im2bw(org_img, level);
```

```
for i = 1:200
    post_img = bwareaopen(org_img, n);
    if (max(max(abs(post_img - org_img_binary))))==0
        n= n+1;
    elseif (max(max(abs(post_img - org_img_binary))))==1
        break
    end
```

```
    % The Equivalent area of the lesion :
    A = (n-1) * a;
    % disp('Sq mm');
```

```
end
```

```
% subplot(2,1,1); imshow(org_img_binary);
```

```
% subplot(2,1,2); imshow(post_img);
```

```
% Number of Pixels in smallest lesion
```

```
N = n-1
A;
```

```
%% Finding the Coordinates of the center of the smallest lesion
```

```
L = bwlabeln(org_img);
[L_row, L_col] = size(L);
```

```
area = regionprops(L, org_img, 'Area');
ctr = regionprops(L, org_img, 'Centroid');
```

```
z = [];
ctr_smallest = [];
for i = 1:length(area)
```

```
    if (area(i).Area) < n
        z = [z, i];
        ctr_smallest = [ctr_smallest; ctr(i).Centroid];
    end
end

ctr_smallest

%% End
```

APPENDIX B
MATLAB CODE FILES - DETECTION OF CITRUS CANCKER USING RGB COLOR
IMAGE ALONG WITH NIR MONOCHROME IMAGES

Main Program File

Simulation of the RGB + NIR images

```
clear all;
clc;
close all;

% Loading the Input file
address = 'C:\Nikhil\Nikhil_Office Comp Back up (Jan 5 2010)\1
Nikhil\Research\Hyper Demo for Duke\10 samples of each
condition\Norm_R_RG_SB_SC_002';

[image_hyper,p,t] = hsi_read (address);
[row, col, band] = size(image_hyper);

%% Building the R, G, B Filters and Creating the Filtered Red, Green & Blue
channel images

% 1} Green (G) Filter

x1 = sort([603.3800 598.1500 592.9200 587.6800 582.4500 577.2200
571.9900 566.7600 561.5300 556.3000 551.0700 545.8400 540.6000 535.3700
530.1400 524.9100 519.6800 514.4500 509.2200 503.9900 498.7500]);

avg1 = 550;
std_dev1 = sqrt(1/(length(x1)-1)*sum((x1 - avg1).^2));

% "y1" = Green Filter (Gussian Approximation)
y1 = (1/(sqrt(2*pi*std_dev1^2))) * (exp(-((x1 - avg1).^2)/(2*std_dev1^2)));

% Normalizing y1 to have its values between 0 to 1
y1 = y1*80;

% Applying the Filter
m1 = length(x1);
for i = 1:m1
    T = image_hyper(:, :, (m1-i+1)); % T = Image at perticular wavelength
    g = T.*y1(i);
    % Adding the Filtered images at each wavelength to the 3rd dimension to
    % create "green" channel
    gr(:, :, i) = g;
end

% Averaging the Green channel to create a grayscale (green) image
green = sum(gr,3)/length(x1);

% 2} Blue (B) Filter

w = [];
```

```

z = 451.67-5.23;
for l=1:200
    if z <= 400
        break;
    else z=z-5.23;
        w = [w, z];
    end
end

x2 = sort([503.9900 498.7500 493.5200 488.2900 483.0600 477.8300 472.6000
467.3700 462.1400 456.9100 451.6700 w]);

avg2 = 450;
std_dev2 = sqrt(1/(length(x2)-1)*sum((x2 - avg2).^2));

% "y2" = Blue Filter (Gussian Approximation)
y2 = (1/(std_dev2*sqrt(2*pi))) * (exp(-((x2 - avg2).^2)/(2*std_dev2^2)));

% Normalizing y2 to have its values between 0 to 1
y2 = y2*81;

% Applying the Filter
m2 = (length(x2)-length(w));
for j = 1:m2
    T2 = image_hyper(:, :, (m2-j+1)); % T = Image at perticular wavelength
    b = T2.*y2(j+length(w)-1);
    % Adding the Filtered images at each wavelength to the 3rd dimension to
    % create "blue" channel
    b1(:, :, j) = b;
end

% Averaging the Blue channel to create a grayscale (blue) image
blue = sum(b1,3)/length(x2);

% 3} Red (R) Filter

x3 = sort([702.7700 697.5400 692.3100 687.0800 681.8500 676.6100 671.3800
666.1500 660.9200 655.6900 650.4600 645.2300 640.0000 634.7700 629.5300
624.3000 619.0700 613.8400 608.6100 603.3800 598.1500]);

avg3 = 650;
std_dev3 = sqrt(1/(length(x3)-1)*sum((x3 - avg3).^2));

% "y3" = Red Filter (Gussian Approximation)
y3 = (1/(sqrt(2*pi*std_dev3^2))) * (exp(-((x3 - avg3).^2)/(2*std_dev3^2)));

% Normalizing y3 to have its values between 0 to 1
y3 = y3*80;

% Applying the Filter
m3 = length(x3);
for k = 1:m3
    T = image_hyper(:, :, (m3-k+1)); % T = Image at perticular wavelength
    r = T.*y1(k);
    % Adding the Filtered images at each wavelength to the 3rd dimension to
    % create "red" channel

```

```

    re(:, :, k) = r;
end

% Averaging the Red channel to create a grayscale (red) image
red = sum(re,3)/length(x3);

% % Displaying Red, Green & Blue grayscale images side by side

% figure;
% subplot(1,3,1); imshow(mat2gray(red));
% subplot(1,3,2); imshow(mat2gray(green));
% subplot(1,3,3); imshow(mat2gray(blue));

% Combining Red, Green & Blue grayscale images to create RGB color image
color = cat(3, 0.4*red, 0.5* green, 0.1*blue);
% figure;
% imshow(mat2gray(color));

% % Plotting the R, G, B filter Characteristics
figure;
plot(x1,y1, '--g','LineWidth',2);
grid on; hold on;
plot(x2,y2, '--b','LineWidth',2);
hold on;
plot(x3,y3, '--r','LineWidth',2);

band17 = image_hyper(:, :, 17);
band39 = image_hyper(:, :, 39);

% % Combining the RGB color image with the remaining NIR single band images

% S is an array containing all the images (concatenated in the 3rd
dimension) to be considered for Correlation Analysis
S = cat(3, color, image_hyper(:, :, 1:43));
S = single(S);
hsi_write(S,'RGB_NIR_SB_002.img');

% % End

```

Generation of Spectra of Different Disease Conditions

```

clear all;
clc;
close all;

% % Generation of CK and Non-CK spectra

% Loading all the Spectra files in ASCII format
load('RGB_NIR_CK_Spectra_001.txt');
load('RGB_NIR_CK_Spectra_002.txt');
load('RGB_NIR_GS_Spectra_001.txt');
load('RGB_NIR_GS_Spectra_002.txt');
load('RGB_NIR_ID_Spectra_001.txt');
load('RGB_NIR_ID_Spectra_002.txt');

```

```

load('RGB_NIR_MK_Spectra_001.txt');
load('RGB_NIR_MK_Spectra_002.txt');
load('RGB_NIR_MN_Spectra_001.txt');
load('RGB_NIR_MN_Spectra_002.txt');
load('RGB_NIR_SB_Spectra_001.txt');
load('RGB_NIR_SB_Spectra_002.txt');
load('RGB_NIR_WS_Spectra_001.txt');
load('RGB_NIR_WS_Spectra_002.txt');

spectra_ck = [RGB_NIR_CK_Spectra_001(:, 2:6), RGB_NIR_CK_Spectra_002(:,
2:6)];
spectra_ck = spectra_ck';
spectra_nck = [RGB_NIR_GS_Spectra_001(:, 2:6), RGB_NIR_GS_Spectra_002(:,
2:6), RGB_NIR_ID_Spectra_001(:, 2:6), RGB_NIR_ID_Spectra_002(:, 2:6),
RGB_NIR_MK_Spectra_001(:, 2:6), RGB_NIR_MK_Spectra_002(:, 2:6),
RGB_NIR_MN_Spectra_001(:, 2:6), RGB_NIR_MN_Spectra_002(:, 2:6),
RGB_NIR_SB_Spectra_001(:, 2:6), RGB_NIR_SB_Spectra_002(:, 2:6),
RGB_NIR_WS_Spectra_001(:, 2:6), RGB_NIR_WS_Spectra_002(:, 2:6)];
spectra_nck = spectra_nck';
a =
[927.71,922.48,917.25,912.02,906.79,901.55,896.32,891.09,885.86,880.63,875.40
,870.17,864.94,859.70,854.47,849.24,844.01,838.78,833.55,828.32,823.09,817.86
,812.62,807.39,802.16,796.93,791.70,786.47,781.24,776.01,770.78,765.54,760.31
,755.08,749.85,744.62,739.39,734.16,728.93,723.69,718.46,713.23,708];
wl = [943.4, 938.17, 932.94, a];

% Saving the Spectra files in MATLAB format
save('data_ca_spectra_ck_nck.mat', 'spectra_ck', 'spectra_nck', 'wl');

%% End

```

Function Files

Function to Perform the Correlation Analysis on the Image Data

```

function hsi_ca
% calculate the correlation coefficient between a spectral wavelength pair
combination and the disease condition (0=normal, 1=defect).

% Reference: Correlation analysis of hyperspectral imagery for multispectral
wavelength selection for detection of defects on apples,
% Sens. & Instrumen. Food Qual. (2008) 2:90-96

load data_ca_spectra_ck_nck;

band = 1:46;
num_band = size(band,2); % wavelength
num_sample1 = size(spectra_ck,1); % canker
num_sample2 = size(spectra_nck,1); % non-canker

% wavelength ratios
ratio_spectra_ck = zeros(num_band,num_band,num_sample1); % 2-band selection
ratio_spectra_nck = zeros(num_band,num_band,num_sample2);

```

```

for k = 1:num_sample1
    for i = 1:num_band
        for j = 1:num_band
            ratio_spectra_ck(i,j,k) = spectra_ck(k,i)/spectra_ck(k,j); % 2-
band selection, I1/I2
        end
    end
end

for k = 1:num_sample2
    for i = 1:num_band
        for j = 1:num_band
            ratio_spectra_nck(i,j,k) = spectra_nck(k,i)/spectra_nck(k,j);% 2-
band selection, I1/I2
        end
    end
end

index = [ones(1,num_sample1) zeros(1,num_sample2)]; % disease condition
(0=normal, 1=defect)

A = zeros(1, num_sample1);
B = zeros(1, num_sample2);
corr_ratio = zeros(num_band,num_band);

for i = 1:num_band
    for j = 1:num_band
        for k1 = 1:num_sample1
            A(k1) = ratio_spectra_ck(i,j,k1);%2-band selection
        end
        for k2 = 1:num_sample2
            B(k2) = ratio_spectra_nck(i,j,k2);%2-band selection
        end
        corr_matrix = corrcoef([A B],index);
        corr_ratio(i,j) = corr_matrix(1,2);
    end
end

% save corr_coeff_2_band corr_ratio

figure;
axes('FontSize',14);
contourf(wl,wl,corr_ratio);
% contourf(band,band,corr_ratio)
colorbar ('FontSize',14);
axis equal
axis tight
title('Contour of Correlation Coefficients', 'FontSize',16);
xlabel('Wavelengths (nm)', 'FontSize',16);
ylabel('Wavelengths (nm)', 'FontSize',16);
[V1 L1] = max(corr_ratio);
[V1 L1] = max(abs(corr_ratio));
[ratio_max column1] = max(V1);
row1 = L1(column1);

```

```

ratio_max
band1 = row1
band2 = column1
%% End

```

Function to Read the Image File in ENVI Format in MATLAB

```

function [image_hyper,p,t] = hsi_read (fname)
% Reads an image of ENVI standard type to a [col x line x band] MATLAB array

% SYNTAX
% image_hyper=hsi_read(fname)
% [image_hyper,p]=hsi_read(fname)
% [image_hyper,p,t]=hsi_read(fname)
%
% INPUT :
% fname string giving the full pathname of the ENVI image to read.
%
% OUTPUT :
% image_hyper: c by l by b array containing the ENVI image values organised
in c : cols, l : lines and b : bands.
% p: 1 by 3 vector that contains (1) the number of cols, (2) the number of
lines and (3) the number of bands of the opened image.
%
% t: string describing the image data type string in MATLAB conventions.
%
% NOTE :
% hsi_read needs the corresponding image header file generated
% automatically by ENVI. The ENVI header file must have the same name as
% the ENVI image file + the '.hdr' exention.

tic;

% Parameters initialization
elements={'samples ' 'lines ' 'bands ' 'data type '};
d={'bit8' 'int16' 'int32' 'float32' 'float64' 'uint16' 'uint32' 'int64'
'uint64'};

% Check user input
if ~ischar(fname)
    error('fname should be a char string');
end

% Open ENVI header file to retrieve s, l, b & d variables
rfid = fopen(strcat(fname, '.hdr'), 'r');

% Check if the header file is correctly open
if rfid == -1
    error('Input header file does not exist');
end;

% Read ENVI image header file and get p(1) : number of samples,
% p(2) : number of lines, p(3) : number of bands and t : data type
while 1
    tline = fgetl(rfid);

```

```

if ~ischar(tline), break, end
[first,second]=strtok(tline,'=');

switch first
    case elements(1)
        [f,s]=strtok(second);
        p(1)=str2num(s);
    case elements(2)
        [f,s]=strtok(second);
        p(2)=str2num(s);
    case elements(3)
        [f,s]=strtok(second);
        p(3)=str2num(s);
    case elements(4)
        [f,s]=strtok(second);
        t=str2num(s);
        switch t
            case 1
                t=d(1);
            case 2
                t=d(2);
            case 3
                t=d(3);
            case 4
                t=d(4);
            case 5
                t=d(5);
            case 12
                t=d(6);
            case 13
                t=d(7);
            case 14
                t=d(8);
            case 15
                t=d(9);
            otherwise
                error('Unknown image data type');
        end
    end
end
end
fclose(rfid);
t=t{1,1};

% Open the ENVI image and store it in the 'image' MATLAB array
disp(['Reading ',(num2str(p(1))),(' cols x '), (num2str(p(2))),(' lines x '),
(num2str(p(3))),(' bands') (' of type '), (t), (' hyperspectral image...')]);
fid=fopen(strcat(fname, '.img'));
image_hyper_array=fread(fid,t);
image_hyper=reshape(image_hyper_array,[p(1),p(3),p(2)]);
image_hyper=permute(image_hyper, [3 1 2]);
fclose(fid);
Time_Used_In_Minute = round (toc/60)
%% End

```

Function to Write the MATLAB Array into an Image File in ENVI Format

```
function i=hsi_write(image,fname)

% Write a MATLAB array to a file in ENVI standard format from a [col x line x
band] array
%
% SYNTAX
%
% hsi_write(image, fname)
%
% INPUT :
%
%
% image c by l by b name of the MATLAB variable containing the array to
export to an ENVI image, with c = cols, l the lines and b the bands
% fname string full pathname of the ENVI image to write.

% Parameters initialization
im_size=size(image);
im_size(3)=size(image,3);
elements={'samples =' 'lines   =' 'bands   =' 'data type ='};
d=[4 1 2 3 12 13];
% Check user input
if ~ischar(fname)
    error('fname should be a char string');
end

cl1=class(image);

% if cl1 == 'double'
%     img=single(image);
% else
%     img=image;
% end

img=image;

cl=class(img);
switch cl
    case 'single'
        t = d(1);
    case 'int8'
        t = d(2);
    case 'int16'
        t = d(3);
    case 'int32'
        t = d(4);
    case 'uint16'
        t = d(6);
    case 'uint32'
        t = d(7);
    otherwise
        error('Data type not recognized');
end
```

```

wfid = fopen(fname, 'w');
if wfid == -1
    i=-1;
end
% disp(['Writing ENVI image ...']);
fwrite(wfid, img, cl);
fclose(wfid);

% Write header file

fid = fopen(strcat(fname, '.HDR'), 'w');
if fid == -1
    i=-1;
end

fprintf(fid, '%s \n', 'ENVI');
fprintf(fid, '%s \n', 'description = {');
fprintf(fid, '%s \n', 'Exported from MATLAB}');
fprintf(fid, '%s %i \n', elements{1,1}, im_size(1));
fprintf(fid, '%s %i \n', elements{1,2}, im_size(2));
fprintf(fid, '%s %i \n', elements{1,3}, im_size(3));
fprintf(fid, '%s %i \n', elements{1,4}, t);
fprintf(fid, '%s \n', 'interleave = bsq');
fclose(fid);
%% End

```

APPENDIX C
MATLAB CODE FILES - COMPENSATION OF EDGE EFFECT ON IMAGES OF
SPHERICAL OBJECTS DUE TO LIGHT SOURCE

Main Program File

```
clear all;
clc;
close all;

% Loading the Input file
load('C:\Nikhil\Nikhil_Office Comp Back up (Jan 5 2010)\Research\Edge effect
compensation-final folder\data_hyper_citrus_canker_original.mat');%%

mask1 = extract_mask ('data_hyper_citrus_canker_original',
'data_dark_white_reference');

[mask1_row, mask1_col] = size(mask1);

%% Obtaining all the pixels (xy) on the Edge of the mask
mask_edge = double(edge(mask1));
np = 30; % np = Number of points to be selected on the Periphery of the mask
xy = [];
n = 0;

for i=1:mask1_row
    for j=1:mask1_col
        if mask_edge(i,j) == 1
            n=n+1;
            xy = [xy [i j]'];
        end
    end
end
xy = xy';
[xy_row, xy_col] = size(xy);

cp = mean(xy);

%% Obtaining the array of "np" number of equidistant Pilot points on the
periphery of the mask

xy = xy - ones(size(xy,1),1)*cp; % Transforming all points to the origin
np_xy = [];
step = 2*pi/(np-1);
for th = -pi : step : pi,
    for i=size(xy,1):-1:1, %disp([th i])
        nn = abs(th - atan2(xy(i,2),xy(i,1)));
        if nn<.009
            np_xy = [np_xy; xy(i,:)];
            xy(i,:)=[];
            break
        end
    end
end
end
```

```

np_xy1 = np_xy + ones(size(np_xy,1),1)*cp;

%% Obtaining the Center of mass (cg) of the mask
cg = (1/np) * sum(np_xy);
cg1 = (1/np) * sum(np_xy1);

% Plotting the center of mass & Pilot Points on the edge of mask
figure;
imshow(mask1); hold on;
axis equal;
plot(np_xy1(:,2),np_xy1(:,1),'o', 'MarkerFaceColor','b','MarkerSize',7);
hold on;
plot(cg1(:,2),cg1(:,1),'*', 'MarkerSize',10);
title('Pilot Points and the Center of mass', 'FontSize',12);

%% Obtaining the Maximum height of the fruit & the Elevations of the
Interpolation network
num = 16; % num = Number of points to be considered on each Radius.
beta = 1; % beta = Flattening factor
sum1 = 0;
radmat = [];
hij = [];

for i = 1: size(np_xy)
    rad = norm(np_xy(i,:) - cg);
    radmat = [radmat; rad];
    sum1 = sum1 + rad;
end

% Obtaining Maximum height (hc) of fruit
hc = (1/np) * beta * sum1;

% Obtaining the X, Y & Z coordinates of the Nodes of interpolation
for m = 1 : size(np_xy)
    dm = radmat(m);
    d = np_xy(m, :);
    theta = atan2(d(2), d(1));
    xyz = [];
    for rij = 0 : (dm/(num - 1)) : dm
        x = rij * cos(theta);
        y = rij * sin(theta);
        h = sqrt((1-(rij/dm)^2)*hc^2);
        xyz = [xyz; [x y h]];
    end
    xyz_mat{m} = xyz;
end

xyz_mat1 = xyz_mat';
xyz_cat = [];
for i = 1:(length(xyz_mat1))
    xyz_cat = vertcat(xyz_cat, xyz_mat1{i});
end

%% Obtaining the Heights for all the pixels by interpolation (Z value for
each of the in between pixel)

```

```

tix = -139.5:1:139.5; tiy = -164:1:164; %%%%%%
[XI,YI] = meshgrid(tix,tiy);
ZI = griddata(xyz_cat(:,1),xyz_cat(:,2),xyz_cat(:,3),XI,YI);

for i=1:length(ZI(:)), if isnan(ZI(i)), ZI(i)=0; end; end

% Displaying the Digital Elevation Model (DEM)
figure;
mesh(XI,YI,ZI)
colorbar;
axis equal;
title('Digital Elevation Model', 'FontSize',13);
xlabel('X Pixels', 'FontSize',13); ylabel('Y Pixels', 'FontSize',13);
zlabel('Elevation Pixels', 'FontSize',13);
% axes('FontSize',14);
colorbar ('FontSize',13);

% Obtaining the X, Y, & Z for all the image pixels in a Single column.
x_all = [];
y_all = [];
z_all = [];
xyz_all= [];

for i = 1 : (size(YI,1))
    for j = 1 : (size(XI,2))
        x_all = [x_all; XI(1,j)];
        y_all = [y_all; YI(i,1)];
        z = ZI(i,j);
        if isnan(z)
            z = 0;
        end;
        z_all = [z_all; z];
    end
end
xyz_all = [x_all, y_all, z_all];

%% Calculation of Geometric Correction Factor (epci)
alphaD = 0.5104; % Mean value of alphaD
fi_all = [];
epci_all1 = [];

% Calculation of Angle of Incidence
for i=1:(size(xyz_all,1))
    x = xyz_all(i,1);
    y = xyz_all(i,2);
    z = xyz_all(i,3);

    if z == 0
        epci = 1;
        epci_all1 = [epci_all1; epci];
    elseif z ~= 0
        temp = (sqrt((x^2) + (y^2))) / z;
        fi = atan(temp);
        fi_all = [fi_all; fi];
    end
end

```

```

        % Calculation of gemetric correction factor
        epci = (alphaD * cos(fi)) + (1 - alphaD);
        epci_all1 = [epci_all1; epci];
    end
end

% Reshaping the matrix "epci_all" (Matrix of Geometric Correction factor for
all the pixels) to the Image dimensions.
epci_2d = reshape(epci_all1, mask1_row, mask1_col);
epci_edge = double(edge(epci_2d));
% figure; imshow(epci_edge);

%% Matching the contour of the Fruit image and contour of geometric
correction factor
C1 = conv2(mask_edge,epci_edge,'same');
%figure,surf(C1)
[val,I] = max(C1);
[val,I2] = max(val);
Xidx = I2;
Yidx = I(I2);

C2 = conv2(mask_edge,mask_edge,'same');
%figure,surf(C2)
[val,I] = max(C2);
[val,I2] = max(val);
Xidx2 = I2;
Yidx2 = I(I2);

Xshift = Xidx2 - Xidx;
Yshift = Yidx2 - Yidx;

% Shifting the contour of Geometric correction factor to match the Fruit
contour
epci_2d = circshift(epci_2d, [Yshift, Xshift]);

% Plotting the Contour of the geometric correction factor
figure;
imagesc(epci_2d); colorbar; colormap jet;
axis equal;
set(gca,'CLim', [0.5, 1.0]);
title('Contour of Geometric Correction Factor', 'FontSize',13);
xlabel('X Pixels','FontSize',13); ylabel('Y Pixels', 'FontSize',13);
colorbar;

% Applying the Geometric correction factor the the image
epci_all = reshape(epci_2d, mask1_row*mask1_col, 1);
a = size(R_sample, 1)*size(R_sample, 2);
for p = 1:size(R_sample,3)
    R_sample_masked(:,:,p) = R_sample(:,:,p) .* mask1;
    R_temp = reshape(R_sample_masked(:,:,p), a, 1);
    R_temp_corrected = R_temp ./ epci_all;
    R_sample_corrected(:,:,p) = reshape(R_temp_corrected, size(R_sample, 1),
size(R_sample, 2));
end

```

```

% Plotting the Fruit image (724 nm) before and after geometric correction
figure;
title('Effect of Geometric Correction', 'FontSize',13);
subplot(1,2,1);
imshow(mat2gray(R_sample_masked(:,:,40)));
xlabel('Before Correction', 'FontSize',13)
subplot(1,2,2);
imshow(mat2gray(R_sample_corrected(:,:,40)));
xlabel('After Correction', 'FontSize',13)

%% End

```

Function Files

```

%% Function to extract the mask of the fruit image

function [R_mask] = extract_mask (filename_sample, filename_reference)
% Generate mask for hyperspectral reflectance images
% Example: R_mask = extract_mask ('data_hyper_citrus_canker_original',
'data_dark_white_reference');

% Image normalization
load (filename_sample);
load (filename_reference);
band_mask = 42;
num_scan = size(R_sample, 1);
R_dark_mono = repmat(mean(R_dark(:,:,band_mask)), num_scan, 1);
R_white_mono = repmat(mean(R_white(:,:,band_mask)), num_scan, 1);
R_mask = uint16(10000*(R_sample(:,:,band_mask) - R_dark_mono)./(R_white_mono
- R_dark_mono));
clear R_sample R_dark R_white;

% Mask generation
level_mask = 0.005;
R_mask_original = double(R_mask);
R_mask = im2bw(R_mask, level_mask);
R_mask = bwareaopen(R_mask, 4000, 8);
R_mask = double(imfill(R_mask, 'holes'));
R_sample_masked = R_mask_original .* R_mask;

% % Plot result
% figure,
% subplot(2,3,1), imshow(R_mask_original, []); title ('Original Image',
'FontWeight', 'bold');
% subplot(2,3,2), imshow(R_mask, []); title ('Mask Template', 'FontWeight',
'bold');
% subplot(2,3,3), imshow(R_sample_masked, []); title ('Masked Imge',
'FontWeight', 'bold');
% subplot(2,3,4), plot([1:size(R_mask,1)], R_mask_original(:,
(size(R_mask,2)-1)/2), [1:size(R_mask,1)], R_sample_masked(:,
(size(R_mask,2)-1)/2), 'r');
% legend('Original','Masked'); title ('Y Profile', 'FontWeight', 'bold');
% subplot(2,3,[5 6]), plot([1:size(R_mask,2)],
R_mask_original(size(R_mask,1)/2, :), [1:size(R_mask,2)],
R_sample_masked(size(R_mask,1)/2, :), 'r');
% legend('Original','Masked'); title ('X Profile', 'FontWeight', 'bold');

```

```
% save (filename_sample, 'R_mask', '-append');  
%% End
```

LIST OF REFERENCES

- Aleixos, N., Blasco, J., Navarrón, F., Moltó, E., 2001. Multispectral inspection of citrus in real-time using machine vision and digital signal processors. *Computers and Electronics in Agriculture*. 33 (2002) 121–137.
- Bishop, C. M., 2006. "Pattern Recognition and Machine Learning". First Edition.
- Cheng, X., Chen, Y. R., Tao, Y., Wang, C. Y., Kim, M. S., Lefcourt, A. M., 2004. A novel integrated PCA and FLD method on hyperspectral image feature extraction for cucumber chilling damage inspection. *Information and Electrical Technologies Division of ASAE*. ISSN 0001–2351. Vol. 47(4): 1313–1320.
- Chen, Y. R., Chao, K., Kim, M. S., 2002. Machine vision technology for agricultural applications. *Computers and Electronics in Agriculture*. 36(2002) 173–191.
- Duda, R. O., Hart, P. E., Stork, D. G., 2004. "Pattern Classification". Second Edition.
- Das, A. K., 2003. Citrus canker – A review. *J. Appl. Hort.* 5(1): 52–60.
- Florida Statistics Site [Internet], USDA's National Agricultural Statistics Service (US); Update: 2007 June; Accessed on December 2009. Available at: http://www.nass.usda.gov/Statistics_by_State/Florida/Publications/Broc/index.asp
- Foley, J., Van Dam, S., Hughes, J., 1996. "Computer Graphics: Principles and Practice." Second Edition.
- Gómez-Sanchis, J., Moltó, E, Camps-Valls, G, Gómez-Chova, L, Aleixos, N, Blasco, J. Automatic correction of the effects of the light source on spherical objects. An application to the analysis of hyperspectral images of citrus fruits. *J. Food Eng* 85 (2008) 191–200.
- Gonzalez, R., Woods, R., Editions, S., 2004. "Digital image processing using MATLAB".
- Green, P., MacDonald, L., 2002. "Colour Engineering – Achieving Device Independent Color". First Edition.

- Hodge, A., E. Philippakos, D. Mulkey, T. Spreen, and R. Muraro. 2001. Economic impact of Florida's citrus industry, Extension Digital Information Source (EDIS) FE307. Gainesville, Fla.: University of Florida, Department of Food and Resource Economics, 1999–2000.
- James A. Jacobs. 1994. Cooperative in the U.S. Citrus Industry, Agricultural Economist, U.S. Department of Agriculture, Rural Business and Cooperative Development Service, RBCDS Research Report 137, December, 1994.
- Kim, M. S., A. M. Lefcourt, K. Chao, Y. R. Chen, I. Kim, and D. E. Chan. 2002. Multispectral detection of fecal contamination on apples based on hyperspectral imagery: Part I. Application of visible and near-infrared reflectance imaging. *Trans. ASAE* 45(6): 2027–2037.
- Kim, M. S., Y. R. Chen, P. M. Mehl 2001. Hyperspectral reflectance and fluorescence imaging system for food quality and safety *ASAE* ISSN 0001–2351.
- Kim, M. S., A. M. Lefcourt, Y. R. Chen, I. Kim, D. E. Chan, and K. Chao. 2002. Multispectral detection of fecal contamination on apples based on hyperspectral imagery: Part II. Application of hyperspectral fluorescence imaging. *Information and Electrical Technologies Division of ASAE*. ISSN 0001–2351. Vol. 45(6): 2039–2047.
- Kim, D. G., Burks, T. F., Qin, J., Bulanon, D. M., 2009. Classification of grapefruit peel diseases using color texture feature analysis. *Int. J. Agric. & Biol. Eng.*, 2009; 2(3): 41–50.
- Koschan, A., Abidi, M., 2008. “Digital Color Image Processing”, First Edition.
- Lee, K., S. Kang, S. R. Delwiche, M. S. Kim, and S. Noh. 2008. Correlation analysis of hyperspectral imagery for multispectral wavelength selection for detection of defects on apples. *Sens. Instrum. Food Qual. Saf.* 2(2): 90–96.
- Lu, R., 2008. Quality evaluation of fruit by hyperspectral imaging. Chapter in “Computer vision technology in food quality evaluation” edited by Da-Wen Sun.
- Lu, R. 2002. Detection of bruises on apples using Near-Infrared hyperspectral imaging. *Information and Electrical technologies Division of ASAE* ISSN 0001–2351. Vol. 46(2): 523–530.

- Noordam, Jacco C., Willie HAM van den Broek, Lutgarde MC Buydens, 2005. Detection and classification of latent defects and diseases on raw French fries with multispectral imaging. *Journal of the Science of Food and Agriculture* 85:2249–2259 (2005) DOI: 10.1002/jsfa. 2226.
- Park, B., Lawrence, K. C., W. R. Windham, R. J. Buhr 2002. Hyperspectral imaging for detecting fecal and ingesta contaminants on poultry carcasses *ASAE* ISSN 0001–2351.
- Park, B., Chen, Y. R., Nguyen, M., 1997. Multispectral image analysis using neural network algorithm for inspection of poultry carcasses. *J. Agric. Engng. Res.* (1998) 69, 351–363.
- Park, B., Chen, Y. R., 2000. Co-occurrence matrix texture features of multispectral images on poultry carcasses. *J. Agric. Engng. Res.* (2001). 78(2), 127–139.
- Pydipati, R., Burks, T. F., Lee, W. S., 2005. Statistical and neural network classifiers for citrus disease detection using machine vision. *Information and Electronics Technologies Division of ASAE.* ISSN 0001–2351. Vol. 48(5): 2007–2014.
- Pydipati, R., T. F. Burks, and W. S. Lee. 2006. Identification of citrus disease using color texture features and discriminant analysis. *Comput. Electron. Agri.* 52(1–2): 49–59.
- Piron, A., Leemans, V., kleynen, O., Lebeau, F. Destain, M. –F., 2007. Selection of the most efficient wavelength bands for discriminating weeds from crop. *Computer and Electronics in Agriculture* 62 (2008) 141–148.
- Palmer, M. Regents Professor at Dept of Botany of Oklahoma State University. Web document. Accessed on December 2009. Available at: <http://ordination.okstate.edu/PCA.htm>
- Qin, J., T. F. Burks, M. S. Kim, K. Chao, and M. A. Ritenour. 2008. Citrus canker detection using hyperspectral reflectance imaging and PCA-based image classification method. *Sens. Instrum. Food Qual. Saf.* 2(3): 168–177.
- Qin, J., T. F. Burks, M. A. Ritenour., and W. G. Bonn. 2009a. Detection of citrus canker using hyperspectral reflectance imaging with spectral information divergence. *J. Food Eng.* 93(2): 183–191.

Qin, J., T. F. Burks, Xuhui Zhao, N. P. Niphadkar and M. A. Ritenour. 2009b. Hyperspectral band selection for citrus canker detection using multispectral algorithms ASABE Paper No. 096144. Reno, Nevada: ASABE.

SAS customer support website. Copyright 2010 SAS Institute Inc. Accessed on January 2010. Available at: <http://support.sas.com/publishing/pubcat/chaps/55129.pdf>.

Schubert, T. S., Miller, J. W., 2000. Bacterial citrus canker. FDACS, Division of plant industry, Gainesville, Florida. 6 fold.

Shirai, Y., Kondo, N., Fujiura, T., 1998. Machine vision. Chapter in “Robotics for bioproduction systems” edited by Kondo, N., Ting, K. C.

The Imaging Source: Manufacturer of industrial machine vision cameras. How color cameras work? Web document. Accessed on January 2010. Available at: http://www.theimagingsource.com/downloads/howcolcamswp.en_US.pdf

Unay, D., Gosselin, B. 2006. Stem and calyx recognition on ‘Jonagold’ apples by pattern recognition. Journal of Food Engineering 78 (2007) 597–605.

Wikipedia – The free encyclopedia. Updated in December 2009. Accessed on January 2010. Available at: http://en.wikipedia.org/wiki/Principal_component_analysis

BIOGRAPHICAL SKETCH

Nikhil Pramod Niphadkar was born in 1983 in Dhule of State of Maharashtra in India. He graduated with a Diploma in Mechanical Engineering (DME) in May 2002 from Cusrow Wadia Institute of Technology. He earned his Bachelor of Engineering (BE) degree in mechanical engineering in May 2005 from University of Pune, India. He worked with John Deere Equipments Pvt. Ltd., Pune, India from Aug 2005 to August 2006 as a Graduate Trainee where he was a part of transmission manufacturing cycle time reduction team. From November 2006 to June 2007, he worked as an Automation Engineer at Siddheshwar Industries Pvt. Ltd., Pune, India, where he was responsible for designing fixtures for cost efficiency and operator safety. He started his graduate studies at University of Florida as a concurrent masters' student in the Mechanical and Aerospace Engineering and Agricultural and Biological Engineering Departments in August 2007. He joined the Agricultural Robotics and Mechatronics group (ARMg) in the Department of Agricultural and Biological Engineering where he worked as a Research Assistant of Dr. Thomas F. Burks.